2009

EFFECTS OF GEOMETRY ON VORTEX SHEDDING FROM ELONGATED BLUFF BODIES

Zhigang Liu

EFFECTS OF GEOMETRY ON VORTEX SHEDDING FROM ELONGATED BLUFF BODIES

(Spine title: Vortex Shedding from Elongated Bluff Bodies)

(Thesis format: Monograph)

by

Zhigang Liu

Graduate Program of Engineering Science
Department of Civil and Environmental Engineering

A thesis submitted in partial fulfillment
of the requirements for the degree of
Doctor of Philosophy

The School of Graduate and Postdoctoral Studies
The University of Western Ontario
London, Ontario, Canada
August 2009

THE UNIVERSITY OF WESTERN ONTARIO
SCHOOL OF GRADUATE AND POSTDOCTORAL STUDIES

CERTIFICATE OF EXAMINATION

Supervisor	Examiners
Dr. Gregory A. Kopp	Dr. J. Peter C. King
Supervisory Committee	Dr. Horia M. Hangan
	Dr. J. Maciej Floryan
	Dr. Serhiy Yarusevych

The thesis by

Zhigang Liu

entitled:

Effects of Geometry on Vortex Shedding from Elongated Bluff Bodies

is accepted in partial fulfillment of the
requirements for the degree of
Doctor of Philosophy

Date_____

_____
Chair of the Thesis Examination Board

ABSTRACT

A 2-D, high-resolution, vortex particle method was implemented, and its validity and capabilities were demonstrated through comparisons with experimental and numerical data available in the literature for flows around bluff bodies. A series of simulations of the flow around flat plates with various nosings and elongation ratios were performed. The resultant St_c map (variation of chord-based Strouhal number, St_c, with elongation ratio, c/t, and nosing angle, θ) reveals that there are an upper and a lower limit for St_c variations, and, by changing the separation angle at the leading edge, the transition between them appears to be continuous. For plates with a smaller separation angle at the leading edge, St_c increases almost linearly with c/t after a jump, and eventually makes transition to a horizontal variation. From the analyses of mean flow characteristics, visualizations of the vorticity field, and quantitative analyses of identified vortices, the effects of geometry on a number of flow properties were identified, based on which a detailed description of the mechanics leading to various behaviors of St_c is given. It is the alternate predominance of the leading- and trailing-edge shedding in the overall shedding process that leads to the linear and horizontal variations, and abrupt jumps of St_c. When the trailing-edge shedding is in control, the shedding frequency jumps to a higher value and St_c tends to follow a linear variation. When the leading-edge shedding predominates, St_c tends to follow a horizontal variation.

Keywords: numerical simulations; vortex particle method; bluff-body aerodynamics; effects of geometry; elongated bluff body; vortex shedding

ACKNOWLEGEMENTS

I would like to express my sincere gratitude to my supervisor, Professor Gregory A. Kopp, for his guidance and continued support, for his patience and enthusiasm, and for always motivating and pushing me to go further.

My grateful thanks also go to my fellow students and all members of the Boundary Layer Wind Tunnel Laboratory for the assistance I received over the years, and for the friendly working environment.

Finally, and most importantly, I would like to thank my parents for always being there for me, and for their unconditional love and support.

TABLE OF CONTENTS

LIST OF TABLES

LIST OF FIGURES

NOMENCLATURE

c	Chord length of a plate
c/t	Elongation ratio (chord-to-thickness ratio)
C_D	Drag coefficient
C_{Lrms}	r.m.s. value of the lift coefficient
C_p	Pressure coefficient
D	Diameter of a circular cylinder
d_{LT}	Distance between a trailing-edge vortex that just starts to form and the closest leading-edge vortex
f	Frequency
f_v	Frequency of vortex shedding
$\mathbf{F}_b$	Net force on the body
$G(\cdot)$	Green's function
h	Particle spacing
$\hat{\mathbf{i}}$, $\hat{\mathbf{j}}$, $\hat{\mathbf{k}}$	Unit vector in x, y, z direction, respectively
$\mathbf{K}$	Biot-Savart kernel
$\mathbf{K}_\sigma$	Mollified Biot-Savart kernel
L_w	Wake formation length
$M_4'(\cdot)$	Symmetric interpolation kernel
$\hat{\mathbf{n}}$	Unit normal vector
$N_{LEV\max}$	Maximum number of leading-edge vortices simultaneously convecting on the upper or lower surface of the body
$\mathbf{r}$	Position vector
$\mathbf{r}_i$	Position vector of the i^{th} particle

$\mathbf{r}_s$	Position vector on the surface of the body
Re	Reynolds number
St	Strouhal number
St_c	Chord-based Strouhal number
t	Time or the thickness of a plate
$\hat{\mathbf{t}}$	Unit tangential vector
Δt	Time step
T	Non-dimensional time
ΔT	Non-dimensional time step or non-dimensional time interval
$\mathbf{U}$	Velocity vector
U_∞	Freestream velocity
U_c	Convection speed
u	Streamwise velocity
u_{mean}	Mean value of streamwise velocities
u_{rms}	r.m.s. value of streamwise velocities
v	Cross-stream velocity
v_{mean}	Mean value of cross-stream velocities
v_{rms}	r.m.s. value of cross-stream velocities
x_r	Reattachment length

SYMBOLS AND ABBREVIATIONS

β	Overlap ratio
ϵ_Γ	Cutoff ratio
Γ_i	Circulation of the i^{th} particle
Γ_{LEV}	Strength of an identified leading-edge vortex
Γ_{TEV}	Strength of an identified trailing-edge vortex
$\Delta\gamma$	Strength of surface vortex sheet
$\eta_\sigma(\cdot)$	Cutoff function
λ	Panel length
$\Lambda_3(\cdot)$	Symmetric interpolation kernel
$\Lambda_3'(\cdot)$, $\Lambda_2'(\cdot)$	Asymmetric interpolation kernels
ν	Kinematic viscosity
θ	Included angle of a triangular nosing
ρ	Fluid density
σ_i, σ	Core size of the i^{th} particle
$\boldsymbol{\omega}$	Vorticity vector
ω, ω_z	Spanwise vorticity
∇	Del operator
∇^2	Laplace operator
$\mathcal{D}$	Computational domain
$\partial\mathcal{D}$	Solid boundary
2-D	Two dimensional
3-D	Three dimensional

CFD	Computational fluid dynamics
DNS	Direct numerical simulation
FMM	Fast Mutipole Method
ILEV	Impinging leading-edge vortices
ISLI	Impinging-shear-layer instability
LES	Large-eddy simulation
LEVS	Leading-edge vortex shedding
O-R	A streamlined leading edge and a rectangular trailing edge
PSE	Particle strength exchange
PSD	Power spectral density
r.m.s.	Root-mean-square
R-R	Rectangular leading and trailing edges
TEVS	Trailing-edge vortex shedding
Tθ-R	A triangular leading edge with included angle θ and a rectangular trailing edge
Tθ-Tθ	Triangular leading and trailing edges with included angle θ
VIV	Vortex induced vibration

CHAPTER 1

INTRODUCTION

Modern long-span bridges are particularly susceptible to the action of wind due to their flexibility, light weight and low damping. Wind-induced motion, or deflection of the flexible structure, may result in remarkable modifications of the flow pattern. This consequently leads to some changes in the aerodynamic forces acting on the structure, which may be significant enough to alter the structural responses. In wind engineering, the foregoing process, in which the structure motion interacts with aerodynamic forces, is usually referred to as "aeroelastic phenomenon" (Simiu & Scanlan 1996). Different aeroelastic behaviors of bridges are usually classified into vortex-induced vibration, galloping, flutter, buffeting, and torsional divergence (e.g., Parkinson 1971, Simiu & Scanlan 1996).

Torsional divergence is essentially a static instability phenomenon, which depends upon the stiffness of the structure, the manner in which the pitching moment varies with the angle of attack, and the mean wind speed. The structure fails at a critical wind speed due to negative torsional stiffness of the system, in a process that is analogous to column buckling (Simiu & Scanlan 1996). Buffeting is the unsteady loading of a structure due to turbulent wind flow (including self-excited forces due to the interaction of structural motion and aerodynamic forces, or aerodynamic damping). The random response of the structure in natural wind can be obtained using the analytical methods developed by Davenport (1961, 1962), although there are still some aspects, such as the aerodynamic admittance and the spatial correlation of the aerodynamic forces, that need

further investigation. Vortex-induced vibration (VIV), galloping and flutter are all oscillatory instability phenomena. Galloping is driven by self-excited aerodynamic forces, and is characterized by low frequencies (compared to the vortex-shedding frequency) and very large amplitudes. It is satisfactorily described by the quasi-static theory in both smooth and turbulent flow (Laneville *et al.* 1977, Blevins 1986, Simiu & Scanlan 1996). Flutter is also driven by self-excited forces, and usually involves the coupling of bending and torsional motion (classic flutter) or only torsional motion (single-degree flutter), in which the aerodynamic forces are large enough to modify the oscillating frequencies of the structure and cancel the mechanical damping effects. This leads to high levels of deflection, which may result in catastrophic failure of the structure. Based on linear assumptions, the flutter theory developed by Scanlan (1978), which involves the use of "aerodynamic derivatives" determined from wind tunnel tests, has been quite successfully applied to long-span bridges.

What distinguishes VIV from other aeroelastic instabilities is the fact that it always occurs over a narrow band of wind speeds (usually less than the design wind speed) where the natural vortex-shedding frequency is close to that of structural oscillation ("lock-in" or "synchronization") and the amplitude of the motion is large but self-limited. Since lock-in is observed to persist over a range of wind speeds where the vortex shedding frequency is almost constant, it can be inferred that vortex-induced oscillation is not simply a forced vibration driven by the periodic excitation due to vortex shedding, and it is not appropriate to be termed "self-excited" since, although the alternating lift force is modified by body motion, it is not initiated and sustained by the motion like in the case of galloping (see Sarpkaya 1979, 2004). Because of the highly

nonlinear interactions between the structural motion and the flow patterns during lock-in, and the inadequate knowledge of the mechanism of VIVs even in the case of bluff bodies with simple shapes, the mathematical modeling of VIVs of bridges has been less successful (although quite a few sophisticated models for circular cylinders have been developed, see Billah 1989, and Gabbai & Benaroya 2005 for reviews). Since there is no reliable analytical prediction model, the assessment of VIVs for long-span bridges has relied heavily on wind tunnel tests (Macdonald *et al.* 2002). However, due to the lack of understanding of the flow around a bridge deck and the effects of geometry and turbulence, together with the limitations on Reynolds number in wind tunnel tests and the uncertainty in structural damping, it is often a difficult task to interpret the test results. Hence, to some extent, VIVs of a bridge remain a problematic aspect, even after a detailed wind tunnel test, and VIVs observed in wind tunnel smooth flows are often considered questionable and not convincing enough by the designers to modify the design. This has led to retrofits of some bridges (see Owen *et al.* 1996, Larsen *et al.* 2000, and Macdonald *et al.* 2002, for recent examples). In the words of King (2003), "The response to vortex shedding remains an area that needs attention. ... The effect of turbulence on vortex shedding and the ensuing oscillations should be addressed in a systematic fashion."

1.1. EFFECTS OF GEOMETRY ON BLUFF-BODY FLOWS

From the perspective of bluff-body aerodynamics, a bridge deck generally takes the form of an elongated bluff body, which is usually defined as a uniform bluff body with an afterbody that is sufficiently long so that the separated shear layer from the leading edge

can reattach on the surface. However, the vast body of knowledge about bluff body flows accumulated so far has mostly been contributed by studies related to circular cylinders (see Appendix A for a brief review), and which has long been employed by wind engineers to explain various aerodynamic behaviors of bridge decks, even though it has been demonstrated that the flow patterns around non-circular bluff bodies may be substantially different. One of the well known distinctions is that the separation points on a circular cylinder move with varying Reynolds numbers, whereas they are fixed on a sharp edged bluff body. However, as we can see later, this fact does not necessarily make the problem simpler.

A striking example showing the significance of an afterbody is the so called "critical geometry" of a rectangular cylinder (Nakaguchi *et al.* 1968, Bearman & Trueman 1972, Roshko 1993). It is observed that as the chord (c) to thickness (t) ratio (c/t, referred to as elongation ratio hereafter) increases from zero, the drag on a rectangular cylinder rises to a maximum value when $c/t \approx 0.6$ and then levels off with increasing c/t. Bearman & Trueman (1972) argue that, when $c/t < 0.6$, the afterbody, while extending into the vortex formation region downstream, barely has any effect on the separated shear layers. It is observed in Bearman (1965) and Griffin & Ramberg (1974) that the base suction is lower when vortices form further away from the body, which is also shown in the numerical simulations by Tan *et al.* (2004). For cylinders with $c/t > 0.6$, vortex formation in the wake is delayed further downstream due to the interference of the trailing edge of the cylinder with the separated shear layers, and thus a recovery in base pressure is observed. Roshko (1993) points out that the base suction is highly dependent on the vortex formation region in the wake: the contribution from the low-pressure

formation region decreases with longer formation length, and the influences from the separated shear layers are enhanced as a result.

Another interesting example of afterbody effects is the Strouhal-Reynolds number relationship for rectangular plates with elongation ratios of c/t = 1, 2, 3 and 4 in the range $70 < Re < 2\times10^4$ discussed in Okajima (1982). For c/t = 1, the Strouhal number varies continuously with increasing Reynolds number, and remains nearly constant at about 0.13 at high enough Reynolds numbers (say, $Re > 900$). However, the situation is rather different for c/t = 2. An abrupt downward jump in Strouhal number at $Re \approx 500$ is observed, after which the Strouhal number varies slowly with Reynolds number and asymptotes to a roughly constant but lower value of 0.08 to 0.09 at $Re > 5{,}000$. Based on flow visualizations and numerical simulations, Okajima argues that these behaviors may be attributed to the interference of the afterbody with the separated shear layers. For c/t = 1, the separated shear layers do not reattach on the body surfaces, and earlier transition in the shear layers at higher Reynolds numbers does not seem to affect the Strouhal number significantly. For c/t = 2, the shear layers reattach alternately on the upper and lower surfaces of the body in a shedding cycle for $Re < 500$. When Reynolds number is increased past the critical value, the shear layers become fully detached, and, hence, a sudden widening of the wake and a downward jump of Strouhal number are observed. The situation is further complicated for c/t = 3. For $Re < 500$, the variation of Strouhal number is similar to that for c/t = 2. When $Re > 500$, the shear layers do not fully detach from the body due to a longer afterbody. Strongly intermittent fluctuating velocity signals were observed in the wake, and multiple Strouhal numbers were obtained from spectral analyses in the range of Re = 1,000-3,000. Unsteady reattachment of separated shear

layers for $c/t \geq 2.8$ is also reported by Nakaguchi *et al.* (1968). At even higher Reynolds numbers, the higher frequency mode survives, leading to a nearly constant Strouhal number of 0.16-0.17. The Strouhal numbers for $c/t = 4$ are found to be essentially independent of Reynolds number.

Although substantial distinctions exist, the flow fields around short bluff bodies of various shapes also show similarity, to some extent, which may be supported by the concept of a "universal Strouhal number" (Fage & Johansen 1928, Roshko 1954b, Goldburg & Florsheim 1966, Bearman 1967, Simmons 1977, Griffin 1978, 1981, Sarpkaya 1979, Nakamura 1996, Yarusevych 2009). Based on experiments on various short bluff bodies, Nakamura (1996) concludes that, even though the base suction of a bluff body is highly dependent on both cross-sectional shape and elongation ratio, the Strouhal number only decreases with increasing c/t, and is essentially independent of the details of section geometries for elongation ratios up to 1.0. It should be noted, however, that these "universal" Strouhal numbers are not really universal, but subject to limitations. As pointed out by Nakamura (1996), Roshko's universal Strouhal number is based on the assumption that "the wakes of different bluff bodies are similar in structure", which, from the foregoing discussions, is obviously not always true for bluff bodies with an afterbody. Nakamura suggests that Roshko's universal Strouhal number may only be applied to bluff bodies without an afterbody that may interfere with the separated shear layers.

1.2. SEPARATED AND REATTACHING FLOWS

Figure 1.1 shows a schematic sketch of the flow around a rectangular plate. The flow tends to separate at the sharp leading edge, and reattach to the plate surface after some

distance, x_r, to form a separation bubble (the region with substantial backflow between the separation point and reattachment point, which is in turn usually defined as the point where the mean wall shear stress vanishes, see e.g., Castro & Haque 1987, and Djilali & Gartshore 1992) if the plate is long enough. The reattached flow redevelops along the body surface until the trailing edge is encountered, where it separates again and tends to interact with the separated shear layer from the other side of the plate.

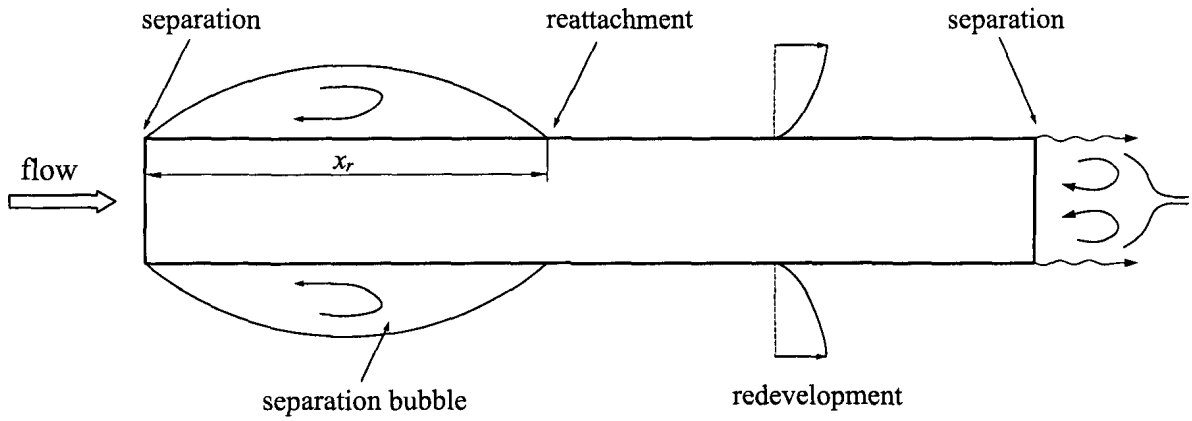

Figure 1.1. Schematic sketch of the flow around a rectangular plate

Two types of separated flows are commonly encountered in bluff body flows (Kiya *et al.* 1997): separated shear layers and separated and reattaching flows. Examples of the former are the two separated shear layers from a circular cylinder, and those from the trailing edge of an elongated bluff body as shown in Figure 1.1. The separation bubble on a long blunt plate in Figure 1.1 is a good example for the latter.

As mentioned earlier, we define an elongated cylinder as a uniform bluff body with an afterbody that is sufficiently long so that the separated shear layer from the leading edge may reattach on its surface. However, it is difficult to precisely define how long is "sufficiently long", because the reattachment length of a separated shear layer can be affected by many factors (Eaton & Johnston 1981, Westphal & Johnston 1984, Cherry

et al. 1984, Castro & Haque 1987, Hancock 2000), such as free-stream turbulence, boundary layer properties at separation, end effects, blockage ratio, geometry of the bluff body, three-dimensional effects, Reynolds number effects, body motion, external forcing, and so on. This concept is introduced for convenience, so that when we speak of an elongated bluff body, we assume that reattachment occurs, at least intermittently.

1.2.1. Reattachment Lengths

As noted above, one of the important factors that have pronounced effects on the reattachment length of a separated shear layer is the body geometry. For flows past a wide range of forebody and splitter-plate combination, the empirical relationship between the mean reattachment length and the separation angle proposed by Simpson (1985, 1989) has been shown to fit the experimental data remarkably well (see also Yeung & Parkinson 2004). However, the reattachment lengths measured by Djilali & Gartshore (1992) on flat plates with symmetric triangular nosings of different angles significantly deviate from Simpson's relationship. A modified form of Simpson's formula is proposed by Djilali & Gartshore, which approximates their data within 5%:

$$x_r(\alpha) = x_r(90^\circ)\sin^2\alpha \tag{1-1}$$

where x_r is the reattachment length, a function of the separation angle α, and $\alpha = 90^\circ$ corresponds to the case of a rectangular (blunt) leading edge. A similar value of $x_r = 4.7$-$5.2t$ has been observed in many experiments on blunt plates (e.g., Lane & Loehrke 1980, Cherry *et al.* 1983, 1984, Kiya & Sasaki 1983, Cao & Hancock 2004). Nevertheless, a much longer reattachment length, $x_r = 7.7t$, is reported by Castro & Epik (1998), who argue that this may be justified by the much lower blockage ratio (1.2%, compared to 4-5%

in other work) and substantially larger (spanwise) aspect ratio (64 versus around 10 in other work) of the plate in their experiments. This is consistent with the trend in the data compiled in Cherry *et al.* (1984) that the separation bubble on a blunt plate is longer when the blockage ratio is smaller and/or the aspect ratio is larger. Blazewicz *et al.* (2007) also report a larger value of x_r = 6.0-6.2t for rectangular plates with $c/t > 17$ from their open-jet wind tunnel experiments. More importantly, their data for c/t = 6.5-23 show that x_r increases with c/t until it saturates at c/t = 17. Similar dependence of x_r on c/t for rectangular plates with $c/t \leq 9$ is also observed by Yaghoubi & Mahmoodi (2004).

The reattachment length has been shown to be an appropriate length scale to normalize bubble geometries (Roshko & Lau 1965, Eaton & Johnston 1981, Westphal & Johnston 1984, Driver *et al.* 1987, Hudy *et al.* 2003), and it is possible to study a separation bubble without worrying about the details of its formation, to some extent. For example, if the pressure distribution under a separation bubble is normalized as suggested by Roshko & Lau (1965), $C_p^* = \left(C_p - C_{p\min}\right)/\left(1 - C_{p\min}\right)$ (where C_p is the measured pressure coefficient, and $C_{p\min}$ is its minimum value), the pressure data can be reasonably collapsed onto a single curve against x/x_r (Roshko & Lau 1965, Cherry *et al.* 1983, Castro & Haque 1987, Djilali & Gartshore 1992, Hudy *et al.* 2003, and Yeung & Parkinson 2004) for elongated bluff bodies with a wide range of geometries (with the exception for a backward facing step with a long streamlined nose, possibly due to the much thicker boundary layer at separation, see Roshko & Lau 1965 and Cherry *et al.* 1983). In addition, Westphal & Johnston (1984) report that the velocity profiles and skin friction in the recirculation region also scale strikingly well with reattachment lengths. They further

argue that some observed deviations in the scaling may be due to large uncertainties in reattachment length measurements.

1.2.2. Vortex Shedding From a Separation Bubble

The reattachment of a shear layer is a highly unsteady process (Cherry *et al.* 1984, Driver *et al.* 1987, Castro & Haque 1987, Simpson 1989, Bandyopadhyay 1991, and Sigurdson 1995). In the reattaching zone, the separated shear layer curves sharply and impinges on the body surface, where a strong adverse pressure gradient drives part of the shear-layer fluid into the reverse flow region, and the instantaneous reattachment point oscillates randomly up and downstream. Mabey (1972) finds a broadband peak at approximately $f_s x_r/U_\infty \approx 0.5 - 0.8$ (with f_s being the peak frequency, x_r the reattachment length, and U_∞ the free-stream velocity) in the turbulent energy spectrum of separated and reattaching flows, which is indicative of vortical structures. Indeed, unsteady shedding of large scale vortices from the bubble is commonly observed, which probably comes from the initial roll-up of the vortex sheet due to Kelvin-Helmholtz instability and multiple parings in the separated shear layer (Castro & Haque 1987, Simpson 1989, Bandyopadhyay 1991, Soria *et al.* 1993, Song & Eaton 2004, Yarusevych *et al.* 2009). The formation and shedding of large structures from reattaching flows is termed the "shedding-type instability" of the bubble by Sigurdson & Roshko (1988), in addition to the Kelvin-Helmholtz instability of a free shear layer, whereas Nakamura *et al.* (1991) suggest that an "impinging shear layer instability" is responsible for the shedding. Sigurdson (1995) further suggests that this shedding-type instability is analogous to that

which leads to the periodic vortex shedding in the wake of a bluff body, and a scaling of the frequency f_s of this instability is found to be universal,

$$f_s d/U_s \approx 0.08 \tag{1-2}$$

which is almost the same value of 0.08 as given by Roshko (1955) for Kármán vortex shedding from a bluff body. In Equation (1-2) U_s is the flow velocity at separation, and d represents the half distance between the vorticity and its corresponding image of opposite sign. Driver *et al.* (1987) find in their backward-facing step flow investigations that the maximum contribution to the turbulence energy, both up and downstream of reattachment, always comes from the components at $f_s x_r/U_\infty \approx 0.6$. Kiya *et al.* (1997) hypothesize that the separation bubble is a self-excited flow sustained by a feedback loop. When a large scale vortex impinges on the surface in the reattachment zone, a pressure pulse is generated, which propagates upstream at the speed of sound to the separation edge, and, hence, modifies the separation and rolling-up behaviors of the shear layer. The frequency of the shedding may be expressed as $f_s x_r/U_\infty = U_c/U_\infty$, where U_c is the average convection speed of the vortex in the separation bubble. Kiya *et al.* suggest that U_c near reattachment may be approximately taken as $U_c/U_\infty \approx 0.5$ since this is observed in a number of experiments (Kiya & Sasaki 1983, Cherry *et al.* 1984). Higher values of $U_c/U_\infty \approx 0.57$-$0.7$ have also been reported by other researchers (Cherry *et al.* 1984, Nakamura *et al.* 1991, Hudy *et al.* 2003). It is shown by Tan *et al.* (2004), through numerical simulations of flow around rectangular plates at $Re = 400$, that U_c/U_∞ actually rises rapidly from a minimum value of around 0.2 when it is being formed, and approaches a saturated value of about 0.7 far downstream.

The influence of separation and reattachment on downstream boundary layer development has been observed to be "extremely long-lived" (Castro & Epik 1998). Far downstream of reattachment, the mean velocity profiles of the developing boundary layer resemble that of a canonical one, but very energetic eddies persist and dominate the turbulence in the outer shear layer (Bradshaw & Wong 1972, Eaton & Johnston 1981, Song *et al.* 2000, Song & Eaton 2004). Bradshaw & Wong (1972) suggest that the classical relationship for a boundary layer velocity profile cannot be applied at least within $30t_b$ (with t_b being the boundary layer thickness at the time mean reattachment point) after reattachment in a step flow, while an even higher value of $70t_b$ is reported by Castro & Epik (1998) for a flat plate (where $t_b \approx 2.06t$). They attribute this persisting effect to the large-scale vortex shedding in the reattachment region. Parker & Welsh (1983) suggest that on a flat plate the elongation ratio must be larger than 25 for the flow at the trailing edge to be independent of the leading edge separation and subsequent reattachment.

1.2.3. The Low-Frequency Motion of a Separation Bubble

A weak "flapping" motion (quasi-periodic extension and collapse of the bubble) at very low frequencies also exists throughout the separation bubble, although most noticeable in the range $x < 0.25x_r$ (Kiya & Sasaki 1983, Cherry *et al.* 1984, Castro & Haque 1987, 1988, Driver *et al.* 1987, Simpson 1989, Hudy *et al.* 2003, Castro 2005). The flapping frequency is usually expressed as $f_p x_r/U_\infty < 0.1$ (Simpson 1989), or 5-10 times lower than that of the passage of large scale vortex structures (Castro 2005). Cherry *et al.* (1984) speculate that this low-frequency motion may be "an integral feature of a

fully turbulent separation", and it may be associated with some overall bubble growth-decay mechanism since it scales well with the reattachment length. However, it is shown in Castro & Haque (1988) that the low-frequency motion in fact does not scale exactly with the bubble size, and the timescale of which can be noticeably reduced with the introduction of free-stream turbulence. Kiya & Sasaki (1983) speculate that the flapping motion is the result of intermittent shedding of large vortical structures from the bubble, while Castro & Haque (1987), and Simpson (1989) suggest that it may be related to the phase variations of the large-scale vortex shedding. From experiments on the separation bubble produced by a fence-splitter plate combination, Hudy *et al.* (2003) demonstrate that there are two distinctive regions in the bubble: for $x < 0.25x_r$, the surface pressure is dominated by low-frequency fluctuations which convect upstream at a velocity of $0.21U_\infty$, and for $x > 0.25x_r$, the flow is characterized by smaller time scales and the dominant pressure fluctuations convect downstream at a velocity of $0.57U_\infty$. Transition between these two regions was found to occur between $0.25x_r$ to $0.5x_r$. Hudy *et al.* further suggest that an absolute instability zone exists near the center of the bubble, where upstream and downstream disturbances emanate. It is presumed that this absolute instability results from the instability of the recirculation flow in bubble, and is responsible for continuous expansion and contraction of the bubble and consequently the shear layer flapping. It is further speculated that the flapping motion may in turn "modulate the shear layer instability process," and, hence, affects "to some degree" the development of shear-layer vortices "on instantaneous bases." They emphasize that the idea of absolute instability in the bubble does not contradict the shedding-type instability, as the latter is related to the instability of the shear layer near the reattachment in the presence of a wall.

1.3. VORTEX SHEDDING FROM A BLUNT TRAILING EDGE

If the elongated cylinder has a streamlined leading edge, the flow may remain attached to the cylinder until the trailing edge is encountered. This idea makes it possible to focus on vortex shedding at the trailing edge alone (see Wood 1971, Staubli & Rockwell 1989, Lotfy & Rockwell 1993, Hourigan *et al.* 2001, and Mills *et al.* 2005 for examples). Usually a "streamlined" leading edge may take the shape of an airfoil tip, a semi-ellipse or a half Rankine oval in order to eliminate flow separation, while a semi-circular shape is also used for its simplicity.

Generally, vortex shedding at the trailing edge of an elongated cylinder with streamlined leading edge mimics that from a circular cylinder (Staubli & Rockwell 1989). However, an obvious difference is that the attached boundary layers may now be able to develop over much longer distances before separating at the trailing edge. In addition, in contrast to a circular cylinder, where the boundary layer is subjected to strong adverse pressure gradient, the flow on a flat plate with a streamlined leading edge usually has a zero pressure gradient at separation (Staubli & Rockwell 1989, Lotfy & Rockwell 1993). Increasing the streamwise length of the body changes the state of boundary layers at the trailing edge, which may in turn affect vortex shedding and the wake. For example, a longer development distance may lead to a thicker boundary layer at separation, which in turn results in a wider wake and a lower Strouhal number, accompanied by a slightly lower base suction (Bull *et al.* 1995, Mills *et al.* 2005). A sudden drop in Strouhal number is observed by Parker & Welsh (1983), and Welsh *et al.* (1984), when the elongation ratio of the plate with a semi-circular leading edge reduces from about 1.2 to 1, which they attribute to the effects of separated shear layers at the leading edge, since with

a semi-circular leading edge, the flow still separates at a small angle (and which is subject to Reynolds number effects) and reattaches rapidly. They argue that when $c/t \leq 1$ the separated shear layers do not reattach to the cylinder permanently and interact downstream the trailing edge, which leads to a longer vortex formation region in the wake and hence a lower Strouhal number.

1.4. VORTEX SHEDDING FROM ELONGATED BLUFF BODIES

Based on a series of experiments on rectangular flat plates at Re = 14,800 – 31,100 (based on plate thickness), Parker & Welsh (1983) suggest that there exist four possible vortex shedding regimes depending on c/t, which are summarized by Stokes & Welsh (1986) as follows:

a) Short plates ($c/t < 3.2$): leading-edge shear layers do not reattach to the surface of the plate, instead they interact directly in the wake to form a regular vortex street.

b) Longer plate ($3.2 < c/t < 7.6$): the leading-edge shear layers reattach to the plate "periodically", after which the separation bubbles tend to grow beyond the trailing edge, when the fluid in the recirculation region enters the wake to form vortices, and a regular vortex street is usually observed.

c) Still longer plates ($7.6 < c/t < 16$): the leading-edge shear layers permanently reattach upstream of the trailing edge to form separation bubbles on the plate. It is presumed that the separation bubble tends to "grow and divide in a random manner", and the discrete vortices shed from the bubble arrive at the trailing edge randomly and interfere with the separating shear layers there. Hence, the

subsequent shedding at the trailing edge is disorganized and no regular vortex street can be observed.

d) Very long plates (c/t > 16): the leading edge shear layers behave in nearly the same manner as in regime (c), but the vortices shed from the reattaching flow are supposed to "diffuse" upstream of the trailing edge. The flow separates again at the trailing edge without much interference from the leading edge vortices, and hence a regular vortex street is re-established.

Through wind tunnel experiments on H-section cylinders, Nakamura & Nakashima (1986) have shown that, when Kármán vortex shedding is suppressed by installing a long splitter plate in the near wake, vortex-included vibrations (VIVs) of the bodies persist, and even the on-set wind speeds remain unchanged. This observation is in direct contradiction to the conventional understanding that Kármán vortex shedding in the wake is responsible for VIVs. It is postulated that the shear layers in regime (b) can be characterized by the "impinging-shear-layer instability" (ISLI hereafter), a concept originally developed for cavity flows (Rockwell & Naudascher 1978, 1979), whereby a leading-edge shear layer becomes unstable in the presence of a sharp trailing-edge corner. They argue that this is a single-layer instability and it exists even when a splitter plate is installed in the wake, while the instability frequency remains the same as the shedding frequency in the case without a splitter plate. The frequency of this single layer instability is almost constant at $St_c = f_v c/U_\infty = 0.6$, which is consistent with their observations for elongated cylinders with c/t = 2-5.

Further experiments on rectangular plates covering an elongation-ratio range of c/t = 3-16 (where c/t = 3 is believed to be the minimum value necessary for ISLI to exist)

were performed by Nakamura *et al.* (1991), in which regular vortex shedding was observed for c/t = 3-15 at Re = 1,000, while for c/t = 16 no dominant peak was detected in the spectrum of fluctuating velocity in the wake. It is also shown that, when Re > 2,000, regular vortex shedding disappears for rectangular plates with c/t > 12. They argue that this is because the ISLI, although still present in the flow, is "masked" by the increased turbulence fluctuations at higher Reynolds numbers, but can be excited by external forcing. A stepwise variation of St_c with c/t is identified by Nakamura *et al.*, as shown in Figure 1.2, where St_c is nearly constant at $0.6n$ for each step, in which n = 1,2,3... is considered to be the wave number of the instability on the cylinder surface. It is proposed that the instability wavelength is locked to the chord due to "some nonlinear flow processes" until jumps occur at certain c/t values. Open circles near St_c jumps in the figure indicate that intermittent velocity signals were observed. Nakamura *et al.* speculate that the feedback from the "impinging edge" tends to affect the vorticity generation at the separation point and greatly enhance the "shear-layer instability", but how this feedback works is left unexplained.

Naudascher & Wang (1993), and Naudascher & Rockwell (1994) suggest that the flows in regimes (a) and (d) are characterized by "leading-edge vortex shedding" (LEVS) and "trailing-edge vortex shedding" (TEVS), respectively. While for regimes (b) and (c), the flow is governed by "a flow instability equivalent to that of impinging shear layers", whereby vortices are produced in the unstable leading-edge shear layers and are convected downstream, weak pressure pulses are generated when they pass the trailing edge and propagate upstream to the leading edge to regulate the formation of new vortices. This flow instability concept, which leads to "impinging leading-edge vortices"

(ILEV), appears similar to the "shedding-type instability" proposed by Sigurdson & Roshko (1988) for separated and reattaching flows, and the proposed feedback loop mechanism seems to be able to reasonably explain why the frequency of leading-edge vortex shedding is locked to the plate chord.

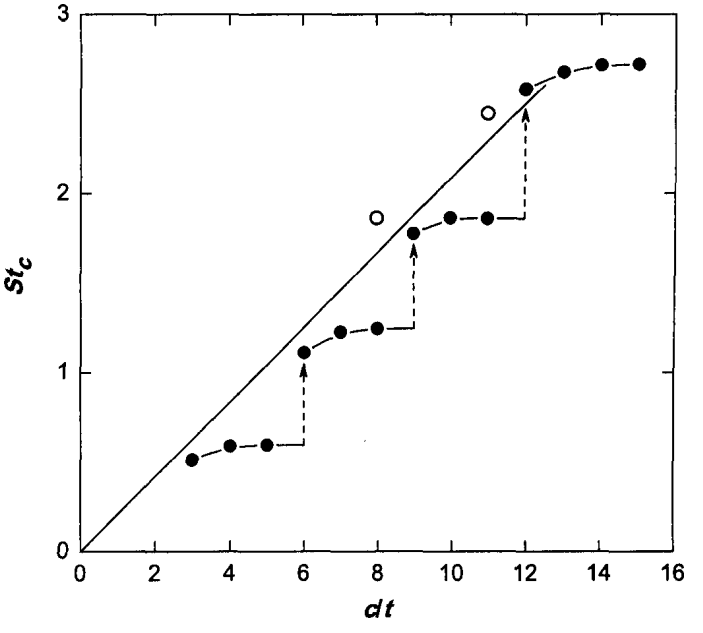

Figure 1.2. Stepwise variation of St_c with c/t (after Nakamura *et al.* 1991); open circles indicate that secondary peaks were observed in spectral analyses

Based on numerical simulations at $Re \leq 700$, Hourigan *et al.* (2001) suggest that the trailing-edge vortex shedding (TEVS) also plays an important role in the self-sustained flow oscillations around long rectangular plates. They speculate that, for elongated cylinders fitted with splitter plates where no TEVS occurs, the flow instability may be characterized by ILEV described above, and the feedback loop is completed by upstream propagating pressure pulses generated when the leading-edge vortices pass the trailing edge. For cylinders with blunt trailing edges, the leading-edge vortices tend to interact with TEVS as they convect past the trailing edge. They argue that trailing-edge

vortices at the trailing edge can only form in-between the arrivals of leading-edge vortices from the developing boundary layer after upstream reattachment. TEVS can generate a stronger pressure pulse than the passage of a leading-edge vortex, which travels upstream to regulate the "preferred" shedding frequency to be that of the TEVS. It is shown by Tan *et al.* (2004), through numerical simulations, that the change of the vorticity flux into the leading-edge shear layer due to the effect of trailing-edge shedding is well correlated with the variation of the total vorticity flux. In contrast, that due to the passage of leading-edge vortices is poorly correlated, which is believed to be an indication that the TEVS contributes much more than ILEV in the feedback loop.

It is speculated in Mills *et al.* (2002, 2003) and Tan *et al.* (2004) that the naturally preferred "global oscillation frequency" of the flow around a long rectangular plate is the one that leads to the peak base suction, or the most intense TEVS, which generates the "dominant" pressure pulse feedback to the leading edge. They postulate that since the vortices that are periodically shed from the leading edge convect downstream at a nearly constant velocity U_c independent of c/t, it takes a longer time for leading edge vortices to arrive at the trailing edge on a longer plate. However, it always takes an integer number of shedding cycles for the leading edge vortices to arrive at the trailing edge regardless of elongation ratios, because their generation is controlled by the feedback pressure pulse generated at the trailing edge, which occurs only in-between the successive arrivals of leading edge vortices. It is also shown that, by changing the frequency of the external forcing, the phase at which the leading-edge vortex arrives at the trailing-edge can be controlled. If it passes the trailing edge at a phase of 180°, it tends to suppress the TEVS. They further suggest that, as the leading-edge vortex convects past the trailing edge, it

interacts with trailing-edge vortex (which is of the same sign) and they merge into one larger vortex before being shed into the wake. This occurs alternately on each side of the plate and a regular vortex street wake is observed. Tan *et al.* argue that, while the leading-edge shear layers are convectively unstable and are very sensitive to external forcing, the trailing-edge shedding, which is globally unstable, can only exist over a narrow frequency band, and, hence, it may be controlling the frequency selection. As c/t increases, the preferred shedding frequency for TEVS is no longer possible for certain elongation ratios because of "interference from leading-edge vortices", and a "nearby" frequency is selected at which TEVS could occur and the shedding jumps to a higher "mode" (Hourigan *et al.* 2001, Mills *et al.* 2002, 2003). As Reynolds number is increased above 2,000 for long rectangular plate, the relatively weak feedback mechanism may be "broken down" by the enhanced inherent turbulence in the flow, but the same locking effect may be excited by external forcing with appropriate frequency and amplitude.

From wind tunnel experiments on elongated cylinders with a variety of leading and trailing edges over a wide range of elongation ratios, Shiraishi & Matsumoto (1983) find that the critical reduced wind speed for vertical VIVs can be well related to the elongation ratio as $V_{cr} = (1/0.6n)(c/t)$ for $c/t = 2 - 7.5$, where n is an integer number. It is hypothesized that the leading-edge vortices convect downstream at an almost constant velocity $U_c = 0.6U_\infty$, and VIVs occur only when the leading-edge vortices coalesce with trailing-edge vortices after an integer number of the natural vibration period. This is consistent with the aforementioned stepwise variation of chord based Strouhal number and the explanation of Mills *et al.* (2002, 2003).

1.5. OBJECTIVES

The vast body of knowledge in the literature has led to a reasonable understanding of the flow around circular cylinders. However, although the wind engineering community has reported a large number of wind tunnel tests on vortex-induced vibrations (VIVs) of bridges, relatively little progress has been made toward understanding the mechanisms behind various aerodynamic behaviors observed in the tests. One of the reasons for the slow progress may be attributed to the complex geometries of bridge decks, which leads to a much larger parameter space than that for circular cylinders and rectangular plates. While previous studies on the flow around rectangular cylinders have provided valuable insights into vortex shedding from elongated bluff bodies, there is a lack of detailed knowledge regarding the effects of geometric details (e.g., nosing shapes, and asymmetry of upper and lower surfaces, etc.). Application of the main findings from these studies, such as the classification of flow regimes based on elongation ratios (c/t), and the stepwise variation of chord-based Strouhal numbers ($St_c = f_v c/U_\infty$), to flows around bridge decks is still limited. Bridge deck nosings are usually designed to form obtuse angles with the upper and lower surfaces, which lead to smaller separation angles and earlier reattachment, significantly modifying the flow pattern and shedding frequency. In practice, a significant matrix of wind tunnel tests is often performed to help determine the "optimal" aerodynamic shape of the bridge deck, and comparisons between testing results of different deck profiles have proven a difficult task due to the lack of understanding of geometric effects. Hence a better understanding of the effects of geometry on vortex shedding from various elongated bluff bodies is considered an essential step toward a better understanding of VIVs of long-span bridges.

Thus, the main objective of the present study is to identify the effects of geometry on vortex shedding from elongated bluff bodies, so that explanations of the effects of nosing shapes and elongation ratios may be offered in a systematic way.

1.6. RESEARCH METHODS

To achieve the objective of the present study, a parametric analysis of flows around elongated bluff bodies is indispensable. Experimentally, this would involve dozens of testing models and an enormous amount of data, which will be expensive and time consuming. Numerical simulations are considered a more suitable method to accomplish the objective of the present study, due to the large parameter space and the need for flow visualizations close to the body surfaces.

Vortex methods, which Ferziger (1993) called the "chief competitors" to conventional grid-based simulation methods, have been shown to produce excellent results for complex bluff-body flows, and are "unsurpassed for explaining the genesis of forces on a body" (Ferziger 1993). In the past two decades, developments of new tools and fast algorithms have brought vortex methods "closer to conventional grid-based methods" (Cottet *et al.* 2002). High-resolution vortex methods, as an alternative approach to direct numerical simulations (DNS), are now capable of producing accurate results for complex bluff-body flows that can only be achieved with high-order spectral methods (Koumoutsakos 2005).

As pointed out by Anderson & Greengard (1985) and Cottet *et al.* (2002), time-step limitations are far less restrictive for vortex methods than for grid-based methods because vortex methods are free of convection-related stability conditions. In other words,

large time steps may be used and substantial savings of computational time over grid-based methods can be achieved (see also Koumoutsakos 2005). This is in addition to considerable time savings due to the fact that the vorticity field that needs to be solved usually exists only in small fractions of the whole flow field. Far-field boundary conditions are automatically satisfied for vortex particles with a compact support, and hence, there is no need for a large computational domain to minimize blockage effects. Another advantage of vortex methods over grid-based methods is that the interactions between computational elements mimic the physics they represent so that no additional criteria for "critical parts" of the flow (which are not always known *a priori*) are necessary (Beale & Majda 1982ab, Koumoutsakos 2005). Moreover, the Lagrangian formulation means that there is no numerical diffusion associated with convection, and the dynamics are not constrained by a prescribed minimum scale and, thus, is a robust way for high Reynolds number flow simulations.

On the other hand, three-dimensional (3-D), high-resolution simulations are still far too time consuming for practical applications. For example, Ploumhans *et al.* (2002) have reported a 3-D vortex method simulation for the flow past a sphere at Re = 1,000, in which the total run time of 4,000 time steps was about 240 hours on a 64-processor HP V-Class system. Two-dimensional (2-D) simulations, of course, will not capture any 3-D effects. In the context of bluff-body flows, an evident example of 3-D effects is the lack of spanwise correlation of vortex shedding and pressure when the body is at rest, while in 2-D simulations a perfect spanwise correlation is always inherently presumed. This may lead to overprediction of total forces on the body, which is usually not too excessive (for example, up to 10% overprediction in drag coefficient for a circular cylinder at $Re \approx 200$,

see Mittal & Balachandar 1995, Tutar & Holdø 2000, and Al-Jamal & Dalton 2004 for comparisons). Through systematic comparisons between results of 2-D and 3-D computations for stationary circular and elliptic cylinder flows, Mittal & Balachandar (1995) have shown many subtle differences between these two approaches. It is argued that in 2-D simulations, all the energy extracted from the mean flow field is used to drive the in-plane velocity fluctuations, while part of the energy is spent on sustaining spanwise velocity fluctuations in 3-D computations, leading to a reduction in in-plane fluctuations of velocities and Reynolds stresses. It is suggested that the effect of higher in-plane Reynolds stresses in the near wake on surface pressures is one of the main reasons for the overprediction of drag in 2-D simulations, and the discrepancies are dependent on the cylinder geometry. They also find that the vortex formation region is usually shorter in 2-D than in 3-D results, which, although is shown to have little direct effect on the mean drag, brings the intense Reynolds stress region closer to the body, and is considered to be partly responsible for larger amplitudes of lift fluctuations predicted in 2-D computations.

An interesting example, showing the capability of 2-D simulations to capture the physics in a turbulent phenomenon, is reported by Orlandi (2007), who, after performing both 3-D and 2-D DNS simulations of co-rotating vortices at Re = 3,000 (based on circulation), concludes that, "The most important output of these expensive simulations is that, at this Re, the results do not differ largely from those of 2-D simulations." In fact, it has been observed in the experiments by Cerretelli & Williamson (2003) that the merging process of two co-rotating vortices is "principally two-dimensional." That is, although turbulence is always 3-D, there are many phenomena dominated by 2-D processes that may be studied with a 2-D approach.

In the present study, a two-dimensional CFD code for incompressible, viscous flows, based on the state-of-the-art high-resolution vortex method is implemented. The code is validated against numerical and experimental results available in the literature, and is then used as the tool to investigate geometric effects on vortex shedding from elongated bluff bodies.

The rest of the thesis is organized as follows. In Chapter 2, the theory and implementation of the high-resolution vortex particle method is presented, and simulations of various bluff-body flows are validated against numerical and experimental data available in the literature. In Chapter 3, a series of numerical simulations of flows around flat plates with various nosings at $Re = 600$ are performed, and the resultant flow fields are examined. And finally, concluding remarks and recommendations for future studies are given in Chapter 4.

CHAPTER 2

THEORY AND IMPLEMENTATION OF THE 2-D VORTEX PARTICLE METHOD

2.1. INTRODUCTION

Computational fluid dynamics (CFD) has achieved rapid progress along with computational technologies during the past three decades, and has become a promising and popular research and engineering tool (see Shang 2004, Ekaterinaris 2005, Fujii 2005, and Fureby 2008 for recent reviews). It is now well known to researchers that CFD is a powerful tool in many situations, but by no means a magic tool that solves all the problems we face (Fujii 2005).

Vortex methods, which Ferziger (1993) called the "chief competitors" to conventional grid-based simulation methods, have been shown to produce excellent results for complex bluff-body flows, and are "unsurpassed for explaining the genesis of forces on a body" (Ferziger 1993). However, classical vortex methods focused on various techniques to achieve stable and fast computations, while accuracy at finer scales was sacrificed. As a result they have suffered from a reputation as "back-of-the-envelope" version of CFD methods, and have not become an accepted member of the mainstream CFD tools (Shiels 1998, Barba 2004).

In the past two decades, developments of new tools and fast algorithms have brought vortex methods "closer to conventional grid-based methods" (Cottet *et al.* 2002). Barba (2004) suggests that there have been three major reasons for vortex methods being

left out of standard CFD family. Firstly, the velocity field calculation using Biot-Savart law involves $\mathcal{O}(N^2)$ operations for N vortex particles and, hence, requires special numerical treatment. This problem has been successfully addressed due to the advent of the Fast Mutipole Method (FMM) which reduces the operation count to $\mathcal{O}(N)$ (Barnes & Hut 1986, Greengard & Rokhlin 1987). Other ways around this problem have been developed through mixed Eulerian-Lagrangian formulations (at the cost of introducing numerical diffusion due to interpolation errors), such as the Vortex-in-Cell (VIC) method (see, e.g., Christiansen 1973, Couet *et al.* 1981, Cottet 1987) which reduces the operations to $\mathcal{O}(M\log M)$ (where M is the number of grid points), and the Particle-Particle Particle-Mesh (P^3M) technique, also with a nominal operation cost of $\mathcal{O}(N\log N)$ (Hockney *et al.* 1973, and Walther 2003). Secondly, including viscous effects in a Lagrangian formulation has proven a difficult task. This problem has received much attention in the past three decades and many vorticity diffusion schemes have been introduced. Typical examples are the Random Walk Method (Chorin 1973), Core Spreading Method (Leonard 1980, Rossi 1996), Particle Strength Exchange (PSE) method (Degond & Mas-Gallic 1989), and Vorticity Redistribution Method (Shankar & Van Dommelen 1996), among others. The no-slip boundary conditions at a solid surface have been successfully addressed by the numerical scheme proposed by Koumoutsakos *et al.* (1994), which is "rigorous and free of ad hoc numerical parameters". The third reason is that the Lagrangian evolution results in a loss of discretization accuracy due to the distortion of the particle distribution in areas of large strain, giving rise to creation and evolution of spurious vortical structures in the flow. A variety of "remeshing" or "redistribution" schemes using high-order interpolation kernels on regular Cartesian grids

have been proposed to tackle this problem (see Beale & Majda 1985, Cottet & Koumoutsakos 2000), and high resolution, totally mesh-less vortex methods (Shankar 1996, Barba 2004) have been proposed to avoid this problem. Vortex particle methods are still under intensive development. New techniques, implementation improvements, and applications to different fields of studies are constantly being proposed; for most recent progress see, among others, Eldredge (2008), Chatelain & Leonard (2008), Wee & Ghoniem (2008), Huberson *et al.* (2008), Lakkis & Ghoniem (2009) , and Huang *et al.* (2009).

The accuracy of vortex methods has been reported to compare well to non-dissipative and high-order, finite-difference schemes (see Ould-Salihi *et al.* 2000, Koumoutsakos 2005). In a homogeneous turbulent flow at low Reynolds number and a vortex reconnection case at moderate Reynolds number, the comparisons between spectral and vortex methods (Cottet *et al.* 2002) show that the vortex method is accurate enough to yield "acceptable statistics" in large and intermediate scales, and it appears to behave as accurately as LES models in the under-resolved scales "in the sense that they avoid accumulation of energy at the end of the spectrum, without excessive dissipation in the resolved scales".

As mentioned in Chapter 1, vortex methods have many advantages over conventional grid-based methods: (i) Vortex methods are free of convection-related stability conditions, so that time-step limitations are far less restrictive for vortex methods (see Anderson & Greengard 1985, and Cottet *et al.* 2002). Large time steps may be used and substantial savings of computational time over grid-based methods can be achieved (see also Koumoutsakos 2005); (ii) The vorticity field that needs to be solved usually

exists only in small fractions of the whole flow field, and hence, considerable savings in computational costs may be achieved; (iii) Far-field boundary conditions are automatically satisfied for vortex particles with a compact support so there is no need for a large computational domain to minimize blockage effects; (iv) The interactions between computational elements mimic the physics they represent so that no additional criteria for "critical parts" of the flow (which are not always known *a priori*) are necessary (Beale & Majda 1982ab, Koumoutsakos 2005); (v) Vortex methods are based on Lagrangian formulations, so there is no numerical diffusion associated with convection, and the dynamics are not constrained by a prescribed minimum scale.

2.2. BASIC FORMULATION

In a non-rotating frame of reference, the vorticity in an incompressible fluid with uniform viscosity and conservative body forces is governed by the vorticity equation

$$\frac{D\boldsymbol{\omega}}{Dt} = (\boldsymbol{\omega}\cdot\nabla)\mathbf{U} + \nu\nabla^2\boldsymbol{\omega} \tag{2-1}$$

with ν being the kinematic viscosity of the fluid, and D/Dt the material derivative

$$\frac{D\boldsymbol{\omega}}{Dt} \equiv \frac{\partial\boldsymbol{\omega}}{\partial t} + (\mathbf{U}\cdot\nabla)\boldsymbol{\omega}$$

$\mathbf{U} = u\hat{\mathbf{i}} + v\hat{\mathbf{j}} + w\hat{\mathbf{k}}$ and $\boldsymbol{\omega} = \omega_x\hat{\mathbf{i}} + \omega_y\hat{\mathbf{j}} + \omega_z\hat{\mathbf{k}}$ are the velocity and vorticity vectors, respectively,

$$\mathbf{U}(\mathbf{r},t) = \frac{d\mathbf{r}}{dt},\ \boldsymbol{\omega} = \nabla\times\mathbf{U}$$

where $\mathbf{r} = x\hat{\mathbf{i}} + y\hat{\mathbf{j}} + z\hat{\mathbf{k}}$ is the position vector. The first term on the right-hand side of Equation (2-1) represents the stretching and tilting of the vortices by the strain rate,

which vanishes in a two-dimensional (2-D) flow. That is, for a 2-D incompressible homogenous flow, we have

$$\frac{\partial \omega}{\partial t} + (\mathbf{U} \cdot \nabla)\omega = \nu \nabla^2 \omega \tag{2-2}$$

in which ω has been used instead of ω_z for simplicity.

Consider a rigid body immersed in an incompressible flow with freestream velocity $\mathbf{U}_\infty$ and zero initial vorticity, the boundary conditions to be satisfied are:

- The no-slip boundary condition at the solid boundary ($\partial\mathcal{D}$)

$$\mathbf{U}(\mathbf{r}_s, t) = \mathbf{U}_s(\mathbf{r}_s, t) \text{ on } \partial\mathcal{D} \tag{2-3}$$

  where $\mathbf{r}_s$ is the position vector on the surface of the body, and $\mathbf{U}_s(\mathbf{r}_s,t)$ is the body velocity at $\mathbf{r}_s$. The no-slip boundary condition is commonly decomposed into two parts: the no-through flow boundary condition

$$\mathbf{U} \cdot \hat{\mathbf{n}} = \mathbf{U}_s \cdot \hat{\mathbf{n}} \quad (\text{on } \partial\mathcal{D}) \tag{2-4}$$

  and the no-slip boundary condition

$$\mathbf{U} \cdot \hat{\mathbf{t}} = \mathbf{U}_s \cdot \hat{\mathbf{t}} \quad (\text{on } \partial\mathcal{D}) \tag{2-5}$$

  where $\hat{\mathbf{n}}$ and $\hat{\mathbf{t}}$ are the unit normal vector and the unit tangential vector on the body surface, respectively.

- The far field boundary condition

$$\mathbf{U} \to \mathbf{U}_\infty \text{ (at } \mathbf{r} \to \infty) \tag{2-6}$$

2.3. NUMERICAL SCHEMES AND IMPLEMENTATION

2.3.1. The Biot-Savart Law

To solve the vorticity equation, Poisson's equation for incompressible flows is often used,

$$\nabla^2 \mathbf{U} = -\nabla \times \boldsymbol{\omega} \tag{2-7}$$

With Green's function for the 2-D Laplace operator

$$G(\mathbf{r}) = -\frac{\ln|\mathbf{r}|}{2\pi} \tag{2-8}$$

a solution to Equation (2-7) can be expressed as

$$\mathbf{U}(\mathbf{r},t) = \mathbf{U}_\infty + \int_{\mathcal{D}} \nabla G(\mathbf{r}-\mathbf{r}') \times \boldsymbol{\omega}(\mathbf{r}',t) dA = \mathbf{U}_\infty + \mathbf{K} * \omega \tag{2-9}$$

where the 2-D Biot-Savart kernel $\mathbf{K}$ is given by

$$\mathbf{K}(\mathbf{r}) = \frac{\hat{\mathbf{k}} \times \mathbf{r}}{2\pi r^2} \tag{2-10}$$

in which $r = |\mathbf{r}|$, and the symbol "*" in Equation (2-9) denotes convolution over the domain $\mathcal{D}$. Equation (2-9) is the well-known Biot-Savart law.

2.3.2. The Vortex Particle Discretization

In modern vortex methods (see Cottet & Koumoutsakos 2000), the vorticity field is usually discretized into the sum of many vortex particles of finite sizes

$$\omega(\mathbf{r},t) \approx \sum_{i=1}^{N} \Gamma_i(t) \eta_\sigma(\mathbf{r} - \mathbf{r}_i(t)) \tag{2-11}$$

with $\mathbf{r}_i(t)$, $\Gamma_i(t)$ and σ_i being the position, strength (circulation), and core size of particle i. $\eta_\sigma(\mathbf{r})$ describes the distribution of the vorticity of the particles,

$$\eta_\sigma(\mathbf{r}) = \frac{1}{\sigma^2}\eta\left(\frac{r}{\sigma}\right) \tag{2-12}$$

where the cutoff function $\eta(r)$ is usually chosen to be radially symmetric. Compared to the traditional point vortex method (vortices of zero size), the finite sizes of the particles eliminate the instability that arises from the direct use of Equation (2-9) when two vortices approach each other. The core sizes σ_i are often chosen to be uniform ($\sigma_i = \sigma$), although they may change with time. Inserting Equation (2-11) into Equation (2-9) yields

$$\mathbf{U}(\mathbf{r},t) \approx \mathbf{U}_\infty + \sum_{i=1}^{N} \mathbf{K}_\sigma(\mathbf{r}-\mathbf{r}_i)\Gamma_i(t) \tag{2-13}$$

where the mollified Biot-Savart kernel $\mathbf{K}_\sigma$ is given by the convolution of the Biot-Savart kernel $\mathbf{K}$ and the cutoff function $\eta_\sigma(\mathbf{r})$

$$\mathbf{K}_\sigma(\mathbf{r}) = \mathbf{K}(\mathbf{r}) * \eta_\sigma(\mathbf{r}) \tag{2-14}$$

Gaussian cutoff functions are commonly used due to their smoothness and fast decay (although they are also more expensive to compute),

$$\eta(r) = \frac{1}{k\pi}\exp\left(-\frac{r^2}{k}\right) \tag{2-15}$$

where the constant k is determines the cutoff width. Different values of k, mostly 1, 2 or 4, have been suggested in the literature, see Barba (2004) for a brief discussion. In the present study, $k = 2$ is used, as suggested by Barba. Now $\mathbf{K}_\sigma$ can be obtained analytically

$$\mathbf{K}_\sigma(\mathbf{r}) = \frac{\hat{\mathbf{k}}\times\mathbf{r}}{2\pi r^2}\left[1-\exp\left(-\frac{r^2}{k\sigma^2}\right)\right] \tag{2-16}$$

Equation (2-13) will be referred to as the (discrete) Biot-Savart law in the present study.

Convergence of the above smoothed vortex particle descretization has been well established through extensive studies in the literature (see Hald 1979, 1987, Beale &

Majda 1982ab, Anderson & Greengard 1985, Cottet & Koumoutsakos 2000), based on some assumptions about the core size and the cutoff function. The core size is assumed to be related to the distance between vortex particles, h, as follows

$$\sigma = h^q \quad (0 < q < 1) \tag{2-17}$$

This means vortex particles must overlap, which may be more conveniently controlled by an overlap ratio, β

$$\beta \equiv h/\sigma < 1 \tag{2-18}$$

The chosen cutoff function, given by Equation (2-15), satisfies all the requirements (see the aforementioned references for details), and the error introduced by the discretization of Equation (2-11) is of order $\mathcal{O}(\sigma^2)$. It has been shown by Perlman (1985) that, in non-smooth vorticity fields, higher-order cutoff functions will not provide any advantage in accuracy. The truncation error due to the mollification contributes to enstrophy production and creation of small vortical structures in high strain regions (Cottet 1996, Koumoutsakos 2005), which may be compensated for by adding an "artificial viscosity" (Cottet 1996) or occasional re-regularization of the particle positions.

The convergence analysis for discrete time advancing of vortex methods is given in Anderson & Greengard (1985). It is shown that the error associated with time discretization is of order $\mathcal{O}(\Delta t^k)$ if a kth-order time-stepping scheme is employed. What is remarkable is that the convergence is unconditional, or in other words, there is no stability condition relating the size of time step to the grid size as suffered by grid-based methods. However, in order to achieve a well resolved simulation, the following constraints on Δt are often suggested (see Ploumhans & Winckelmans 2000, Barba 2004):

$$|\omega|_{\max} \Delta t = \mathcal{O}(1) \tag{2-19}$$

to ensure that particles do not rotate too much with respect to one another in one time step, and

$$\nu\Delta t/h^2 = \mathcal{O}(1) \tag{2-20}$$

in order to simulate the diffusion effects accurately. Eldredge (2007) further suggests that, in order to allow the thickness of the temporal boundary layer created during each time step, which is of the scale of $\sqrt{4\nu\Delta t}$, to extend at least one particle spacing, it is necessary to impose a lower bound on Δt. His numerical analysis leads to the following recommendation:

$$0.2 < \nu\Delta t/h^2 < 1.2 \tag{2-21}$$

2.3.3. The Fractional-Step Algorithm

First introduced by Chorin (1973) into viscous vortex methods, viscous splitting, or the fractional-step method, has been one of the most popular algorithms in the studies using this method. This is perhaps because it is straightforward to implement, and convergent for both bounded and unbounded flows (Beale & Majda 1981, Alessandrini *et al.* 1983, Ying 1987, 1990, Cottet & Koumoutsakos 2000).

In numerical simulations, the evolution of the flow is treated in discrete time steps. The viscous splitting algorithm considers the convection and diffusion of vorticity successively in multiple substeps. Although more than two substeps may be used to increase the accuracy, the standard and commonly accepted two-step algorithm is used in the present numerical scheme. Suppose that we have finished the computation for the (n-1)th time step, and we are seeking to advance the solution to the next time step, $t = n\Delta t$

(with Δt the size of the time step). Following Cottet & Koumoutsakos (2000), the fractional-step algorithm is implemented in the present study as follows:

- **Substep 1**: using the results from $t = t\text{-}\Delta t$ as the initial conditions, the local velocity is computed by the Biot-Savart law and integrated to convect the vortex particles (see Section 2.3.4), and their strengths are updated through diffusion (see Section 2.3.5). A spurious slip velocity, $\Delta\mathbf{U}_{slip}$ (see Section 2.3.7), will be observed at the solid boundary at the end of this substep, but no boundary condition is explicitly enforced in this substep.

- **Substep 2**: a surface vortex sheet, $\Delta\gamma$, is computed by enforcing the kinematic boundary condition (see Section 2.3.7) to cancel the slip velocity $\Delta\mathbf{U}_{slip}$ obtained in substep 1. The vortex sheet is then diffused into the vorticity field (see Section 2.3.7), which is equivalent to enforcing the no-slip boundary condition.

The two-step viscous splitting algorithm is second-order accurate at each substep, but is first-order accurate overall, irrespective of the time-stepping scheme used (see Beale & Majda 1981, Cottet & Koumoutsakos 2000).

2.3.4. Convection

Particle positions, $\mathbf{r}_i(t)$, can be determined from the following differential equations

$$\frac{d\mathbf{r}_i}{dt} = \mathbf{U}(\mathbf{r}_i, t), \quad i = 1..N \tag{2-22}$$

where N is the number of particles used in the computation to simulate the vorticity field, and $\mathbf{U}(\mathbf{r}_i, t)$ may be obtained using Equation (2-13). However, the direct use of Biot-Savart law involves $\mathcal{O}(N^2)$ computation, which is prohibitive in high resolution

simulations where N may be of the order of a million. In the present work, the adaptive fast multipole method (Barnes & Hut 1986, Greengard & Rokhlin 1987, Carrier *et al.* 1988) is implemented, which reduces the operation count to $\mathcal{O}(N)$. A second-order Runge-Kutta (RK2) scheme is chosen in the present study to integrate the velocity over time.

2.3.5. Diffusion

The diffusion of the vorticity field, in the frame work of viscous splitting, is governed by

$$\frac{\partial \omega}{\partial t} = \nu \nabla^2 \omega \tag{2-23}$$

Many schemes to approximate the above viscous diffusion in vortex methods have been proposed since Chorin (1973) first introduced his famous random walk method. Due to its "numerical convenience" (Sarpkaya 1989), the random walk method has been the most widely used scheme, especially in engineering applications, although the accuracy is limited by the statistical nature of the scheme. The particle strength exchange (PSE) method (Degond & Mas-Gallic 1989) is more popular in academic studies of "high-resolution" vortex methods (see, e.g., Koumoutsakos & Leonard 1995, Ploumhans & Winckelmans 2000, Barba 2004, Eldredge 2007). To solve Equation (2-23), the basic idea of PSE is to use an integral operator to approximate the Laplacian (Degond & Mas-Gallic 1989):

$$\nabla^2 \omega(\mathbf{r}) \approx \frac{1}{\varepsilon^2} \int_{\mathcal{D}} \zeta_\varepsilon(\mathbf{r}-\mathbf{r}') \left[\omega(\mathbf{r}') - \omega(\mathbf{r})\right] dA \tag{2-24}$$

where $\mathcal{D}$ is the entire computational domain, and ε is a scaling parameter which satisfies the stability inequality

$$\nu \le C_s \varepsilon^2 \tag{2-25}$$

with C_s being a positive constant. $\zeta_\varepsilon(\mathbf{r})$ is a smoothing function dependent on the parameter ε such that

$$\zeta_\varepsilon(\mathbf{r}) = \frac{1}{\varepsilon^2}\zeta\left(\frac{\mathbf{r}}{\varepsilon}\right) \tag{2-26}$$

in which the 2-D cutoff function $\zeta(\mathbf{r})$ satisfies the following moment conditions

$$\begin{cases} \int_{\mathcal{D}} x^2 \zeta(\mathbf{r}) dA = 2 \\ \int_{\mathcal{D}} y^2 \zeta(\mathbf{r}) dA = 2 \\ \int_{\mathcal{D}} x^{\alpha_1} y^{\alpha_2} \zeta(\mathbf{r}) dA = 0, \ \forall \alpha_i \in \mathbb{N}^2, 1 \le \alpha_1 + \alpha_2 \le m+1 \\ \int_{\mathcal{D}} r^{m+2} |\zeta(\mathbf{r})| dA < \infty \end{cases} \tag{2-27}$$

for an integer $m \ge 2$. The approximation introduces an error of $\mathcal{O}(\varepsilon^m)$. For convenience, a radially symmetric cutoff function, which satisfies Equation (2-27) for $m = 2$, may be constructed as follows (Degond & Mas-Gallic 1989)

$$\zeta(\mathbf{r}) = -\frac{2}{r}\frac{d}{dr}\eta(r) \tag{2-28}$$

where $\eta(r)$ is given by Equation (2-15) with $k = 2$. Let $\varepsilon = \sigma$, we have

$$\zeta_\varepsilon(\mathbf{r}) = 2\eta_\sigma(\mathbf{r}) \tag{2-29}$$

Assuming a uniform distribution of vortex particles with overlapping ratio $\beta \le 1$, Equation (2-24) may be discretized using particle locations as quadrature points, and Equation (2-23) may now be rewritten as

$$\frac{d\Gamma_i}{dt} \approx \frac{2\nu h^2}{\sigma^2}\sum_{j=1}^{N}(\Gamma_j - \Gamma_i)\eta_\sigma(\mathbf{r}_i - \mathbf{r}_j) \tag{2-30}$$

It can be inferred from Equation (2-30) that PSE scheme simulates diffusion effects by

exchanging strengths among particles, instead of modifying particle positions as in the random walk method. Although the method is formulated grid-free, the accuracy highly depends on the evaluation of the discretized integral, which requires a uniform distribution and overlap of particles. To meet this requirement, a remeshing step, where the particles are interpolated (remeshed) onto a regular grid, will be carried out every a few time steps (see Section 2.3.6).

In Equation (2-30), every particle will exchange strength with all other particles in the flow field, which may incur high computational costs. Thanks to the rapid decay of the smoothing function, only particles within a small radius, which can be easily determined by examining the smoothing function with a prescribed error tolerance, make significant contribution to the strength exchange. A radius of 5σ is typically used by other researchers (see, e.g., Ploumhans & Winckelmans 2000, and Barba 2004) and is chosen in the current implementation.

As pointed out in Ploumhans & Winckelmans (2000), particles very close to the solid boundary may "not be completely surrounded by other particles," which may lead to a spurious vorticity flux at the wall. Following the suggestions by Mas-Gallic (1995), Benhaddouch (1999), and Ploumhans & Winckelmans (2000), the method of image particles is adopted in the present implementation for particles within 5σ distance from the body to ensure zero vorticity flux at the boundary.

2.3.6. Remeshing

Numerical experiments (see Perlman 1985, and Barba 2004) have shown that the discretization accuracy deteriorates quickly due to the distortion of the particle

distribution and loss of particle overlap in areas of large strain, leading to spurious vortical structures in the flow. Also, as discussed in Section 2.3.5, the accuracy of PSE diffusion scheme relies on a uniform distribution and overlap of the particles. Several "remeshing" or "redistribution" schemes using high-order interpolation kernels have been designed to solve this problem (see Cottet & Koumoutsakos 2000, and Barba 2004 for reviews). In high-resolution vortex methods, the Λ_3 and M_4' interpolation kernels are chosen by most researchers for remeshing schemes:

$$\Lambda_3(u) = \begin{cases} \frac{1}{2}(1-u^2)(2-u) & \text{if } 0 \le u < 1, \\ \frac{1}{6}(1-u)(2-u)(3-u) & \text{if } 1 \le u < 2, \\ 0 & \text{otherwise} \end{cases} \tag{2-31}$$

$$M_4'(u) = \begin{cases} 1-\frac{5}{2}u^2+\frac{3}{2}u^3 & \text{if } 0 \le u < 1, \\ \frac{1}{2}(1-u)(2-u)^2 & \text{if } 1 \le u < 2, \\ 0 & \text{otherwise} \end{cases} \tag{2-32}$$

where $u = |\xi|$, with ξ being the normalized distance from the source particle. Both kernels require a 4-point wide stencil. The Λ_3 kernel is piecewise-cubic and conserves up to the third moment of vorticity, but it is not as smooth as the M_4' kernel, which is derived from B-splines (Monaghan 1985) and is also third-order accurate. In the present implementation, the M_4' kernel is the preferred interpolation kernel for remeshing, although the Λ_3 kernel is also implemented for comparison purposes.

For particles very close the solid boundary, some of the new particles within their interpolation stencil may fall inside the solid body, and hence, the direct use of the symmetric interpolation kernel may result in leakage of vorticity into the body. The common way to deal with this problem is to work with a body-fitted grid and/or use

asymmetric interpolation kernels near the boundary; see the remeshing techniques in Koumoutsakos & Leonard (1995), Cottet & Koumoutsakos (2000), and Ploumhans & Winckelmans (2000) for examples. Since we are dealing with bodies of general geometries in the present study, the concept of immersed boundary by Peskin (1972) is adopted, and the boundary intersects with the Cartesian remeshing grid in an arbitrary way. To avoid leaking vorticity in to the body, two asymmetric interpolation kernels conserving up to second (Λ_2') and third (Λ_3') moment of vorticity distribution, respectively, are constructed:

$$\Lambda_3'(\xi)=\begin{cases}\frac{1}{6}\xi(\xi-1)(2-\xi) & \text{if } -1\le\xi<0,\\ \frac{1}{2}(\xi-1)(\xi-2)(\xi+1) & \text{if } 0\le\xi<1,\\ \frac{1}{2}\xi(\xi+1)(2-\xi) & \text{if } 1\le\xi<2,\\ \frac{1}{6}\xi(\xi-1)(\xi-1) & \text{if } 2\le\xi<3,\\ 0 & \text{otherwise}\end{cases} \tag{2-33}$$

$$\Lambda_2'(\xi)=\begin{cases}\frac{1}{2}(1-\xi)(2-\xi) & \text{if } 0\le\xi<1,\\ \xi(2-\xi) & \text{if } 1\le\xi<2,\\ \frac{1}{2}\xi(\xi-1) & \text{if } 2\le\xi<3,\\ 0 & \text{otherwise}\end{cases} \tag{2-34}$$

When remeshing involves a particle near the boundary, an inside-body test is first performed on all the 16 points of the symmetric stencil. If all new particles are outside the body, the symmetric kernel is used. If any of the new particles falls inside the body, the remeshing then proceeds in two substeps as suggested by Ploumhans & Winckelmans (2000). In the first substep, an interpolation kernel is selected to redistribute particles in the x-direction only, without creating new particles inside the body, and temporary particles are created at appropriate locations. Each of the temporary particles is then redistributed in the y-direction with a carefully selected kernel. When selecting an

interpolation kernel, M_4' (or Λ_3) is used if possible. But if it creates new particles inside the body, Λ_3' is then tested. If Λ_3' still leaks vorticity into the body, Λ_2' is then selected. A "penalty" p_i (Ploumhans & Winckelmans 2000) is calculated for each new particle:

$$p_i = \begin{cases} 0 \text{ if symmetric kernels are used in both directions,} \\ 1 \text{ if an asymmetric kernel is used in eighter } x\text{- or } y\text{-direction,} \\ 2 \text{ if asymmetric kernels are used in both directions} \end{cases} \quad (2\text{-}35)$$

A "global penalty" P_{XY} is then obtained as the average value of p_i. A "global penalty" P_{YX} is then calculated in the next substep by redistribute the particle first in the y-direction and then in the x-direction. If $P_{XY} \leq P_{YX}$, the remeshing result from the first substep is used as the final result, or else the result from the second substep is chosen.

2.3.7. Boundary Conditions

The far field boundary condition, Equation (2-6), is automatically satisfied in a vortex particle system described above, hence, only the boundary conditions at the fluid-solid interface need to be considered.

2.3.7.1. Kinematic boundary condition

In the present study, we are interested in a stationary rigid body immersed in an incompressible flow with freestream velocity $\mathbf{U}_\infty$ and zero initial vorticity. To describe the vorticity boundary conditions, the surface of the body is represented by a surface vortex sheet (bound vortex) of strength $\gamma(\mathbf{r}_s)$, the velocity field associated with the vortex sheet, $\mathbf{U}_\gamma$ is given by (Cottet & Koumoutsakos 2000)

$$\mathbf{U}_\gamma(\mathbf{r}) = \pm\frac{1}{2}\gamma(\mathbf{r}_s)\hat{\mathbf{t}}(\mathbf{r}_s) + \oint_{\partial\mathcal{D}} \gamma(\mathbf{r}_s)\nabla G(\mathbf{r}-\mathbf{r}_s)\times\hat{\mathbf{k}}ds \tag{2-36}$$

in which the + or – sign is used when we approach the surface from outside or inside of the body, respectively. By matching the tangential component of the total velocity at the interior side of the surface with that of the body velocity, we get

$$-\frac{\gamma(\mathbf{r}_s)}{2} + \oint_{\partial\mathcal{D}} \gamma(\mathbf{r})\frac{\partial}{\partial n}G(\mathbf{r}_s-\mathbf{r})ds = -\Delta\mathbf{U}_{slip}(\mathbf{r}_s,t)\cdot\hat{\mathbf{t}}(\mathbf{r}_s) \tag{2-37}$$

where the normal vector is into the body, and

$$\Delta\mathbf{U}_{\text{slip}}(\mathbf{r}_s,t) = \mathbf{U}(\mathbf{r}_s,t) - \mathbf{U}_s(\mathbf{r}_s,t) \tag{2-38}$$

Equation (2-37) is a Fredholm integral equation of the second kind. A Fredholm integral equation of the first kind may also be obtained by matching the normal components of the velocities on the exterior side of the vortex sheet

$$\oint_{\partial\mathcal{D}} \gamma(\mathbf{r})\nabla G(\mathbf{r}_s-\mathbf{r})\cdot\hat{\mathbf{t}}(\mathbf{r}_s)ds = \Delta\mathbf{U}_{\text{slip}}(\mathbf{r}_s,t)\cdot\hat{\mathbf{n}}(\mathbf{r}_s) \tag{2-39}$$

However, as pointed out by Koumoutsakos (1993) and Cottet & Koumoutsakos (2000), the latter often leads to ill-conditioned systems of equations when discretized, and, hence, Equation (2-37) is employed in the present study. In addition to Equation (2-37) or (2-39), the strength of the vortex sheet must satisfy Kelvin's theorem of circulation conservation (Wu 1981, Koumoutsakos 1993, Koumoutsakos *et al.* 1994)

$$\oint_{\partial\mathcal{D}} \Delta\gamma(s)ds + \sum_{i=1}^{N}\Gamma_i(t) = 0 \tag{2-40}$$

2.3.7.2. The panel method

Equations (2-37) or (2-39) may be solved with the panel method (see Katz & Plotkin 2001, and Kuethe & Chow 1986). In the present implementation, the body surface is

discretized into M linear panels of constant strengths. Boundary conditions are to be enforced at the center points of these panels, and the panel-averaged slip velocity $\bar{\mathbf{U}}_{\text{slip}}(\mathbf{r}_s, t)$ (obtained using Gaussian quadrature) is used instead of $\mathbf{U}_{\text{slip}}(\mathbf{r}_s, t)$ for better accuracy (Koumoutsakos 1993, Ploumhans & Winckelmans 2000, Eldredge 2007). This leads to a system of M linear equations with M unknowns

$$[\mathbf{C}]\{\gamma\} = \{\mathbf{b}\} \tag{2-41}$$

where [**C**] is the coefficient matrix depending on the body geometry. Furthermore, the constraint imposed by Equation (2-40) must also be satisfied, hence we now have an over-determined system of linear equations. Usually they are solved in a least squares sense (see, e.g., Morgenthal 2002 and Eldredge 2007). However, as suggested Ploumhans & Winckelmans (2000), Equation (2-40) should be satisfied exactly, and hence, we need to solve a linear equality-constrained least-squares problem. Note that for a rigid body, the matrix [**C**] in Equation (2-41) does not change over time. In the present study, the linear equality-constrained least-squares problem is solved in two steps. All the computations that only involve [**C**] are finished at the beginning of the simulation, and only the computations involve the changing right hand side value in Equation (2-40) and the vector {**b**} in Equation (2-41) need to be repeated in each time step.

2.3.7.3. Diffusion of the surface vortex sheet

Once the vortex sheet strength is obtained, it is diffused into the fluid with homogenous initial conditions (keep in mind that this diffusion occurs during the second substep in the fractional-step algorithm, where the initial vorticity field has been taken into account in

the first substep) and a Neumann-type vorticity boundary condition (Koumoutsakos *et al.* 1994, Mas-Gallic 1995)

$$\begin{cases} \dfrac{\partial \omega'}{\partial t} = \nu \nabla^2 \omega' & \text{on } \mathcal{D} \times [0, \Delta t] \\ \omega'(\mathbf{r}, 0) = 0 & \text{on } \mathcal{D} \\ \nu \dfrac{\partial \omega'}{\partial n} = -\dfrac{\gamma(\mathbf{r}_s)}{\Delta t} & \text{on } \partial\mathcal{D} \times [0, \Delta t] \end{cases} \tag{2-42}$$

where the normal vector is into the fluid. As pointed out by Koumoutsakos *et al.*, the nullification of this spurious vortex sheet at the body surface eliminates the spurious slip velocity present at the boundary and generates vorticity in the fluid, which is equivalent to enforcing the no-slip boundary condition (see also Lighthill 1963). Following Koumoutsakos *et al.* (1994) and Cottet & Koumoutsakos (2000), the solution to Equation (2-42) can be expressed in integral form (see Friedmann 1964) as

$$\omega'(\mathbf{r}, t) = \int_0^t \int_{\partial\mathcal{D}} \mathcal{G}(\mathbf{r} - \mathbf{r}', t - \tau) \mu(\mathbf{r}', \tau) ds_{\mathbf{r}'} d\tau \tag{2-43}$$

where the 2-D heat kernel $\mathcal{G}(\mathbf{r},t)$ is given by

$$\mathcal{G}(\mathbf{r}, t) = \frac{1}{4\pi\nu t} \exp\left(-\frac{|\mathbf{r}|^2}{4\nu t} \right)$$

and the surface density $\mu(\mathbf{r},t)$ is determined from

$$-\frac{1}{2}\mu(\mathbf{r}, t) + \nu \int_0^t \int_{\partial\mathcal{D}} \frac{\partial}{\partial n} \mathcal{G}(\mathbf{r} - \mathbf{r}', t - \tau) \mu(\mathbf{r}', \tau) ds_{\mathbf{r}'} d\tau = -\frac{\gamma(\mathbf{r})}{\Delta t} \tag{2-44}$$

The discretization of the boundary into linear panels described in Section 2.3.7.2 is re-used here to solve Equation (2-43). Assuming that $\mu(\mathbf{r},t)$ remains constant over the small time interval Δt and takes a constant value over each panel, Equation (2-43) can be

integrated analytically, and the vorticity field induced by the ith panel, centered at $\mathbf{r}_i$ with length λ_i, is then given by

$$\omega_i'(\mathbf{r},\Delta t)=\frac{\mu_i}{2}\int_0^{\Delta t}\phi_i(\mathbf{r},t)dt \tag{2-45}$$

In a local coordinate system of the panel i where $x'=(\mathbf{r}-\mathbf{r}_i)\cdot\hat{\mathbf{t}}_i$, $y'=(\mathbf{r}-\mathbf{r}_i)\cdot\hat{\mathbf{n}}_i$, $\phi_i(\mathbf{r},t)$ is expressed as

$$\phi_i(\mathbf{r},t)=\frac{1}{\sqrt{4\pi\nu t}}\exp\left(-\frac{y'^2}{4\nu t}\right)\left[\operatorname{erf}\left(\frac{x'+\lambda_i/2}{\sqrt{4\nu t}}\right)-\operatorname{erf}\left(\frac{x'-\lambda_i/2}{\sqrt{4\nu t}}\right)\right] \tag{2-46}$$

An approximate solution to Equation (2-44) is given in Koumoutsakos *et al.* (1994) and Cottet & Koumoutsakos (2000), by adopting the approximations suggested by Greengard & Strain (1990) to exploit the locality of the heat kernel $\mathcal{G}(\mathbf{r},t)$

$$\mu(\mathbf{r}_s)\approx\frac{2\gamma(\mathbf{r}_s)/\Delta t}{1-\kappa(\mathbf{r}_s)\sqrt{\pi\nu\Delta t/2}} \tag{2-47}$$

with $\kappa(\mathbf{r}_s)$ being the local curvature of the boundary. μ_i is assumed to be constant over panel i, on a flat panel it follows that

$$\mu_i\approx 2\gamma(\mathbf{r}_i)/\Delta t \tag{2-48}$$

With Equations (2-45)-(2-48), the amount of circulation $\Delta\Gamma_{ij}$ to be diffused from vortex panel i to particle j with an associated fluid area A_j in one time step can be expressed as

$$\Delta\Gamma_{ij}=\int_{A_j}\omega_i'(\mathbf{r},\Delta t)dA_j=\frac{\gamma(\mathbf{r}_i)}{\Delta t}\int_0^{\Delta t}\int_{A_j}\phi_i(\mathbf{r},t)dA_j dt \tag{2-49}$$

In Koumoutsakos *et al.* (1994) and Cottet & Koumoutsakos (2000) the spatial integration in Equation (2-49) is simply evaluated by treating ϕ_i as constant over the fluid area, and the time integral is carried out using a mid-point rule. It is argued in Leonard *et al.* (1997)

and Ploumhans & Winckelmans (2000) that these approximations are a source of accuracy loss. For square fluid areas (of size h_j) aligned with the local coordinate system of the panel i, the spatial integration in Equation (2-49) can be carried out exactly:

$$\int_{A_j} \phi_i(\mathbf{r},t)dA_j = \frac{1}{2}\left[\alpha_i\left(x_j'+\frac{h}{2},t\right)-\alpha_i\left(x_j'-\frac{h}{2},t\right)\right]\left[\beta\left(y_j'+\frac{h}{2},t\right)-\beta\left(y_j'-\frac{h}{2},t\right)\right] \quad (2\text{-}50)$$

where

$$\alpha_i(x,t) = \eta\left(x+\frac{\lambda_i}{2},t\right)-\eta\left(x-\frac{\lambda_i}{2},t\right),\ \beta(x,t) = \operatorname{erf}\left(\frac{x}{\sqrt{4\nu t}}\right)$$

and

$$\eta(x,t) = x\operatorname{erf}\left(\frac{x}{\sqrt{4\nu t}}\right)+\sqrt{\frac{4\nu t}{\pi}}\exp\left(-\frac{x^2}{4\nu t}\right)$$

For particles at a distance $y_j' < h$ from the panel, Equation (2-50) may be rewritten as

$$\int_{A_j} \phi_i(\mathbf{r},t)dA_j = \frac{1}{2}\left[\alpha_i\left(x_j'+\frac{h}{2},t\right)-\alpha_i\left(x_j'-\frac{h}{2},t\right)\right]\beta\left(y_j'+\frac{h}{2},t\right) \quad (2\text{-}51)$$

Ploumhans & Winckelmans further suggest that, to exactly conserve the circulation, the following correction be made to the circulation assigned to particle j

$$\Delta\Gamma_{ij}' = \Delta\Gamma_{ij} + \frac{\left(\Delta\Gamma_{ij}\right)^2}{\sum_j\left(\Delta\Gamma_{ij}\right)^2}\left[\lambda_i\gamma(\mathbf{r}_i)-\sum_j\Delta\Gamma_{ij}\right] \quad (2\text{-}52)$$

In the present work, the time integration Equation (2-49) will be computed by Gaussian qudrature (3 or 4 points as suggested by Ploumhans & Winckelmans 2000), and the spatial integration will be evaluated according to Equations (2-50)-(2-52). The resulting field ω' will be added to the solution in the first substep to yield the complete vorticity distribution at the beginning of next time step.

2.3.8. Particle Population Control

The particle population is controlled by creation and deletion according to the following criteria (with suggestions from Morgenthal 2002, and Eldredge 2007):

- New particles are only created from interpolation stencils in the remeshing step;
- Particles within a prescribed distance, $c_b h$, of the body are deleted, and their strengths are recorded and later added to Equation (2-40). This is suggested by Eldredge (2007) to avoid singularities which arise in the interactions between vortex panels and particles when they become too close to each other. c_b is set at 0.5 in the present study, as suggested by Eldredge;
- Particles with strengths below a prescribed threshold, $\Gamma_{min} = \epsilon_\Gamma \nu$, are removed from the flow field after each remeshing step;
- Particles outside the prescribed limits of the computational domain are deleted, and their strengths are recorded and later added to Equation (2-40).

2.3.9. Forces on the Body

For the flow field of interest, where there is no net vorticity and the no-through flow boundary condition is enforced, the net force on a stationary body can be expressed in terms of vorticity impulse (see Wu 1981, Saffman 1992)

$$\mathbf{F}_b = -\frac{d}{dt}\rho\int_{\mathcal{D}}(\mathbf{r}\times\boldsymbol{\omega})\,dA \tag{2-53}$$

In the context of the vortex method, the above equation can be written explicitly as

$$\mathbf{F}_b = -\rho\frac{d}{dt}\sum_{i=1}^{N}\mathbf{r}_i\times\Gamma_i\hat{\mathbf{k}} \tag{2-54}$$

As pointed out by Koumoutsakos (1993) and Koumoustakos & Leonard (1995), the linear impulse is conserved in the interpolation process, but its time derivative may not be. This can lead to some small high-frequency oscillations riding on the force curve. A smoothing scheme may be applied to the linear impulse history to remove the non-physical oscillations, if a smooth curve is desired.

2.4. VALIDATION OF THE CODE

2.4.1. Impulsively started circular cylinders

Due to numerous analytical and numerical studies, most notably by Collins & Dennis (1973a,b), and Bar-Lev & Yang (1975), and the extensive experiments by Bouard & Coutanceau (1980, referred to as BC80 hereafter), the early stage evolution of the flow around an impulsively started circular cylinder has been a popular benchmark problem for modern viscous vortex particle codes; see Koumoustakos & Leonard (1995, referred to as KL95 hereafter), Shankar (1996, referred to as SS96 hereafter), Ploumhans & Winckelmans (2000, referred to as PW00 hereafter), Lakkis & Ghoniem (2009, referred to as LG09 hereafter), and Huang *et al.* (2009) for examples. The code must cope with the challenge of a $1/\sqrt{T}$ singularity (see Collins & Dennis 1973b, and Bar-Lev & Yang 1975) at the beginning of the evolution, and high-resolution is necessary to resolve the details of the separation process at high Reynolds numbers.

In this section, the present simulation results for impulsively started circular cylinder at Re = 550, 3,000 and 9,500 will be validated against published data from other researchers. In the simulations, a circular cylinder with diameter, D, was placed in a

uniform flow, which was impulsively set into motion at the beginning of the simulation with velocity U_∞. Remeshing was carried out every 5 time steps, and other parameters for the simulations are summarized in Table 2.1.

Table 2.1. Simulation parameters for impulsively started circular cylinders

Parameter	$Re = 550$	$Re = 3{,}000$	$Re = 9{,}500$
Time step $\Delta T = U_\infty \Delta t/D$	0.005	0.005	0.005
Particle spacing h/D	4.264×10^{-3}	1.826×10^{-3}	1.026×10^{-3}
$\nu\Delta t/h^2$	0.5	0.5	0.5
Overlap ratio β	1.0	1.0	1.0
Number of panels	737	1721	3063
Cutoff ratio ϵ_Γ	1×10^{-3}	1×10^{-3}	1×10^{-4}

The time evolution of drag coefficient obtained from the simulation at $Re = 550$ is shown in Figure 2.1(a). The linear impulse was filtered by a 5-point moving average to smooth out the noise introduced by remeshing before the drag was computed. Also shown in Figure 2.1(a) are the numerical results from KL95, SS96, and PW00, all of which are also obtained with high-resolution vortex particle methods. Note that an interpolation scheme on body-fitted grids specially designed for circular cylinders was used by KL95 (see the discussions in PW00), and in SS96 the grid-free vorticity redistribution method was employed, and ghost vortices inside the body were included in drag calculations to improve accuracy (Graham 1980). The present result is almost indistinguishable from those from PW00 and SS96, and the comparison shows that the improvements in numerical schemes over those of KL95 suggested by PW00, which are also adopted in the present implementation, seem to make slight differences for $T > 1.0$.

To see if the present simulation is able to capture the singularity at the beginning of the evolution, and how it compares to the theoretical predictions, the time history of

the drag coefficient for $T < 0.3$ is plotted in Figure 2.1(b), in comparison to the short time analytical solution by Collins and Dennis (1973b, referred to CD73 hereafter), and the numerical results by SS96 and PW00. An additional simulation with a smaller time step $\Delta T = 0.0025$ is also reported in PW00, because their simulation with $\Delta T = 0.01$ is unable to capture the singularity at the beginning of the evolution. In this figure the linear impulse from the present simulation was smoothed with a 3-point moving average before calculating the drag. Note a smaller smoothing window was used here in order to reduce the shifting effect of the moving average. It can be observed that the present result follows the analytical solution very well for $T < 0.3$, and is almost indistinguishable from that by SS96. The present results also agrees well with those from the simulations by PW00 with $\Delta T = 0.0025$ and $\Delta T = 0.01$ for $T < 0.15$ and $T > 0.06$, respectively.

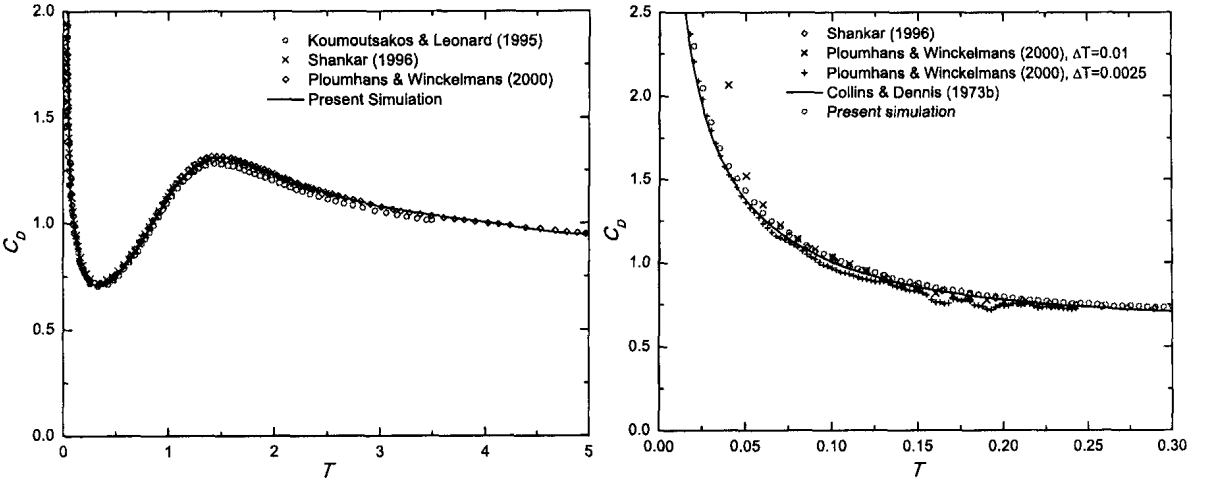

(a) (b)

Figure 2.1. Time history of drag coefficient for an impulsively started circular cylinder at Re = 550. (a), long-time evolution; (b), early stage evolution.

The early stage evolution of drag coefficient for $T < 0.5$ from the simulation at Re = 3,000 is presented in Figure 2.2(a), compared to the analytical solution by CD73, and

the numerical results by SS96 and PW00. To avoid the shifting effect of a moving average, the linear impulse from the present simulation was *not* smoothed before calculating the drag. Central difference was employed to calculate the time derivative, except before and after each remeshing step, where forward and backward differences were used, respectively. The "general scheme" in PW00 refers to the same remehsing scheme with a regular Cartesian lattice arbitrarily overlapping the boundary as in the present implementation, and "KL-like" scheme means that remeshing was performed on body-fitted grids as in KL95. The figure shows that the present result follows the analytical solution closely for $T < 0.5$, and, although all numerical results shown are in good agreement, the present result seems to match that of SS96 more closely at the early stage of evolution.

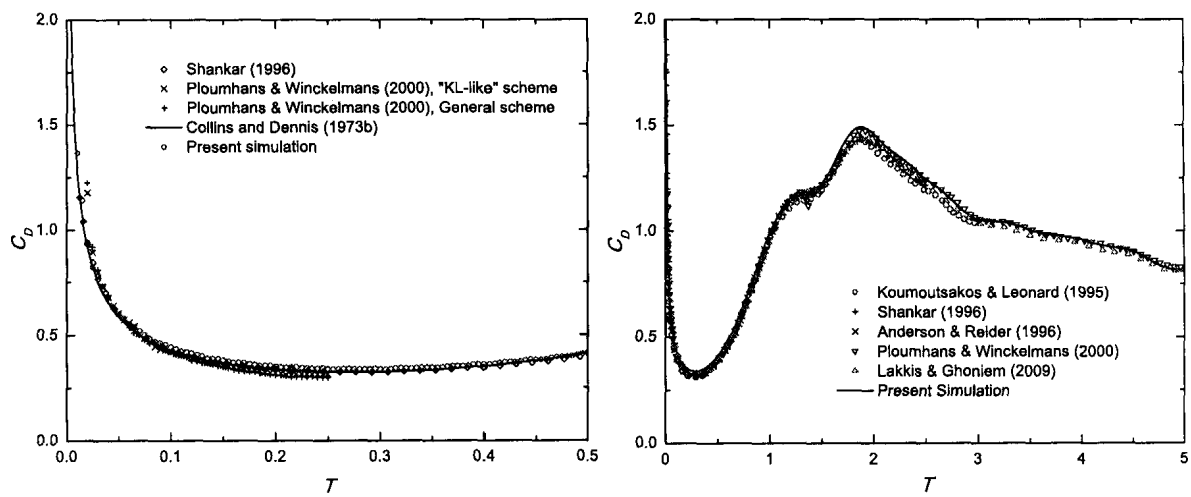

Figure 2.2. Time history of drag coefficient for an impulsively started circular cylinder at Re = 3,000. (a), early stage evolution; (b), long-time evolution.

Figure 2.2(b) shows the longer time evolution of drag coefficient for Re = 3,000, which was calculated from the linear impulse history filtered by a 5-point moving

average. The numerical results by KL95, SS96, Anderson & Reider (1996) (referred to as AR96 hereafter), PW00, and LG09 are also shown for comparisons. A fourth-order accurate (both special and temporal) finite-difference scheme was employed by AR96 to achieve their result, and a high-resolution vortex method with a grid-free scheme was used by LG09. The figure again shows that the present result is in excellent agreement with those obtained with various high resolution methods. Note that the sharp "dip" in the middle of the "plateau" at $T \approx 1.4$ on the drag curve from PW00 is not observed in the present result and those by other researchers.

Figure 2.3(a) presents the time history of drag coefficient for $T < 0.6$ at Re = 9,500, in comparison to the analytical solution by CD73, and the numerical results by SS96. The linear impulse from the present simulation was filtered by a 3-point moving average before calculating the drag. The comparisons show that the present result follows the analytical solution closely for $T < 0.6$, and is in good agreement with that of SS96.

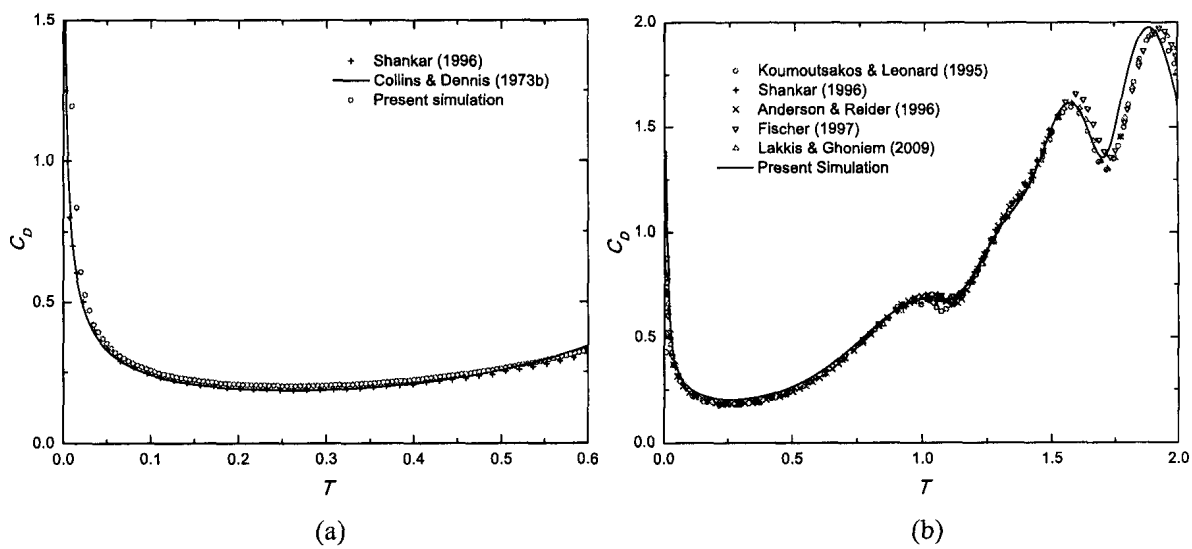

Figure 2.3. Time history of drag coefficient for an impulsively started circular cylinder at Re = 9,500. (a), early stage evolution; (b), long-time evolution.

In Figure 2.3(b), the longer time evolution of the drag coefficient obtained from the present simulation at Re = 9,500 is compared to the numerical results by KL95, AR96, SS96, Fischer (1997), and LG09. The drag curve from Fischer (1997) was obtained with a high-order spectral element method with mesh refinements in "critical regions". Generally, the present result compares very well with those by other researchers, especially for $T < 1.5$ where more data is available and all results are in excellent agreement. As discussed in KL95 the "plateau" at $T \approx 1$ is the "footprint" of the process in which the secondary vortex penetrates the primary one (see Figure 2.4). This "eruptive" phenomenon, which is considered to be the initiation of boundary-layer separation, was first discussed in Van Dommelen & Shen (1980). As pointed out by Van Dommelen & Shen (1980) and Doligalski *et al.* (1994), it is a challenging task for grid-based methods to resolve such a phenomenon, which develops very fast at a location not known *a priori,* and the "spike" narrows progressively (see Figure 2.4) during the process.

Figures 2.5-2.7 show comparisons between instantaneous streamlines from the present simulations and the experimental visualizations by BC80 at T = 2.5, 2.5, and 1.0, for Re = 550, 3,000, and 9,500, respectively. The flow visualizations from BC80 were realized by illuminating reflective or diffusive tracers in the flow. The present streamlines are contours of streamfunctions computed on a Cartesian grid during the simulations. As suggested by KL95, all the particles were treated as point vortices to ensure that the streamfunction value inside the body is constant. However, the use of a regular Cartesian grid, which overlaps the immersed boundary arbitrarily, may still lead to non-smoothness of the streamlines very close the body. An example of such errors may be observed by scrutinizing the "zero" streamline in Figure 2.5(b). Other than this cosmetic problem, the

present streamlines visually compare very well with the experimental results by BC80. The lengths of recirculation regions in the wake normalized by the cylinder diameter obtained from the present simulations for the three cases are, respectively, 0.82, 0.70, and 0.087, which are also in good agreement with 0.87, 0.73, and 0.088 determined from the experiments, correspondingly. These favorable comparisons indicate that the present simulations accurately captured the physics.

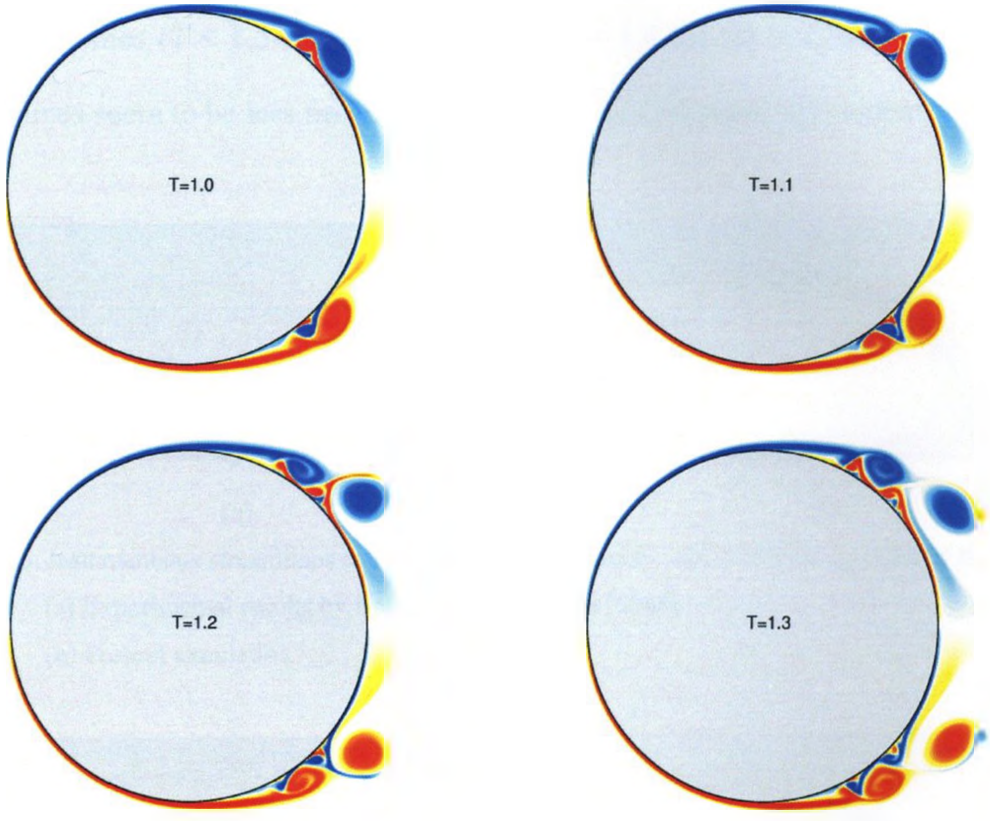

Figure 2.4. Vorticity field at T = 1.0-1.3 for an impulsively started circular cylinder at Re = 9,500.

In Figures 2.8-2.10 instantaneous streamwise velocities along the centerline in the wake obtained from the present simulations are compared with the experimental results by BC80, and the numerical results by SS96, for Re = 550, 3,000, and 9,500, respectively. The experimental data for Re = 3,000 and 9,500 were taken from Ta Phuoc Loc &

Bouard (1985). In the figures, the distance, x, is measured from the center of the cylinder. It can be observed that the present results closely match those from SS96, except some small discrepancies in the recirculation region. A further comparison in Figure 2.10 shows that the present results are almost indistinguishable from those by LG09 for Re = 9,500 at T = 1.5. For Re = 550, the present results are in good agreement with the experimental results, except for T = 0.5 and x/D > 1.2. For Re = 3,000 and 9,500, the agreement between the present simulations and the experiments by BC80 are very good for shorter times (T < 1.5 for Re = 3,000, and T < 1.4 for Re = 9,500). Comparisons at longer times seem to be less favorable, but are still in reasonable agreement.

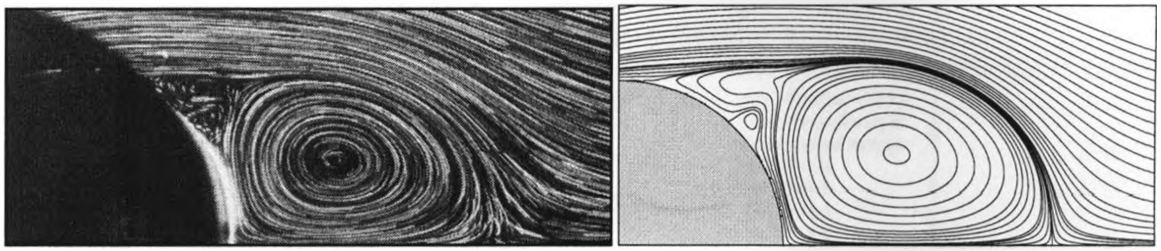

(a) (b)

Figure 2.5. Instantaneous streamlines at T = 2.5 for an impulsively started circular cylinder at Re = 550

(a) Experimental results by Bouard & Coutanceau (1980)

(b) Present simulation

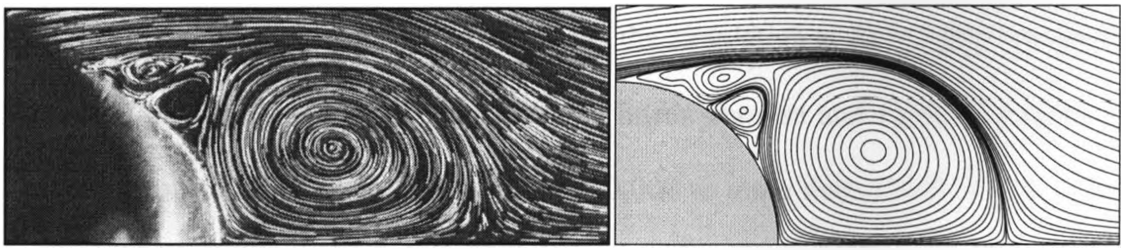

(a) (b)

Figure 2.6. Instantaneous streamlines at T = 2.5 for an impulsively started circular cylinder at Re = 3,000

(a) Experimental results by Bouard & Coutanceau (1980)

(b) Present simulation

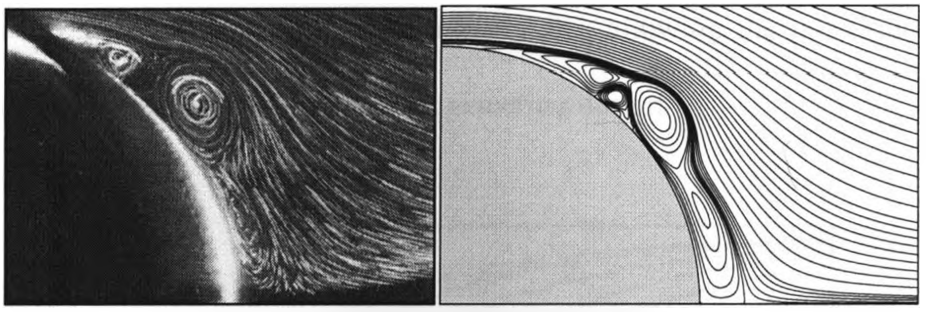

(a) (b)

Figure 2.7. Instantaneous streamlines at $T = 1.0$ for an impulsively started circular cylinder at $Re = 9{,}500$
(a) Experimental results by Bouard & Coutanceau (1980)
(b) Present simulation

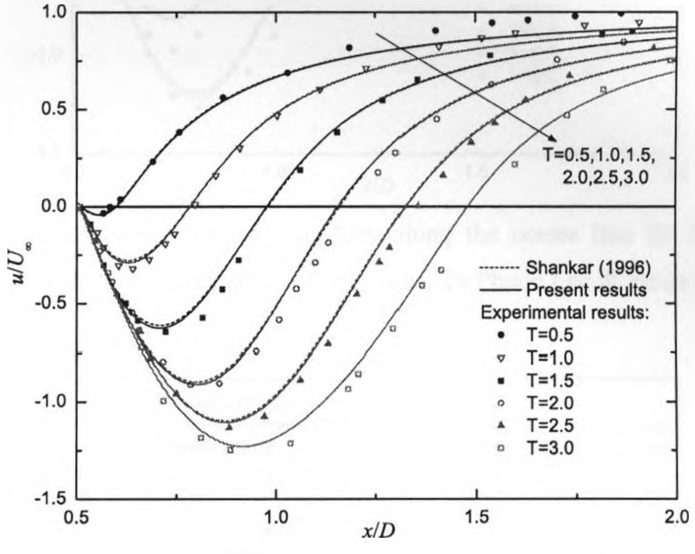

Figure 2.8. Instantaneous streamwise velocity profiles along the centre line for an impulsively started circular cylinder at $Re = 550$. Experimental data taken from Bouard & Coutanceau (1980).

To show the performance of the code, the simulation at $Re = 3{,}000$ was performed with only simple diagnostic output (such as linear impulse and force calculations). The number of particles increased from around 20,000 to more than 550,000 over 1,000 time steps, and the total run time was about 1.8 hours on a laptop computer with an Intel Core 2 Duo CPU running at 2.5 GHz (only one core was used). While KL95 had to perform such simulations on a supercomputer (Cray YMP) in 1995, and it took PW00 60 hours to run their simulation at $Re = 3{,}000$ on a workstation (DEC Alpha running at 533 MHz) in

2000, today these can be run on an ordinary PC, allowing the possibility to use such codes in the developmental stages for engineering design.

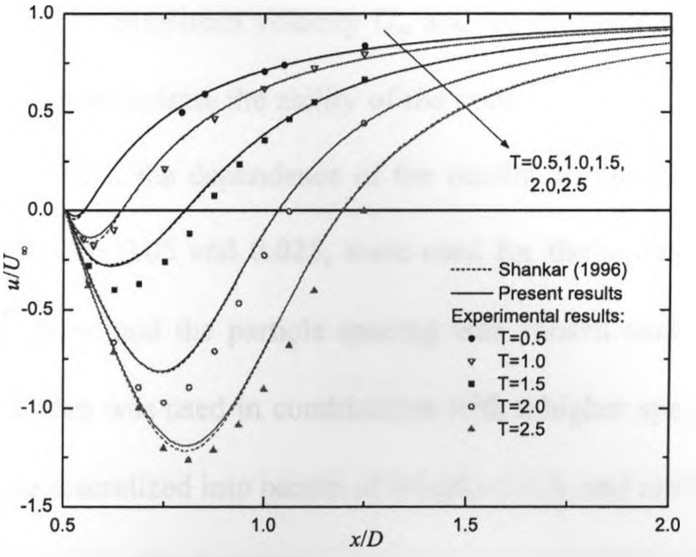

Figure 2.9. Instantaneous streamwise velocity profiles along the centre line for an impulsively started circular cylinder at Re = 3,000. Experimental data taken from Ta Phuoc Loc & Bouard (1985).

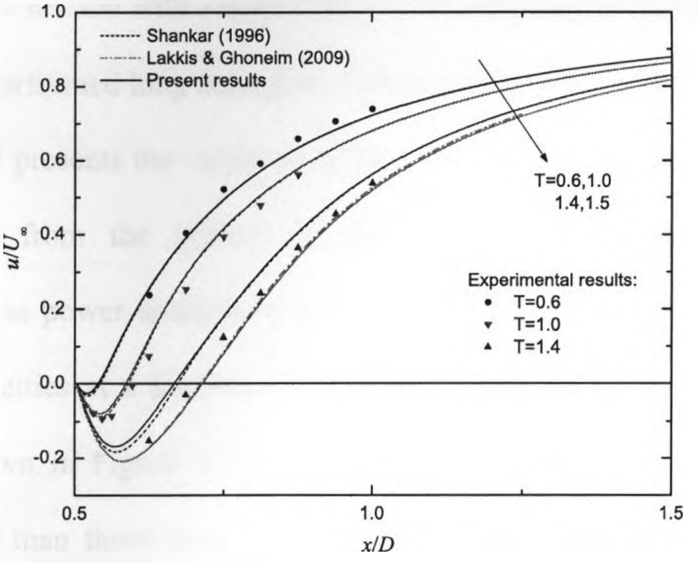

Figure 2.10. Instantaneous streamwise velocity profiles along the centre line for an impulsively started circular cylinder at Re = 9,500. Experimental data taken from Ta Phuoc Loc & Bouard (1985).

2.4.2. St-Re relationships for circular and square cylinders

In this Section, a series of simulations of flows around circular and square cylinders at Re = 50 – 600 (based on the freestream velocity U_∞ and the cross-stream dimension of the body) are presented to demonstrate the ability of the code to run long time simulations of bluff-body flows. To check the dependence of the results on numerical resolution, two different time steps, ΔT = 0.05 and 0.025, were used for the simulations. The overlap ratio, β, was set to unity, and the particle spacing was chosen such that $\nu\Delta t/h^2$ = 0.5, hence a smaller time step was used in combination with a higher spatial resolution. The solid boundaries were discretized into panels of lengths $\lambda \approx h$, and remeshing was carried out every 5 time steps. The sharp corners of the square cylinders were "rounded" with radius $r = \lambda$ as suggested by PW00 for better numerical behavior. The fluid was impulsively set into motion with velocity U_∞ at the beginning of the simulation, and the simulations were performed long enough to obtain 10-30 stable shedding cycles.

Figure 2.11 presents the variation of Strouhal number with Reynolds number for circular cylinders from the present simulations. The shedding frequencies were determined from the power spectral densities (PSD) of the lift time history as well as instantaneous velocities at a number of locations in the wake (see Figure 2.12 for an example). As shown in Figure 2.11, Strouhal numbers obtained with ΔT = 0.05 are consistently lower than those with ΔT = 0.025, but the differences are usually small (maximum 2.0% for $Re > 100$ and 2.8% for $Re < 100$), suggesting that ΔT = 0.05 is adequate to resolve the flows under investigation. Notable experimental data and numerical results from other researchers are also included in Figure 2.11, for comparison.

It can be observed that the present results are in excellent agreement with the experimental data in the laminar shedding regime ($Re < 190$). A fit of the present results obtained with $\Delta T = 0.025$ to the *St-Re* relationship proposed independently by Fey *et al.* (1998), and Williamson & Brown (1998)

$$St = A - \frac{B}{\sqrt{Re}} \tag{2-55}$$

yields $A = 0.2656$, and $B = 1.0247$, which are in good agreement with $A = 0.2684$, $B = 1.0356$ from Fey *et al.* (1998) by fitting their experimental data for $Re = 47$-180, and $A = 0.2665$, $B = 1.018$ from Williamson & Brown (1998) by fitting the parallel shedding data from Williamson(1988,1992). All these favorable comparisons indicate that, at least in the laminar flow regime, the present implementation of the vortex method is capable of capturing the physics of interest. However, the present 2-D simulations are unable to capture the discontinuities in the transitional region and tend to overpredict Strouhal numbers for circular cylinders at high Reynolds numbers, which is, of course, dictated by the 2-D nature of the method.

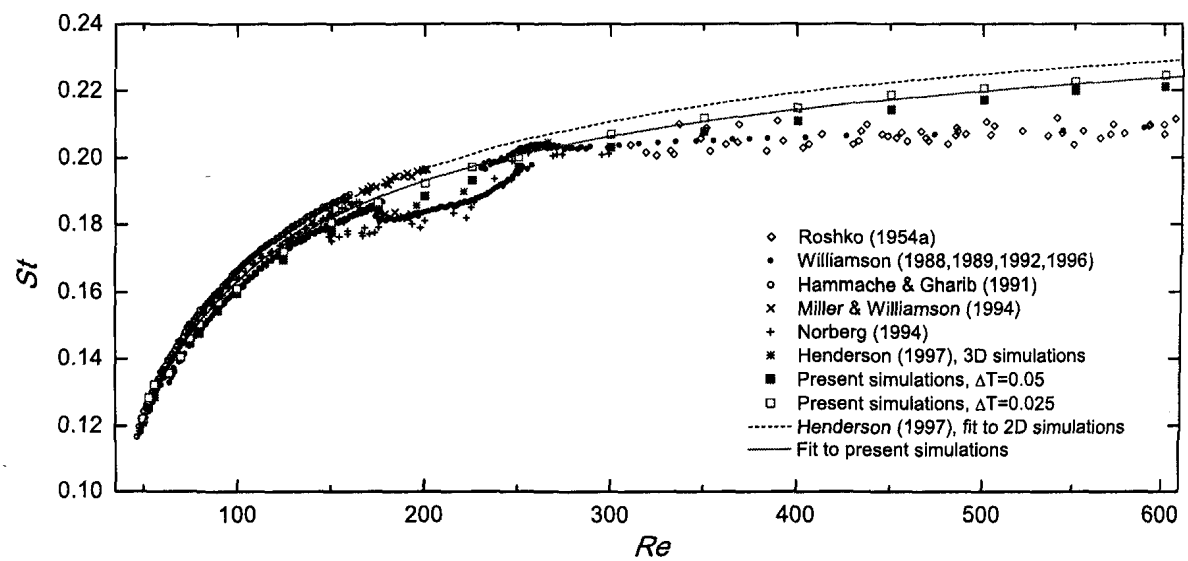

Figure 2.11. *St-Re* relationship for circular cylinders

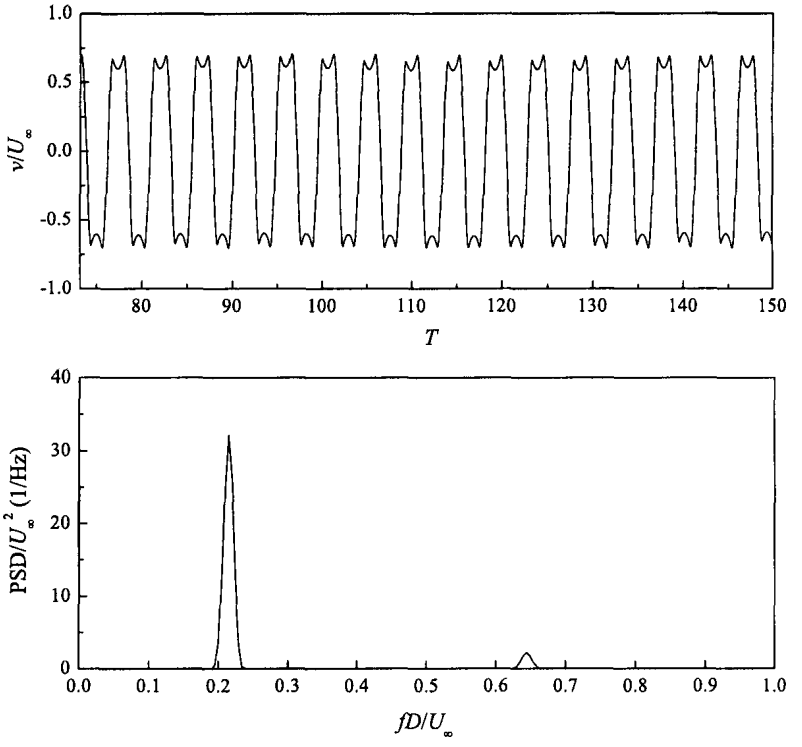

Figure 2.12. Cross-stream velocity time history (top) and its power spectral density (PSD, bottom) at the location on the center line of the wake and 2*D* downstream of a circular cylinder at $Re = 400$

Nevertheless, it is well known that the flows around circular cylinder are sensitive to Reynolds number variations, and the motion of separation points combined with the 3-D effects makes the flow at high Reynolds numbers intractable for 2-D methods. In Figure 2.13 the *St-Re* relationship for square cylinders is presented. Included for comparisons are notable experimental and numerical data available in the literature. Note the unpublished data referred to as Norberg (1996) are available from Sohankar *et al.* (1999). The available data for square cylinders are much more variable compared to circular cylinders except for $Re < 100$, where the present results are in close agreement with all the experimental and numerical data. The general trend is that Strouhal numbers for square cylinders are less sensitive to variations in Reynolds number for $Re > 150$, where the present results compare reasonably well with the experimental data by Shimizu & Tanida (1978), Okajima (1982), Norberg (1993), Norberg (1996), Saha *et al.* (2003),

and Dutta *et al.* (2008), and the numerical results by Fitzgerald *et al.* (2007). For Re > 400, the present results are also in agreement with those from 3-D DNS simulations by Sohankar *et al.* (1999). It is interesting to note that, for the flows around square cylinders at low to moderate Reynolds numbers, the Strouhal numbers predicted by 3-D simulations are not necessarily more "accurate" than the present results.

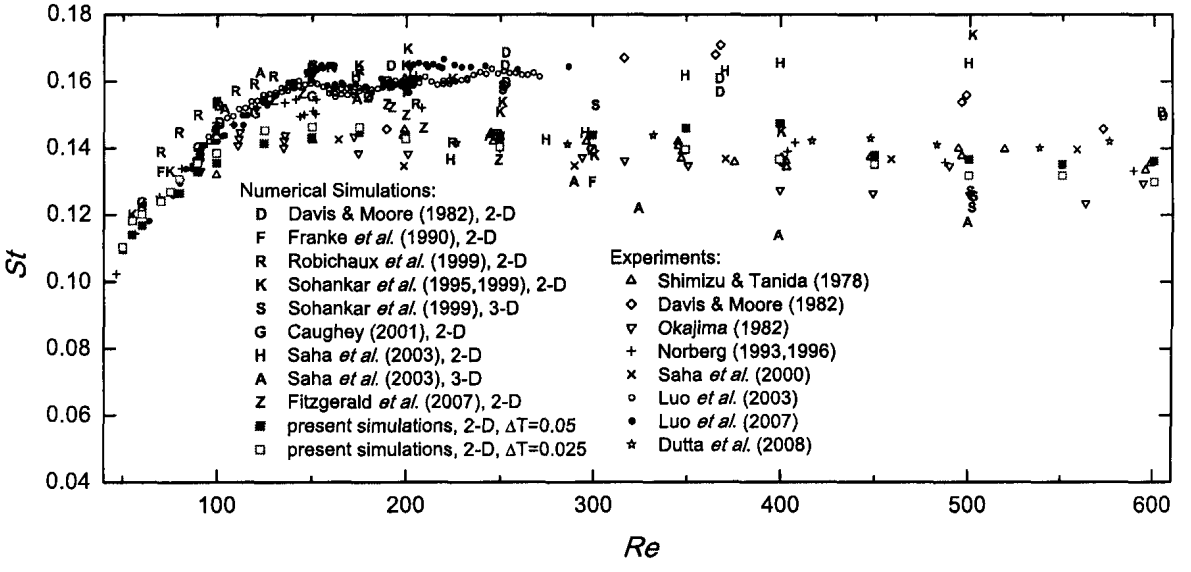

Figure 2.13. *St-Re* relationship for square cylinders

The Strouhal numbers recently obtained by Luo *et al.* (2003) and Luo *et al.* (2007) from experiments are significantly higher than those from Shimizu & Tanida (1978), Okajima (1982), Saha *et al.* (2000) and Dutta *et al.* (2008) for Re = 100-290, but no comparisons and discussions were made. The studies on aspect ratio and inclination of the end plates in Luo *et al.* (2007) seem to suggest that the use of longer cylinders and inclined endplates, which are intended for promoting and maintaining parallel shedding, tends to increase Strouhal numbers. It is interesting that, both larger aspect ratio and parallel shedding are ways of promoting two-dimensionality, and yet the result is that the experimental data deviates further from the present 2-D numerical results.

It can be observed from Figure 2.13 that, the numerical resolution has an impact on the predicted Strouhal numbers at some Reynolds numbers (usually less than 5.0%, except when $Re = 400$ the difference is 7.8%). In addition to the more unstable nature of the flow, the "rounding" of the sharp corners with a radius of $r = \lambda$ in the present simulations may also contribute to the impact. The panel length λ, and hence the corner radius ratio r/H (with H being the height of the square) decreases with increasing resolution. Studies on the corner sharpness (see Hu *et al.* 2006 and references cited therein) suggest that, the Strouhal number for a "square" cylinder increases almost linearly as r/H is increased from 0 (square with sharp corners) to 0.5 (circular cylinder). In the present simulations, the values of r/H varies from 0.045 ($Re = 50$) to 0.013 ($Re = 600$) when $\Delta T = 0.05$, and from 0.032 to 0.009 when $\Delta T = 0.025$. Since the difference in Strouhal numbers between circular and square cylinders are smaller at lower Reynolds number where r/H is larger, the effects of corner rounding are considered negligible in the present simulations. Nevertheless, square cylinders with slightly rounded corners may better mimic those used in real-life experiments.

Further comparisons for the simulation at $Re = 500$ for a square cylinder are presented in Table 2.2, in which C_{Lrms} is the r.m.s. (the root-mean-square) value of the lift coefficient. Experimental data for C_{Lrms} at $Re = 500$ is rare in the literature, and all the numerical results in Table 2.2, both 2-D and 3-D, are higher than the values from the water tunnel experiments by Shimizu & Tanida (1978). The experimental data presented in Shimizu & Tanida (1978) shows that, C_{Lrms} is sensitive to Re variations in the range $Re = 400$-$1{,}000$ (where $C_{Lrms} = 0.17$-1.27), hence, any errors in the experiments and numerical simulations leading to small changes in the effective Reynolds number may

result in significant discrepancies. Nonetheless, the present C_{Lrms} values compare reasonably well with other numerical results, and the drag coefficients and Strouhal numbers obtained from the present simulations are in good agreement with both experimental and numerical data available in the literature. These comparisons again confirm that the present 2-D code is capable of capturing the physics of interest at moderate Reynolds numbers for square cylinders.

Table 2.2. Comparison of force coefficients and Strouhal numbers for a square cylinder at $Re = 500$

Source	C_D	C_{Lrms}	St
Shimizu & Tanida (1978), water tunnel experiments	1.85 - 1.94	0.56 - 0.72	0.138 - 0.140
Okajima (1982), wind tunnel experiments	-	-	0.126 - 0.135
Norberg (1993), wind tunnel experiments	-	-	0.135
Okajima (1995), wind tunnel experiments	1.80 - 1.89	-	0.138
Hwang & Sue (1997), 2-D simulation	1.88	1.01	0.137
Sohankar *et al.* (1999), 3-D simulation	1.84	1.22	0.122
Sohankar *et al.* (1999), 2-D simulation	1.89	1.13	0.174
Saha *et al.* (2003), 3-D simulation	2.17	1.45	0.116
Present simulation, $\Delta T = 0.025$	2.08	1.35	0.132
Present simulation, $\Delta T = 0.05$	2.22	1.39	0.137

2.4.3. Stepwise variation of chord-based Strouhal numbers for rectangular plates at Re = 600

In these simulations, rectangular cylinders with elongation (c/t) ratios from 3 to 10 were placed in a uniform flow with freestream velocity U_∞, and, to balance accuracy and computational costs (i.e., time), the normalized time step was set to $\Delta T = 0.05$. A unity overlap ratio, β, was used throughout the simulations, and the particle spacing was chosen as $h/t = 1.291\times10^{-2}$ so that $\nu\Delta t/h^2 = 0.5$. The sharp corners were again "rounded"

as in the square cylinder case. Remeshing was carried out every 5 time steps, and the solid boundaries were discretized into panels of lengths $\lambda \approx h$. The fluid was impulsively set into motion with velocity U_∞ at the beginning of the simulation, and the simulations were performed long enough to yield 15-20 stable shedding cycles, with 3-5 million particles in the flow fields towards the end of the simulations.

The stepwise variation of the chord-based Strouhal number $St_c = f_v c/U_\infty$, where f_v is the shedding frequency, with c/t obtained from the simulations are shown in Figure 2.14, with comparisons to experimental and numerical results available in the literature. A second symbol for the same set of data indicates that a secondary shedding frequency was observed for certain c/t ratios, usually just before the "jump". Stepwise variations of St_c with c/t, as well as similar characteristics of the flows have been reported for rectangular plates over a wide range of Reynolds numbers in the literature, and, hence, it is reasonable to make comparisons between the results obtained at various Reynolds. Further discussions about the choice of the Reynolds number, Re = 600, are given in Section 3.2.

It can be observed from Figure 2.14 that the current results compare very well to the LES simulations by Ohya *et al.* (1992), and spectral element method simulations by Tan *et al.* (1998). For c/t = 3-5, the present results match the experimental results almost exactly. For larger c/t, small discrepancies can be observed, and they tend to be a little larger for c/t = 9-10. A possible explanation of these disparities is that the speed-up of the flow around the plates due to blockage in experiments may result in a higher convection speed of leading-edge vortices and hence a higher shedding frequency. In their 2-D spectral element method simulations, Tan *et al.* (2004) also find that $St_c = 0.55n$ instead

of $0.6n$ (n = 1,2,3...) commonly observed in experiments. They speculate that higher Reynolds numbers, and, hence, three-dimensional effects in experiments may lead to higher average convection velocity of leading-edge vortices, which in turn result in higher Strouhal numbers. Additional simulations of higher resolution with $\Delta T = 0.025$ and $v\Delta t/h^2 = 0.5$ were performed for c/t = 5, 6, 7 and 9 to check the dependence of the results on numerical resolution, and virtually no changes (i.e., differences less than 2.5%) in Strouhal numbers were observed, which suggests that the chosen resolution ($\Delta T = 0.05$) is adequate to resolve the flows under investigation.

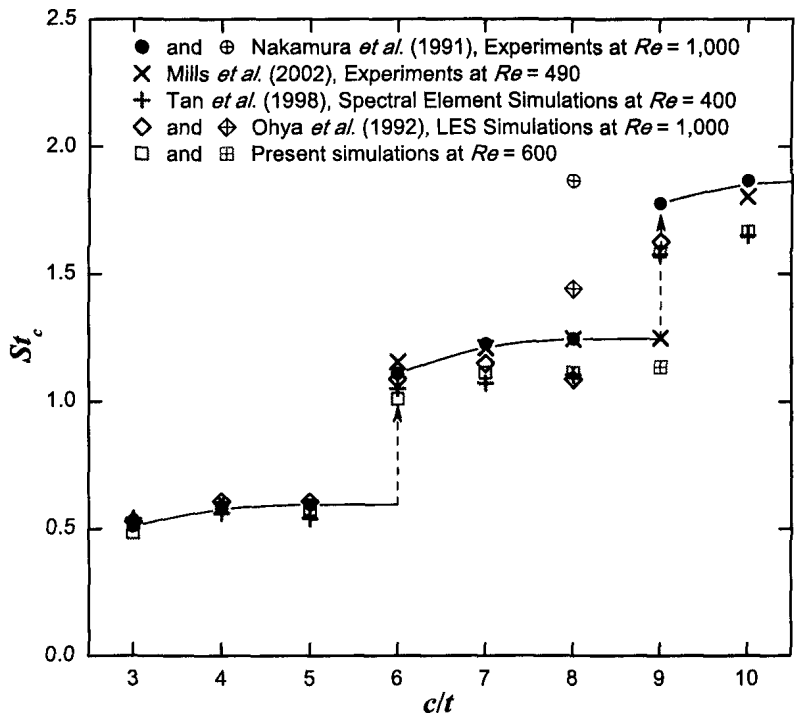

Figure 2.14. Stepwise variation of chord-based Strouhal numbers for rectangular plates at Re = 600

As mentioned in Chapter 1, the underlying mechanics leading to the stepwise variation has attracted strong interests from many researchers in the past two decades, and a detailed description of the shedding process and feedback mechanism is reviewed in Section 1.4.

Figure 2.15 shows a sequence of snapshots of the vorticity field for a rectangular plate with $c/t = 7$ at $Re = 600$ from the present simulations at time intervals of $\Delta T = 1$. In frame (a), there are two leading-edge vortices on the lower surface, and a trailing-edge vortex is growing. At the upper trailing-edge a leading-edge vortex is coalescing with the trailing-edge one, and another leading-edge vortex attached to the shear layer is still growing. In frame (b), the merging vortices at the upper trailing-edge are leaving the body, and the leading-edge vortex upstream is cut from the shear layer and starts to convect toward the trailing-edge. On the lower surface, a leading-edge vortex convects closer to the trailing edge and the trailing-edge vortex is still growing. In the next frame, the lower trailing-edge vortex is about to be shed while a leading-edge vortex is approaching. At the upper trailing edge, the merging vortices are shed as a pair into the wake, and a trailing-edge vortex starts to grow. A vortex also starts to grow at the end of the shear layer from the upper leading edge. Frame (d) shows the same coalescing process at the lower trailing edge as in frame (a) at the upper trailing edge, and the upper trailing-edge vortex is growing larger. This completes approximately half a shedding cycle.

It can be observed in Figure 2.15 that there are always two leading-edge vortices on both the upper and lower surfaces of the plate, which corresponds to the observation that $c/t = 7$ is of "mode 2" in Figure 2.14. It is also observed that trailing-edge vortices only form in-between the passages of leading-edge vortices, and the shedding of the coalescing vortices at the trailing edge corresponds to the end of the growth of a leading-edge vortex, which closely matches the experimental findings.

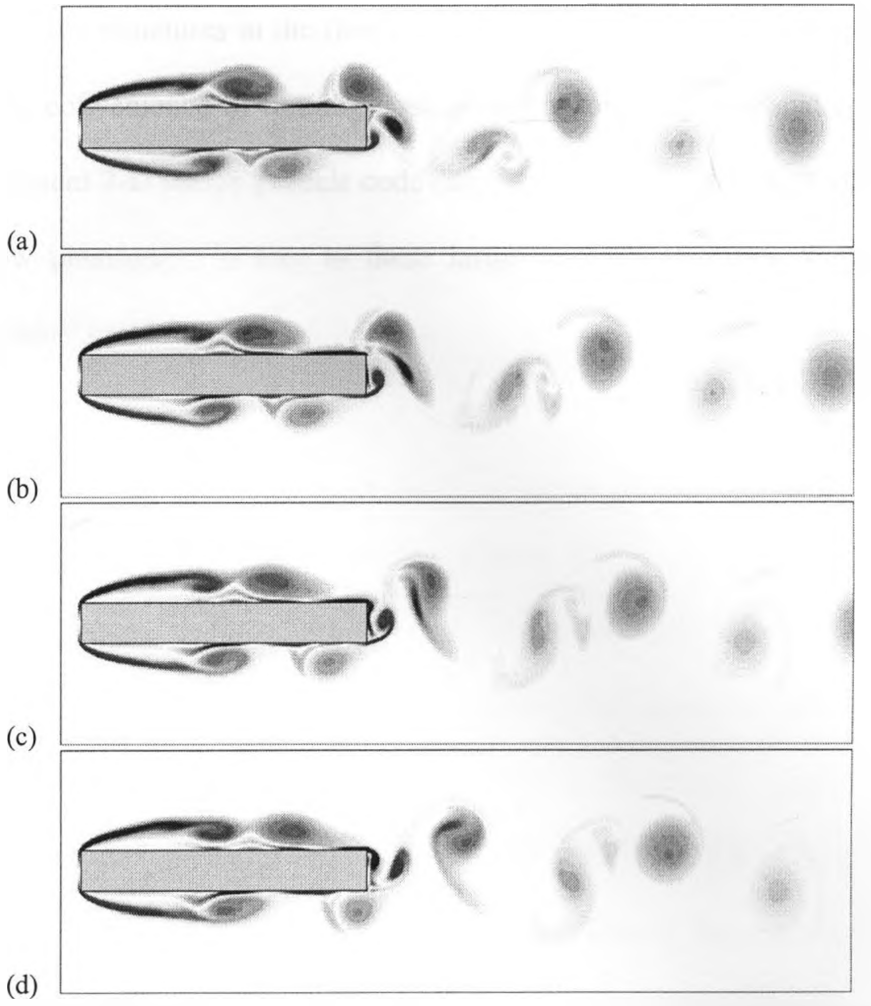

Figure 2.15. Vorticity field for a rectangular plate with c/t = 7 at Re = 600; The time interval between successive images in ΔT = 1.

The successful replication of the stepwise variation of the chord-based Strouhal numbers for rectangular cylinders, and the favorable comparisons of flow patterns from the present simulations with experimental observations, suggest that the present code is capable of capturing the physics of interest with reasonable accuracy. The fact that the flow patterns from the present 2-D simulations at a moderate Reynolds number agree well with experimental observations at much higher Reynolds numbers indicates that, although small differences in the flow fields are expected due to the large difference in Reynolds numbers and the absence of 3-D effects in these simulations, the energy-

carrying, large-scale structures in the flows are correctly captured to a significant extent. Hence, with the convenience of running simulations on ordinary personal computers at low cost, the present 2-D vortex particle code can be a useful engineering tool for studies of various flow phenomena related to these large vortical structures, such as vortex shedding from bluff bodies.

CHAPTER 3

EFFECTS OF GEOMETRY ON VORTEX SHEDDING FROM ELONGATED BLUFF BODIES

3.1. INTRODUCTION

As mentioned in Chapter 1, while previous studies on the flow around rectangular cylinders have provided valuable insights into vortex shedding from elongated bluff bodies, there is a lack of detailed knowledge regarding the effects of geometric details (e.g., nosing shapes, and asymmetry of upper and lower surfaces, etc.). Application of the main findings from these studies, such as the classification of flow regimes based on elongation ratios (c/t), and the stepwise variation of chord-based Strouhal numbers ($St_c = f_v c/U_\infty$), to flows around bridge sections is still limited. In this chapter, numerical simulations of flows around flat plates with various nosings at Re = 600 are performed with the 2-D high-resolution vortex particle method implemented in Chapter 2. The resultant flow fields are then explored. Thus, the main objective of this chapter is to identify the geometric effects on vortex shedding from elongated bluff bodies, so that explanations of the effects of nosing shapes and elongation ratios may be offered in a systematic way. It should be noted that, all the simulations are carried out with a 2-D code at a relatively low Reynolds number, since it is the basic mechanisms and geometric effects which are of interest here. The approach here is much like the low Reynolds number work on the flow around circular cylinders.

3.2. NUMERICAL SIMULATIONS

3.2.1. Simulation Details

In this series of simulations, flat plates with various nosings and elongation ratios (c/t ranging from 3 to 10) were placed in a uniform flow with free stream velocity, U_∞. A definition sketch of a flat plate with triangular nosings is shown in Figure 3.1. The angle, θ, was chosen to be 60°, 75°, 82.5°, 90°, 105°, 120° and 150° in the simulations, and a rectangular plate may be fit into this series with $\theta = 180^\circ$. Flows around flat plates with a streamlined leading edge (half Rankine Oval with a width to height ratio of 2, see Figure 3.2) and a rectangular trailing edge were also simulated for comparison. The streamlined leading edge was used to eliminate the leading-edge separations as a limiting case. A list of the simulations presented in this chapter is given in Table 3.1. For convenience, the plates with various leading and trailing edges are given a short name. For example, a "T90-R plate" refers to a plate with a $\theta = 90^\circ$ triangular leading edge and a rectangular trailing edge, and an "O-R plate" is one that has a streamlined leading edge (Rankine Oval) and a rectangular trailing edge.

The Reynolds number based on freestream velocity and the thickness of the plates was 600. To balance accuracy and computational costs, the normalized time step was set to $\Delta T = 0.05$ (see Sections 2.4.2 and 2.4.3 for discussions about the dependence of the results on numerical resolution). A unity overlap ratio, β, was used throughout the simulations, and the particle spacing was chosen to be $h/t = 1.291\times10^{-2}$ so that $\nu\Delta t/h^2 = 0.5$, where Δt is the time step. The solid boundaries were discretized into panels of lengths $\lambda \approx h$, and the sharp corners were "rounded" with radius $r = \lambda$ for better numerical

behavior, as discussed in Chapter 2. The fluid was impulsively set into motion with velocity U_∞ at the beginning of the simulation, and remeshing was applied every 5 time steps. All the computations were carried out on a desktop computer, and the simulations were performed long enough for the start-up effects to die out. In most cases 15-25 stable shedding cycles were observed, with 3-5 million particles in the flow fields toward the end of the simulations.

Table 3.1. Simulations of flows around elongated bluff bodies at $Re = 600$

Leading edge	Trailing edge	Short name	c/t	$\Delta(c/t)$
triangular, $\theta = 60^\circ$	triangular, $\theta = 60°$	T60-T60	3-10	1
triangular, $\theta = 75^\circ$	triangular, $\theta = 75°$	T75-T75	3-10	1
triangular, $\theta = 82.5^\circ$	triangular, $\theta = 82.5°$	T82.5-T82.5	3-10	1
triangular, $\theta = 90^\circ$	triangular, $\theta = 90^\circ$	T90-T90	3-10	0.25
triangular, $\theta = 105^\circ$	triangular, $\theta = 105^\circ$	T105-T105	3-10	1
triangular, $\theta = 120^\circ$	triangular, $\theta = 120^\circ$	T120-T120	3-10	1
triangular, $\theta = 150^\circ$	triangular, $\theta = 150^\circ$	T150-T150	3-10	1
triangular, $\theta = 75^\circ$	rectangular	T75-R	3-10	1
triangular, $\theta = 90^\circ$	rectangular	T90-R	3-10	0.25
triangular, $\theta = 105^\circ$	rectangular	T105-R	3-10	1
triangular, $\theta = 120^\circ$	rectangular	T120-R	3-10	1
triangular, $\theta = 150^\circ$	rectangular	T150-R	3-10	1
rectangular	rectangular	R-R	3-10	0.5
Rankine oval	rectangular	O-R	3-10	1

3.2.2. Reynolds Number Effects

The Reynolds number, $Re = 600$, was chosen as a compromise between physical requirements and computational costs. At low Reynolds numbers, 3-D effects are less pronounced and 2-D simulations would have greater accuracy. A lower Reynolds number

is also desirable to reduce computational costs. However, the wind tunnel experiments at Re = 200-1,000 by Nakamura *et al.* (1996) have shown that the stepwise variation of St_c for rectangular plates only occurs above Re = 300. When Re < 250, the separated shear layers appear to be steady and the trailing edge shedding dominates the wake, which leads to an almost linear variation of St_c with c/t (or, in other words, an almost constant thickness-based Strouhal number, St). This is consistent with the experimental results of Lane and Loehrke (1980), who found that the separation bubble on a long blunt plate is steady up to Re = 260. It is also shown by Lane & Loehrke that the length of separation bubble increases with Reynolds number up to Re = 325, and then shrinks with further increases in Reynolds number and asymptotes to 4-5 plate thicknesses after Re = 700. Through 2-D simulations of separated-reattaching flows over a normal plate followed by a long splitter plate, Najjar & Vanka (1993) also find that "a clear shedding" of vortices from the separation bubble only occurs above Re > 250. On the other hand, flow visualizations by Sasaki & Kiya (1991) suggest that the leading-edge separation bubble on a blunt flat plate becomes three-dimensional at Re > 320. Strouhal numbers obtained at relatively low Reynolds numbers, both experimentally (e.g., water tunnel experiments at Re = 490 by Mills *et al.* 2003) and numerically (e.g., 2-D spectral element method simulations at Re = 400 by Tan *et al.* 1998, 2004), are in good agreement with the experimental data Re = 1,000 by Nakamura *et al.* (1991). Nakamura *et al.* (1996) also report that an increase in Reynolds number from 300 to 1,000 only leads to higher levels of "random modulations" in velocity signals in the wake of rectangular plates, and the shedding frequencies remain unchanged. Furthermore, it is demonstrated in Tafti & Vanka (1991) that, time-dependent features of flows around rectangular plates, such as

leading-edge shedding frequencies and vortex convection speeds, predicted by their 2-D LES simulations at Re = 1,000 are in good agreement with experiments at much higher Reynolds numbers.

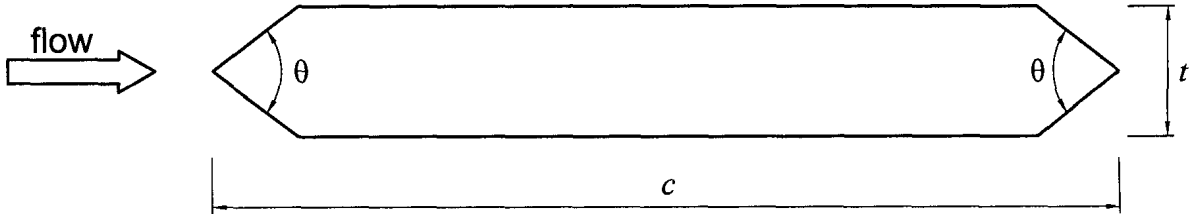

Figure 3.1. Sketch of a flat plate with triangular leading and trailing edges

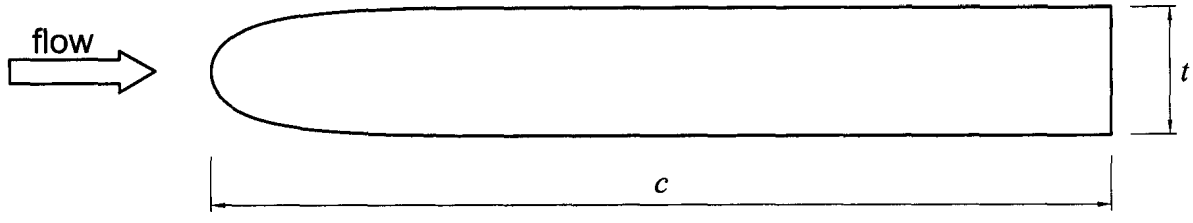

Figure 3.2. Sketch of a flat plate with a streamlined leading edge and a rectangular trailing edge

Table 3.2. Experiments and numerical simulations where stepwise variation of St_c is observed

Source	*Re*	Method	Blockage ratio
Nakamura *et al.* (1996)	300-1,000	Wind tunnel experiments	0.1%
Tan *et al.* (1998, 2004)	400	Numerical simulations (2-D)	2.5%
Mills *et al.* (2003)	490	Water tunnel experiments	4.8%
Nakamura *et al.* (1991)	1,000-3,000	Wind tunnel experiments	0.2%
Mills *et al.* (2002)	5,000-13,000	Wind tunnel exp. with external forcing	open jet
Stokes & Welsh (1986)	8,000-44,300	Wind tunnel exp. with resonant sound	2.5-4.9%
Parker & Welsh (1983)	14,800-31,100	Wind tunnel exp. with external forcing	open jet
Nakamura & Nakashima (1986)	2,400-288,000	Wind tunnel experiments	0.6-6%

Actually, as long as the Reynolds number is high enough for the leading-edge shedding to occur, similar characteristics of flows around long rectangular plates have been reported over three decades of variation in Reynolds number; see Table 3.2 for a

summary of the experiments and numerical simulations where such observations are reported (although the observations for long plates at high Reynolds numbers included in the table were all made under external forcing). In other words, the flows around sharp edged rectangular plates are largely insensitive to the variation of Reynolds numbers when $Re > 300$, hence, a comparison between the results obtained at various Reynolds numbers are reasonable. This also justifies the use of 2-D simulations at a moderate Reynolds number in the present work to study this phenomenon.

3.3. STEPWISE VARIATION OF CHORD-BASED STROUHAL NUMBERS

Figure 3.3 shows the variations of chord-based Strouhal numbers (St_c) for a series of flat plates with triangular nosings. The dashed straight line is a reference line with a slope of 0.2. As well, a symbol with a "+" at its center indicates that a secondary peak was observed in spectral analysis. Also shown for comparison is the St_c variation for flat plates with a streamlined leading edge and a rectangular trailing edge. For convenience in discussions, a "mode" number (Hourigan *et al.* 2001, Mills *et al.* 2002, 2003) is assigned to each part between jumps in the St_c map. Figure 3.3 shows that there are two limits for St_c variations: horizontal lines with jumps at certain elongation ratios (lower limit, rectangular plates), and a straight line (upper limit, plates with streamlined leading edge) where St_c varies almost linearly with c/t. It can be inferred from the discussion in Chapter 1 about the mechanism leading to the stepwise variation of St_c for rectangular plates that, when leading-edge vortices are strong enough to interfere with the trailing-edge shedding, St_c tends to follow the horizontal line as in the case of rectangular plates.

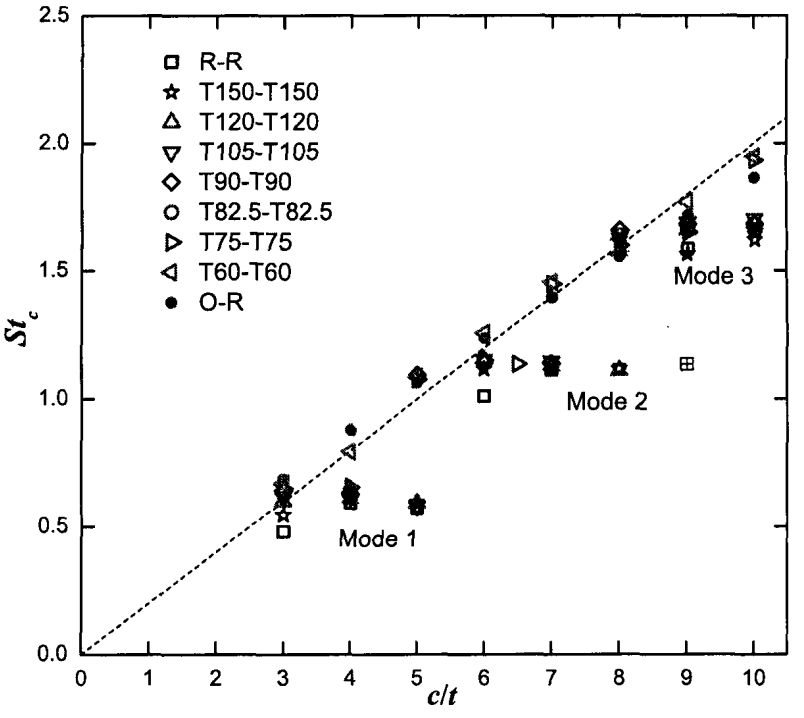

Figure 3.3. St_c for flat plates with triangular leading and trailing edges at $Re = 600$

For plates with a streamlined leading edge, the trailing edge shedding dominates the wake and, hence, an almost linear variation of St_c (or an almost constant shedding frequency, f_v) is observed. As mentioned in Chapter 1, a longer development distance leads to a thicker boundary layer before separation at the trailing edge, which in turn results in a wider near wake and a lower Strouhal number, and, hence, a slight deviation of St_c from the straight line can be observed. By reducing the separation angle at the leading edge (which is half of θ), the transition from the lower to upper limit appears to be continuous: St_c jumps occur earlier, the sizes of which tend to be smaller, until finally they disappear and St_c variation follows the straight line (e.g., St_c variation for T60-T60 plates in Figure 3.3).

A triangular nose extending into the wake may interfere with vortex formation in the near wake, and, hence, it may have an impact on the Strouhal number. Figure 3.4

presents the variations of St_c with c/t for flat plates with triangular leading edges and rectangular trailing edges. Fewer plates are included in this figure to avoid cluttering of data. In comparison with Figure 3.3, only minimal changes can be observed (e.g. the secondary Strouhal number for a T120-T120 plate disappears for a T120-R plate at c/t = 8). This indicates that the shape of trailing-edge nosing has only a minor influence on the shedding frequency.

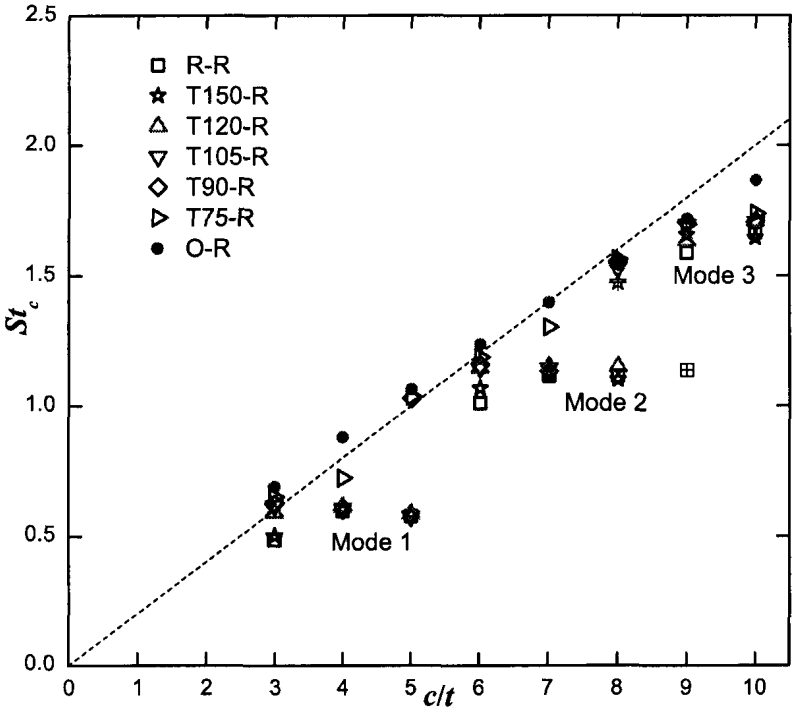

Figure 3.4. St_c for flat plates with a triangular leading edge and a rectangular trailing edge at Re = 600

In Figure 3.5 a comparison of the St_c variations for a T90-T90 plate and a T90-R plate is presented with smaller increments of c/t. It can be observed that the triangular trailing edge may delay the St_c jumps to slightly larger elongation ratios, and lead to slightly larger sizes of jumps. Since the chord length is measured from tip to tip (see Figure 3.1), the distance between the leading- and trailing-edge separation points (referred to as "surface length" hereafter) differs slightly (by 0.5t in this case) for these

two plates, which may also contribute to the discrepancies in St_c at some elongation ratios. However, normalizing the shedding frequencies with surface lengths does not bring the Strouhal numbers for both plates closer to each other, which indicates that the interference of the trailing-edge nose with vortex formation in the near wake does play a role in leading to these discrepancies.

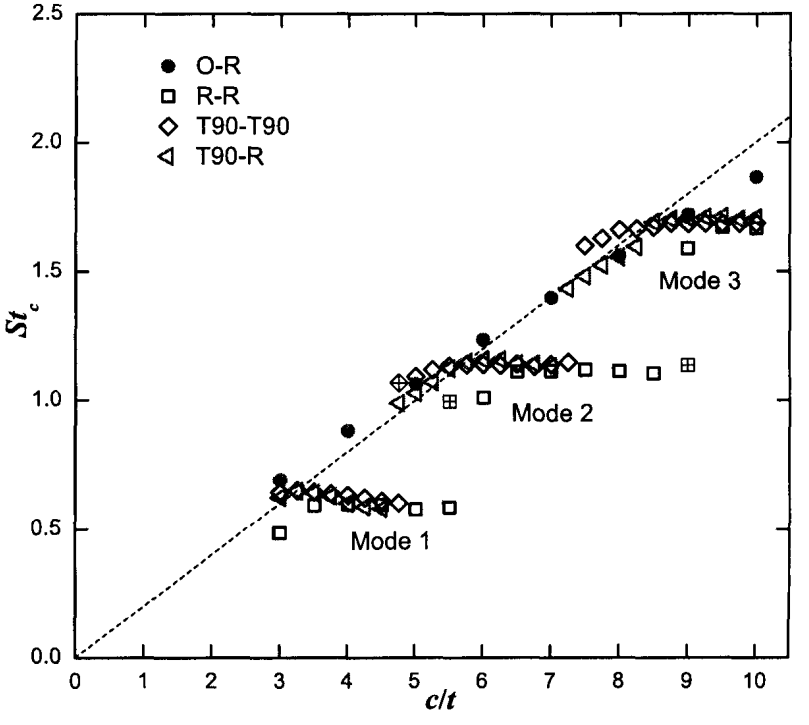

Figure 3.5. St_c for flat plates with $\theta = 90^{\circ}$ triangular leading edges at $Re = 600$

More importantly, with finer increments of c/t, Figure 3.5 shows a clearer picture of the transition before and after a jump in St_c. It can be observed that St_c does not always jump directly onto the "horizontal leg" of a higher mode. Instead it settles at a somewhat lower value, and then follows a straight line (referred to as the "linear leg" of a mode, hereafter) which eventually makes transition to the horizontal leg. This means that the shedding frequency (f_v) remains nearly constant after the jump over a range of elongation ratio, and then starts to decrease with c/t. Since the linear leg is associated with shedding

from the trailing edge, while the horizontal leg is largely controlled by shedding from the leading edge, this suggests that one of the significant effects of nosing geometry is that, depending on c/t ratios, both mechanisms can occur for any particular leading-edge separation angle. This will be further examined below.

3.4. MEAN FLOW CHARACTERISTICS

3.4.1. Reattachment Lengths

As mentioned in Chapter 1, the reattachment length (x_r) is often used as the characteristic length scale to normalize other dimensions in separated and reattaching flows. Figure 3.6 shows variation of the reattachment length with c/t for T90-R, T105-R, T120-R and R-R plates, in which x_r is measured from the separation point to the location where the mean wall shear stress (which was calculated on a grid of $0.05t$ increments) changes sign (following a reverse flow region). The experimental results from Blazewicz *et al.* (2007) and Yaghoubi & Mahmoodi (2004) for R-R plates are also included for comparison. Note that an open-jet wind tunnel was used by Blazewicz *et al.* (2007), while the blockage ratio in Yaghoubi & Mahmoodi (2004) is 4.4%. Hence, the x_r values from the former are higher than those from the latter. Figure 3.6 shows that, for the c/t under investigation, x_r tends to increase with c/t, and is longer for bluffer plates. The dependence of x_r on c/t is consistent with the two sets of experimental data, although the values differ significantly for longer plates. However, the largest value of x_r from the present simulations for a rectangular plate, $x_r = 7.5t$, occurs at $c/t = 10$, is in good agreement with $x_r = 7.7t$ reported by Castro & Epik (1998), who argue that two dimensionality (large aspect ratio, which is

64 in their experiment, 2-D in the present simulations) and low blockage ratio (1.2% in their experiment, 0 in the present simulations) lead to longer reattachment lengths (see Section 1.2 for a discussion). For short plates (e.g. $c/t = 4$), x_r is almost the same for all plates in Figure 3.6, which is also in good agreement with the experimental result from Yaghoubi & Mahmoodi (2004). This indicates that, for short plates, x_r is largely limited by the presence of the trailing edge, and is less sensitive to other effects, such as the effects of leading-edge separation angle and blockage ratio. For rectangular plates with $c/t = 5.5$ and 7, the present results compare fairly well with those obtained experimentally by Blazewicz *et al.* (2007), which suggests that the physics are correctly captured in present simulations. A possible reason for the discrepancies at larger elongation ratios is that, 3-D effects, which may be more pronounced on longer plates, are missing in the present 2-D simulations.

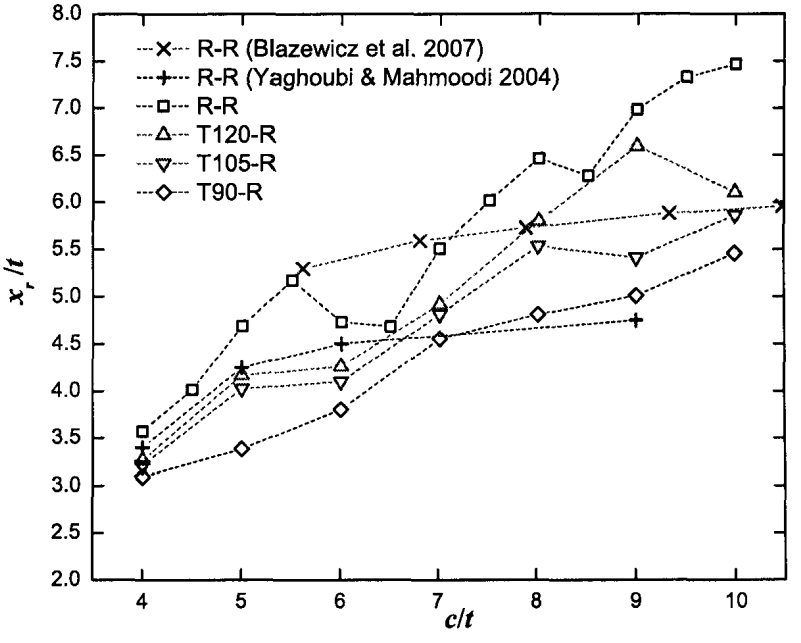

Figure 3.6. Reattachment lengths for flat plates at $Re = 600$

The scaling of x_r with separation angles proposed by Djilali & Gartshore (1992, referred to as DG92 hereafter), which is given by Equation (1-1), does not seem to apply to the present data presented in Figure 3.6 (for example, Equation (1-1) predicts that x_r for a T90-R plate is half that for an R-R plate, which is not the case for the present data). Interestingly, recent wind tunnel data ($x_r = 4.2t$ for a rectangular plate, and $2.1t$ for a T90-T90 plate, both with $c/t = 7$) reported by Taylor *et al.* (2009, TGK09 hereafter) scale well with Equation (1-1). A closer look into the experimental details by DG92 and TGK09 reveals that Reynolds number (5×10^4 in DG92, 3×10^4 in TGK09), aspect ratio (11.1 in DG92, 18 in TGK09), and blockage ratio (5.6% in DG92, 5.4% in TGK09) are similar in both experiments. In Figure 3.6, due to the 2-D nature of the simulations, and a zero blockage ratio, x_r is still increasing with c/t even for the longest plates. Or, in other words, the reattachment lengths are limited by the presence of the trailing edge of the plates and are not "saturated". While in the experiments at high Re with low aspect ratios and high blockage ratios, x_r may be already "saturated" (at a value observed in many experiments on semi-infinite plates) even on a plate with $c/t = 7$. So, it is reasonable to assume that the empirical relationship given in Equation (1-1) may only be applied to "saturated" x_r data.

The variations of x_r with c/t for T90-R and T90-T90 plates are compared in Figure 3.7. Within the c/t range under investigation, x_r increases with c/t for both plates. Overall the reattachment lengths at the same c/t ratios for both plates are close to each other, and the effects of the trailing-edge shape are mostly observed on short plates and those near the St_c jumps (see Figure 3.5). For short plates, the surface length is $t/2$ longer on a T90-R plate and, hence, a longer x_r is observed. However, the difference near the St_c jump at c/t = 7.25-7.5 is interesting, since the close match of x_r for both plates before and after this

c/t region seems to suggest that the small difference in surface lengths is not the reason for the relative large difference in x_r, and it is more likely that the shedding process leads to a different arrangement of the vortices on the body surfaces. That is, x_r measured on plates with finite lengths might be affected by vortex shedding in the wake, and, hence, caution should be used when comparing various experiments.

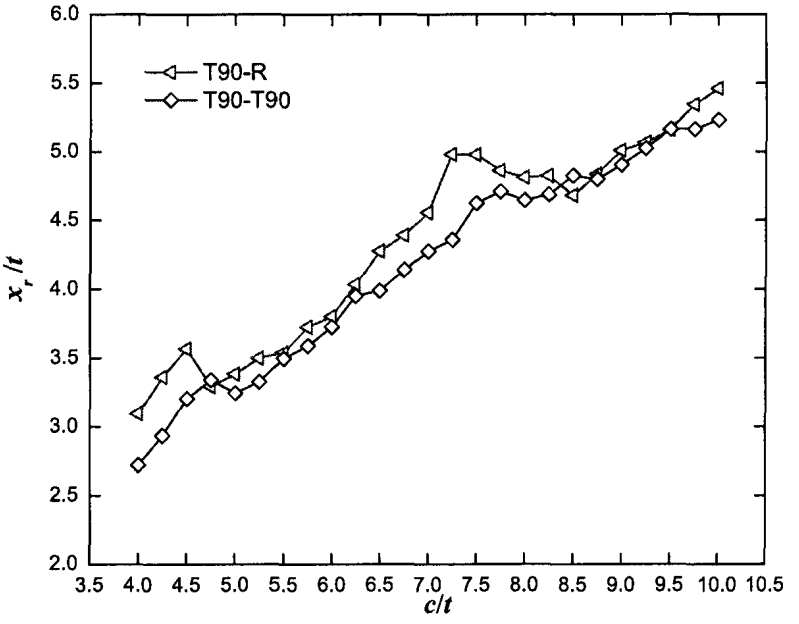

Figure 3.7. Reattachment lengths for flat plates with $\theta = 90^{\circ}$ triangular leading edges at $Re = 600$

3.4.2. Wake Formation Lengths

The (vortex) formation length (the length of the vortex formation region in the near wake) is considered by Gerrard (1966, see Appendix A for a description of Gerrard's formation region model) one of the two characteristic length scales (the other one is the "diffusion length") governing the shedding frequency of short bluff bodies. A relevant definition in the mean flow field is the length of the "wake recirculation region" or "wake formation region" (see, e.g., Williamson 1996), which is bounded by the mean zero streamline in

the near wake. In the present study, the length of the wake formation region is simply referred to as the "formation length" (L_w), and is determined from the trailing-edge separation point to the saddle point of the streamlines in the wake.

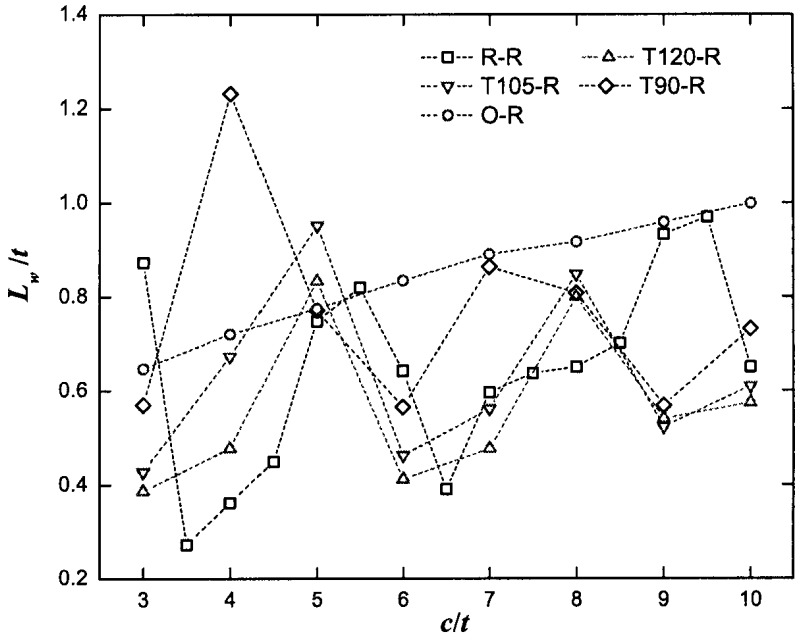

Figure 3.8. Formation lengths for flat plates at Re = 600

The variations of formation length with c/t for various flat plates with rectangular trailing edges are presented Figure 3.8. For the O-R plate, L_w increases almost linearly with c/t, which is consistent with the finding for short bluff bodies (the O-R plate has no afterbody) that the shedding frequency (see Figure 3.4, note St_c increases almost linearly with c/t, and the shedding frequency decreases slightly with c/t) roughly scales inversely with L_w (Roshko 1954b, Gerrard 1966). For T90-R, T105-R and T120-R plates, two peaks are observed in L_w at the two elongation ratios just before St_c jumps in Figure 3.4. For the R-R plate, two peaks are also observed near the St_c jumps, although a larger peak at c/t = 9.5 occurs after the St_c jump at c/t = 9.0. This is because the flow is intermittent

for $c/t = 9.0$ (which is indicated by the secondary Strouhal number), and an average value is obtained in the mean flow field.

Figure 3.9 compares the variations of L_w with c/t for T90-R and T90-T90 plates at much smaller c/t steps. Unlike the Strouhal numbers in Figure 3.5, L_w can be noticably different for these two similar plates. The L_w peaks in Figure 3.9 all coincide with St_c jumps, and, what is more interesting is that, the valleys of L_w variations also coincide with the transition points from linear to horizontal legs in the St_c map. That is, L_w decreases with c/t for plates on a linear leg (almost constant shedding frequencies), and increases with c/t for plates on a horizontal leg (decreasing shedding frequencies).

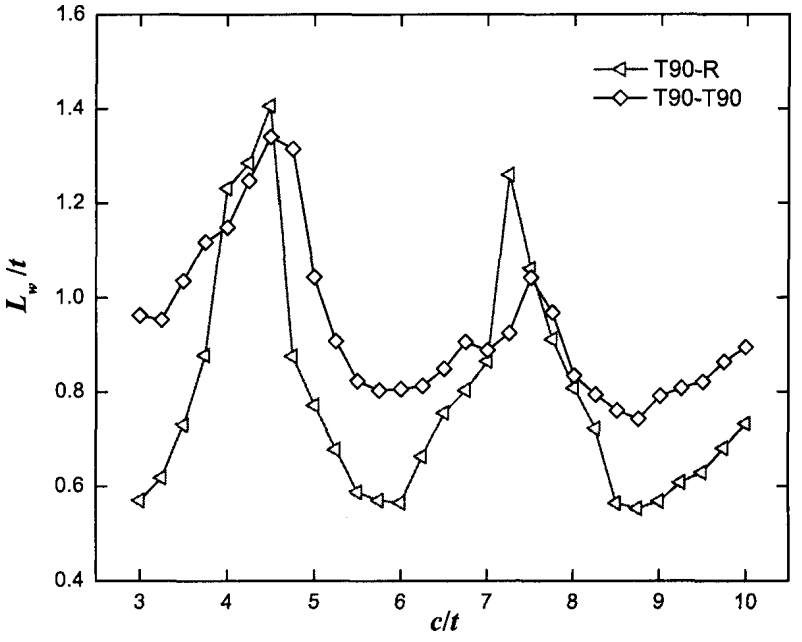

Figure 3.9. Formation lengths for flat plates with $\theta = 90^\circ$ triangular leading edges at $Re = 600$

Figure 3.9 also shows that, as expected from previous discussions, the triangular trailing-edge nose intruding into the near wake tends to push the end of formation region away from the body, resulting in a longer L_w. However, L_w peaks at St_c jumps are smaller in the presence of a triangular trailing-edge nose. On the other hand, the significant

discrepancies in L_w observed in Figure 3.9 only lead to minor differences in St_c in Figure 3.5, indicating that, in the presence of leading-edge shedding, the formation length in the wake is no longer the governing length scale of the shedding frequency. Since the trailing-edge nose has only a secondary influence on the Strouhal number (which is of main interest of the present study), only plates with a rectangular trailing edge will be included in the rest of the discussions, so that we can focus on the effects of leading-edge geometries and elongation ratios.

3.4.3. Velocity Fields

Mean velocity profiles at a series of locations (x/t = -4.0 to 1.0 by $\Delta x/t$ = 0.5) for O-R, T90-R and R-R plates with c/t = 7 are presented in Figure 3.10, where x is measured from the trailing-edge of the plate, and a distance of $\Delta x/t$ = 5 is scaled as one unit on the horizontal axis in the figure. c/t = 7 is chosen because both the T90-R and R-R plates are on the horizontal leg of the second mode, and both leading- and trailing-edge shedding are strong on these plates. In Figure 3.10(a) the velocity profiles above the surface of the O-R plate mimics that of a classical boundary layer, although slight speed-ups (1.113-1.135 in the figure for $x/t \leq 0$) are observed at the edge (where the mean velocity reaches its maximum) of the surface layer. The thickness of the surface layer (from its edge to the plate surface) is around 0.43-0.5t. In the near wake, an intense reverse flow region ($U_{\min}$ = -0.193U_∞ at x/t = 0.5) can be observed, where the velocity profile takes a similar shape to that in the wake of a circular cylinder. For the T90-R plate (Figure 3.10(b)), a reverse flow region (separation bubble) appears on the surface near the leading edge, and a higher level of speed-up (1.099-1.196 in the figure for $x/t \leq 0$, higher in the reverse flow

region) is observed. The thickness of the surface layer is thicker in the reverse flow region (0.65-0.68t for $x/t \leq$ -2.0) and thinner in the redevelopment region (0.58-0.66t for -1.5$\leq x/t \leq$ 0), which is still much thicker than that on an O-R plate. The reverse flow in the near wake is less intense, being $U_{\min}$ = -0.101U_∞ at x/t = 0.5, which is nearly half of that behind an O-R plate. For the rectangular plate in Figure 3.10(c), the separation bubble is noticeably larger than that on a T90-R plate, and the speed-up is also higher (1.055-1.257 in the figure for $x/t \leq$ 0, higher in the reverse flow region). As expected, the surface layer is also much thicker, which is 0.95-1.14t for $x/t \leq$ 0.0. The near wake reverse flow is even weaker with U_{min} = -0.055U_∞ at x/t = 0.5, again nearly half of that in the wake of a T90-R plate.

Figure 3.11 presents the streamwise (u_{rms}) and cross-stream (v_{rms}) r.m.s. (root-mean-square) velocity profiles for O-R, T90-R and R-R plates with c/t = 7 at the same series of locations as in Figure 3.10. In the figure x is measured from the trailing-edge of the plate, and a distance of $\Delta x/t$ = 5 is scaled as 0.4 units on the horizontal axis. A simple invicid model of a Rankine vortex (which is of size on the order of t, and strength on the order of $U_\infty t$) convecting near a wall shows that, the vortex induces maximum streamwise velocity fluctuations at its top and bottom edges (although the upstream velocity fluctuations near the wall is much higher than the streamwise fluctuations at its outer edge due to the presence of a wall), and maximum cross-stream velocity fluctuations near its upstream and downstream edges. Hence, convecting vortices on the surfaces of the plates will manifest themselves on the u_{rms} curve as two peaks (with the primary one lies closer to the wall), and as a single broad peak on the v_{rms} curve between the two peaks on the u_{rms} curve (see also Burgmann et al. 2008, and Yarusevych *et al.* 2009). Also, the

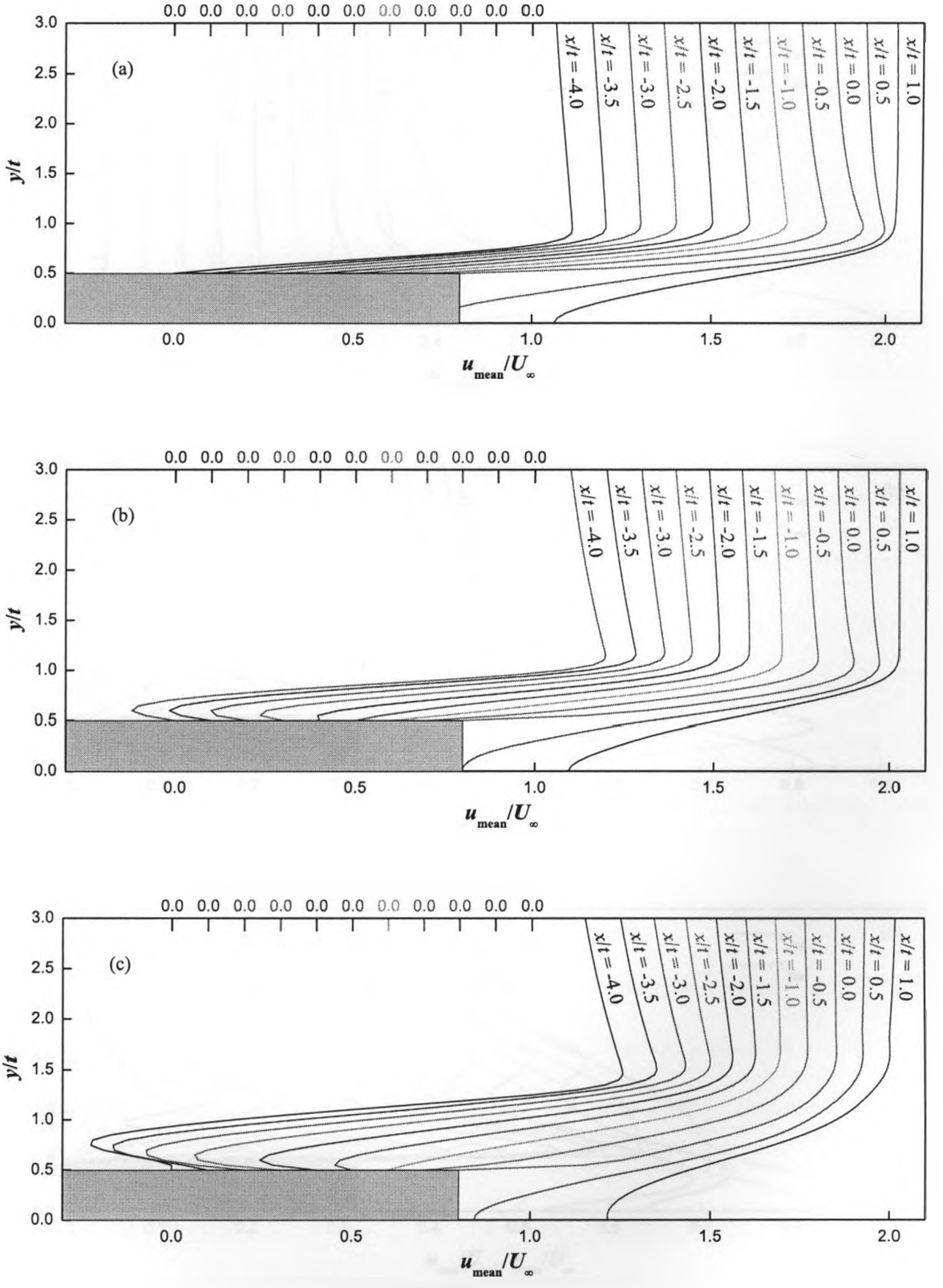

Figure 3.10. Mean velocity profiles at different locations for flat plates with c/t = 7; (a) O-R; (b) T90-R; (c) R-R. x is measured form the trailing edge, $\Delta x/t$ = 5 is scaled as one unit on the horizontal axis.

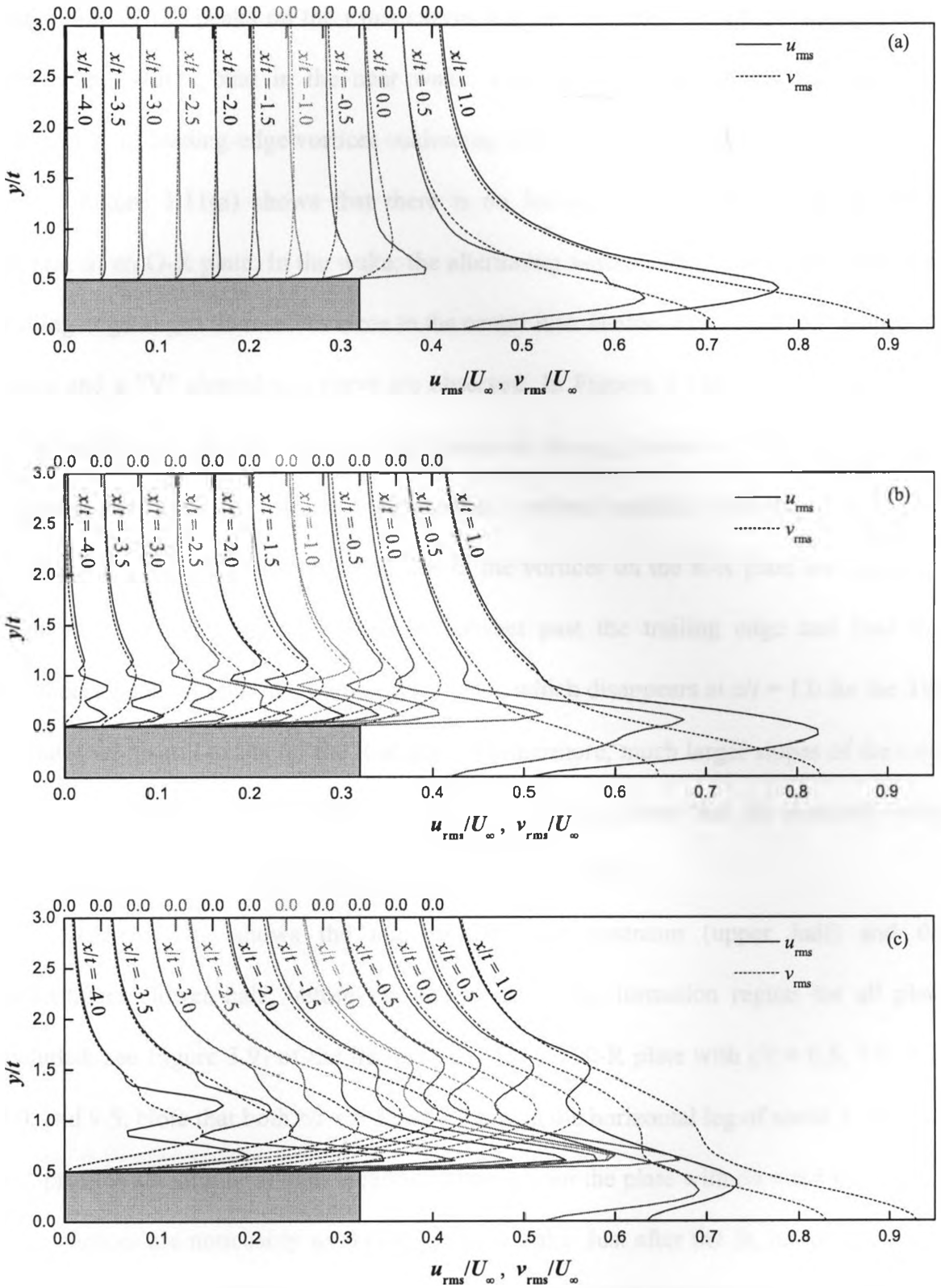

Figure 3.11. Streamwise and cross-stream r.m.s. velocity profiles at different locations for flat plates with $c/t = 7$; (a) O-R; (b) T90-R; (c) R-R. x is measured form the trailing edge, and $\Delta x/t = 5$ is scaled as 0.4 units on the horizontal axis

magnitude of the peaks on the r.m.s curves may be an indication of the strength of the convecting vortex, and in the near wake, a secondary peak on the u_{rms} curve is a "footprint" of leading-edge vortices coalescing with the trailing-edge one.

Figure 3.11(a) shows that there is no leading-edge vortex convecting on the surface of an O-R plate. In the wake, the alternating vortices shed from either side of the trailing edge aligns themselves close to the center line. Hence, a classical "M" shaped u_{rms} curve and a "V" shaped v_{rms} curve are observed. In Figures 3.11(b) and (c), the double peaks on the u_{rms} curves, and the broad peaks on the v_{rms} curves between the u_{rms} peaks indicate that there are strong leading-edge vortices regularly convecting along the surfaces of both plates, although the size of the vortices on the R-R plate are larger. For both plates, the leading-edge vortices convect past the trailing edge and lead to a secondary peak on both u_{rms} curves at $x/t = 0.5$, which disappears at $x/t = 1.0$ for the T90-R plates while still exists for the R-R plate. Furthermore, much larger slopes of the r.m.s. curves away from the plate surface in Figure 3.11(c) indicate that the unsteady vortex shedding from the plate is felt by a larger region of the flow.

Figure 3.12 shows the u_{rms} profiles just upstream (upper half) and $0.5t$ downstream (lower half; before the end of the wake formation region for all plates included, see Figure 3.9) of the trailing-edge for a T90-R plate with $c/t = 6.5$, 7.0, 7.25, 8.0, and 9.5. Note that both $c/t = 6.5$ and 7.0 are on the horizontal leg of mode 2, and their u_{rms} profiles are similar at both locations, although for the plate with $c/t = 6.5$ the leading-edge vortices are noticeably weaker in the near wake. Just after the St_c jump ($c/t = 7.25$), a sudden decrease in the strengths of both the leading- and trailing-edge vortices can be inferred from the much weaker peaks on the u_{rms} profiles. However, a clear footprint of

leading-edge vortices coalescing with trailing-edge ones is still observed in the near wake. For the plate on the linear leg of the higher mode (c/t = 8.0), the secondary peak on the u_{rms} just upstream of the trailing-edge separation point suggest that the strength of leading-edge vortices are now slightly higher than those on the plate with c/t = 7.0. The low level of u_{rms} near the body surface and the fast decay of u_{rms} away from the surface may be a result of the coalescing of the leading- and trailing-edge vortices (see) before the leading-edge one actually arrives at the trailing edge (see Section 3.5.2). However, the secondary peak on the u_{rms} profile in the near wake indicates that the merger of the vortices occurs over a distance, and the footprint of the leading-edge may be still observed in the near wake. The u_{rms} profiles for the plate with c/t = 9.5 are similar to those for c/t = 6.5 and 7.0, except that the vortices are now stronger.

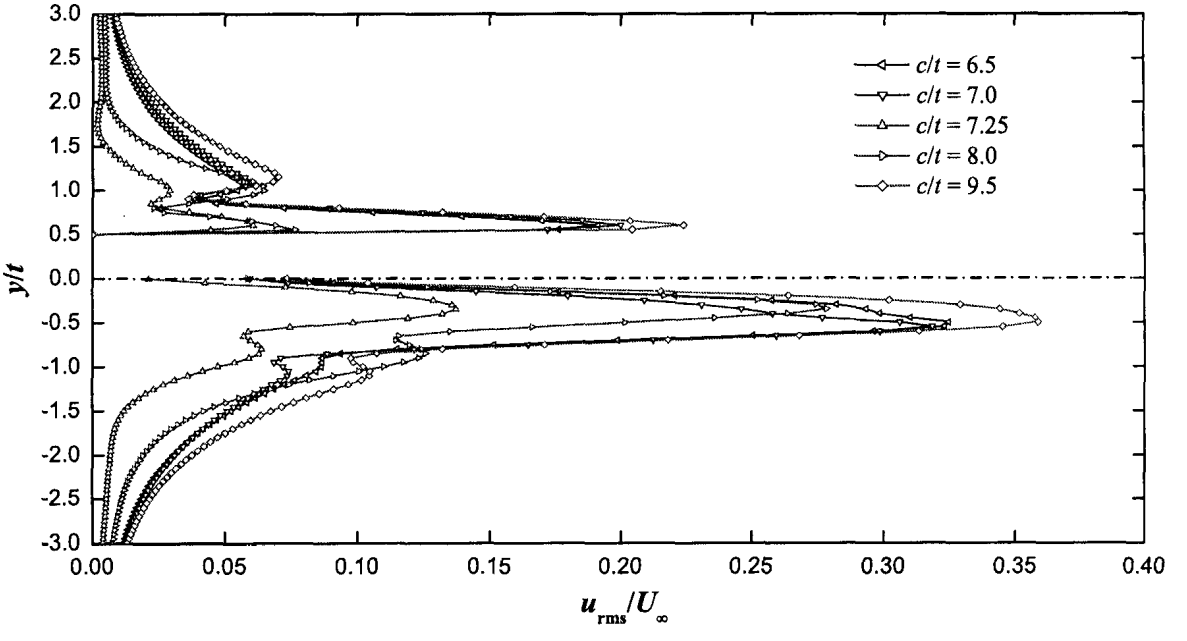

Figure 3.12. Streamwise r.m.s. velocity profiles for T90-R plates with c/t = 6.5, 7.0, 7.25, 8.0, and 9.5; upper half: just upstream of trailing-edge separation, lower half: 0.5t downstream of trailing-edge separation

3.5. THE SHEDDING PROCESS

To understand the effects of geometry on Strouhal numbers illustrated Section 3.3, a better understanding of the shedding process is necessary. In this Section, the flow fields around elongated bluff bodies are explored to reveal the geometric effects on various flow characteristics, based on which the changes in the underlying shedding process that lead to the observed St_c jumps, and the linear and horizontal legs (as well as the transition between them) in the St_c map, are explained.

3.5.1. The Vorticity Field

Figure 3.13 compares the vorticity fields for four elongated bluff bodies at the moment when the lift is at its maximum. For the plate with a streamlined leading edge, there is no separation at the leading edge and the boundary layers develop on the upper and lower surfaces of the body until the trailing edge is encountered, where the boundary layers separate and directly interact with each other in the near wake to form a regular vortex street. As a result, the shedding process mimics that from a circular cylinder, although some subtle differences exist (see Section 1.3 for a discussion).

The vorticity fields for the two plates with $\theta = 90^{\circ}$ triangular leading edges are essentially the same. This is expected since from Figure 3.5 the Strouhal numbers are the same for both plates. Figure 3.14 shows how the vorticity fields compare when the Strouhal numbers for these two plates with $c/t = 7.5$ are slightly different. It can be observed that the vorticity fields are similar, although the distances between vortices in the wake are different (accounting for the different shedding frequencies). However, the

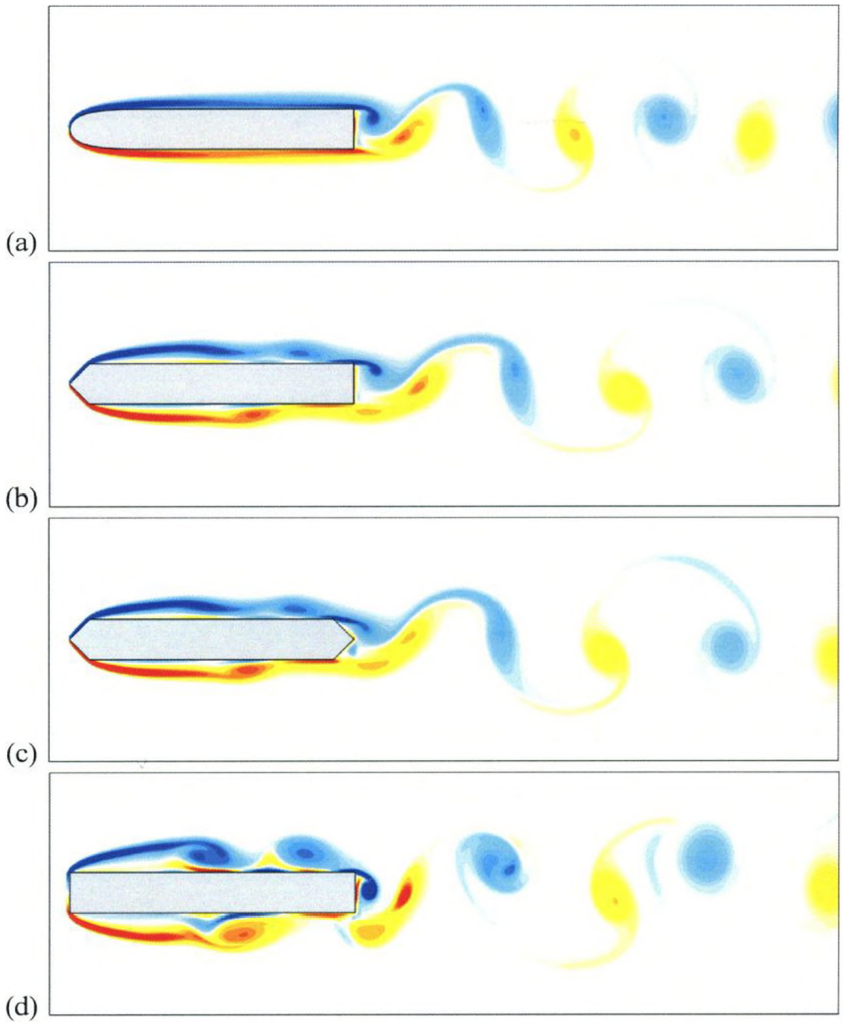

Figure 3.13. Vorticity fields corresponding to maximum lift for various bluff bodies at Re = 600; (a) O-R plate with c/t = 7; (b) T90-R plate with c/t = 7; (c) T90-T90 plate with c/t = 7; (d) R-R plate with c/t = 7.

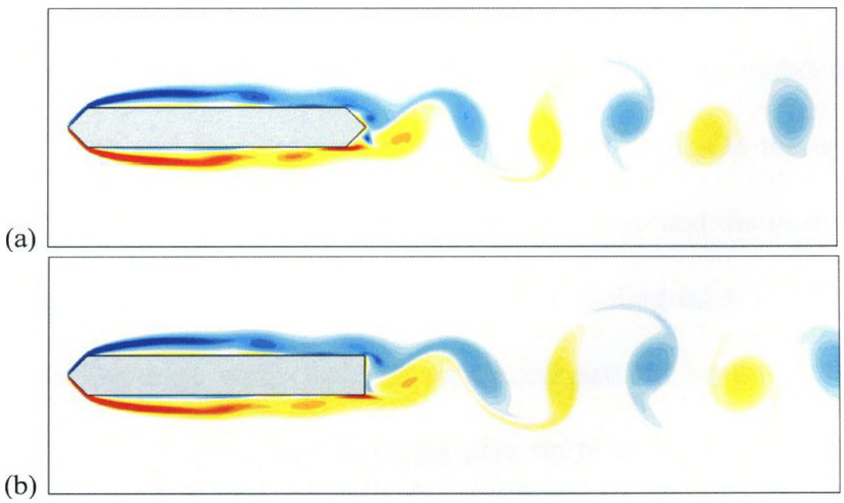

Figure 3.14. Vorticity fields corresponding to maximum lift for plates with a $\theta = 90^{\circ}$ triangular leading edge at Re = 600; (a) T90-T90 plate with c/t = 7.5; (b) T90-R plate with c/t = 7.5.

near wake appears to be similar for both plates. In fact, it has been shown in Figure 3.9 that the length of the formation region for the T90-T90 plate is longer than the triangular nose ($0.5t$), and is very close to that for the T90-R plate. This seems to indicate that, in this case, the interference of the trailing-edge nose with the formation region is not the main reason for the discrepancy in Strouhal numbers. Actually, a simple calculation shows that, Strouhal numbers based on surface lengths for these two plates are almost the same. Hence, for this case only, the discrepancy in St_c is mainly caused by the difference in surface lengths. The vorticity field for the R-R plate in Figure 3.13 (d) is similar to those around the T90-R and T90-T90 plates, although the leading-edge vortices are larger and stronger.

Figure 3.15 shows a sequence of snapshots of the vorticity field at time intervals of $\Delta T = 1$ for a T90-T90 plate with $c/t = 7$ at $Re = 600$. In frame (a), there is a leading-edge vortex on the upper surface convecting towards the trailing edge, and a trailing-edge vortex is growing. On the lower surface, a leading-edge vortex is coalescing with the trailing-edge one behind the trailing edge, and another leading-edge vortex attached to the shear layer is still growing. In frame (b), the merging vortices behind the lower trailing-edge are shed as a pair into the wake, and the leading-edge vortex upstream is cut from the shear layer and starts to convect to the trailing-edge. On the upper surface, a leading-edge vortex is convecting closer to the trailing edge and the trailing-edge vortex is still growing. The next frame shows that the upper trailing-edge vortex is about to be shed, while a leading-edge vortex has just convected past the trailing edge and starts to coalesce with the trailing-edge one. A vortex also starts to grow at the end of the shear layer from the upper leading edge. On the lower surface, a leading-edge vortex is moving

closer to the trailing edge, and a trailing-edge vortex starts to grow. The last frame shows the same coalescing process at the upper trailing-edge as in frame (a) at the lower trailing-edge, and the lower trailing-edge vortex is growing larger while a leading-edge vortex is moving closer. This completes approximately half a shedding cycle. This process repeats itself and a regular vortex street is observed in the wake, since the trailing- edge merging is regular for this plate.

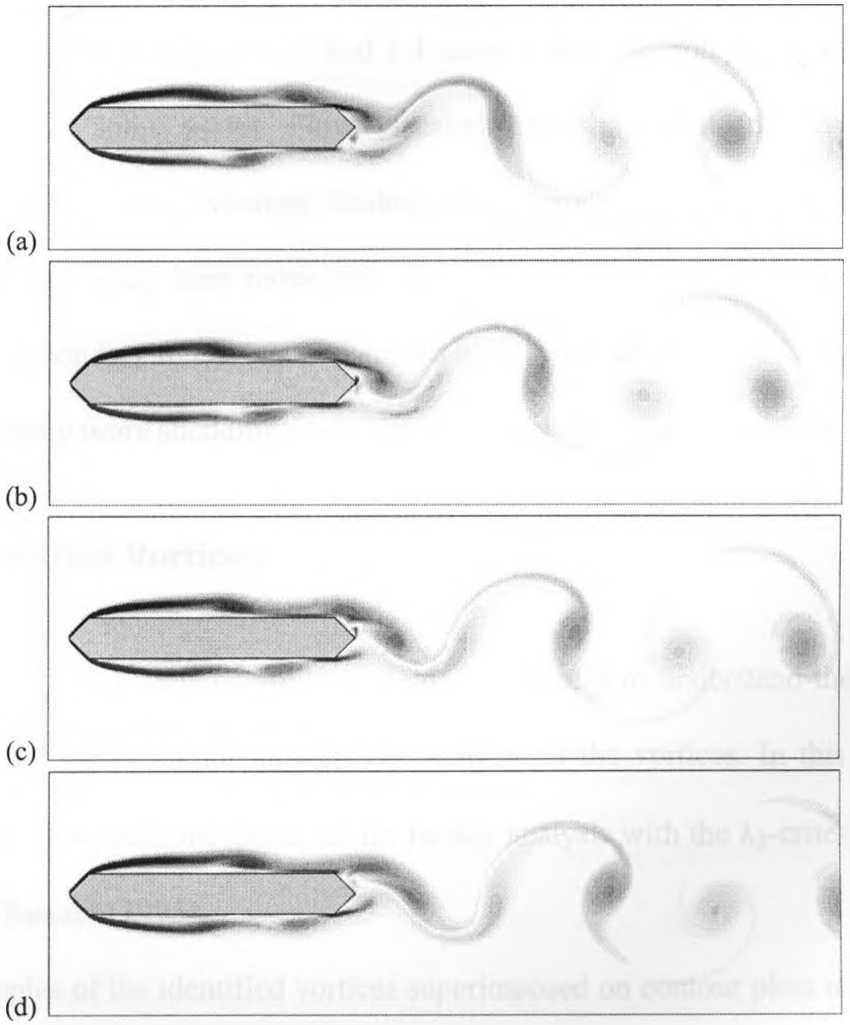

Figure 3.15. Vorticity field for a T90-T90 plate with c/t = 7 at Re = 600. The time interval between successive images in $\Delta T = 1$.

It can be observed that trailing-edge vortices only form in-between the passage of leading-edge vortices, and the shedding of the coalescing vortices as a pair at the trailing edge corresponds to the end of the growth of a leading-edge vortex. As discussed in Chapter 1 and Section 2.4.3, this is the reason that the shedding frequencies are locked to the chord of the body. Comparing the above observations with those in Section 2.4.3 for a rectangular plate shows that the flow patterns and shedding processes are similar for both plates.

The St_c maps in Figures 3.3 and 3.4 show a few secondary peaks just before or after a jump for some plates. Flow visualizations show that this may be due to randomness in the flow, whereby leading-edge vortices do not always merge with trailing-edge ones while they move into the wake. This usually happens intermittently and, hence, a secondary frequency is observed in the spectral analysis. To fully verify this assumption, many more shedding cycles (much longer simulations) would be necessary.

3.5.2. Identified Vortices

Although the contour plots of vorticity fields are helpful to understand the flow fields, they are not the best tool for quantitative analysis of the vortices. In this Section, the vortices in the flow field are identified for further analysis with the λ_2-criterion proposed by Jeong & Hussain (1995).

Examples of the identified vortices superimposed on contour plots of the vorticity field are shown in Figure 3.16. The identified vortices are represented by thick-line circles. The centre of the circle is determined from the "centre of mass" of the identified vortex, while the radius is calculated from the area occupied by the identified vortex.

Thus, the area of the representing circle is the same as the area of the identified vortex, although the shape is different.

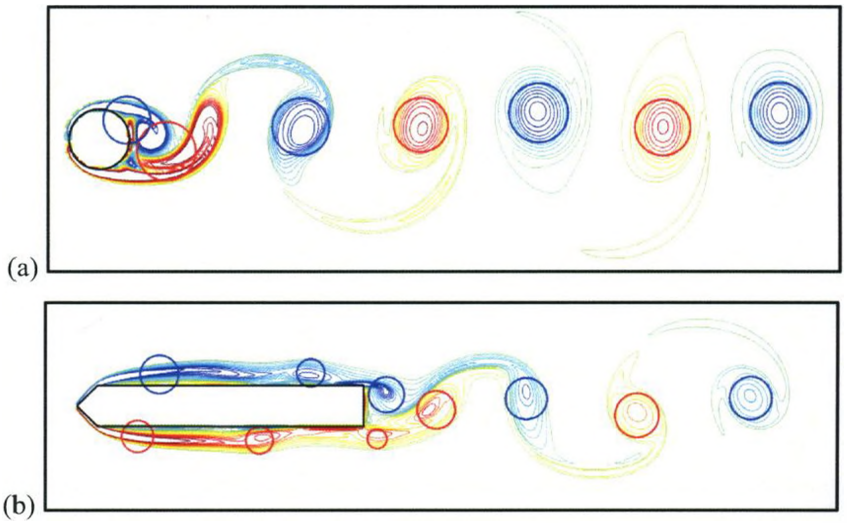

Figure 3.16. Identified vortices superimposed on vorticity contours at Re = 600; (a) circular cylinder (b) T90-R plate with $c/t = 7$

The above method is applied to identify the vortices in the flow fields around T90-R plates. Table 3.3 lists the maximum number of identified leading-edge vortices simultaneously convecting on the upper surface of the plate ($N_{LEV\max}$) in each shedding cycle, in which the mode number is determined from Figure 3.5. Table 3.3 shows that, contrary to the conclusion inferred from Chapter 1 – that the mode number is the same as the number of leading-edge vortices simultaneously convecting on the surface – the latter may be less than the former by 1. This occurs for the shorter plates of modes 2 and 3 in Table 3.3. A closer look at Figure 3.5 reveals that these plates are all on the linear legs of modes 2 and 3. This means that, a jump is not necessarily accompanied by an increase of leading-edge vortices on the surface of the body as it is for rectangular plates ($\theta = 180^{\circ}$), and only when a plate is long enough to allow an $N_{LEV\max}$ that equals the mode number is it on a horizontal leg in the St_c map.

Table 3.3. Maximum number of identified leading-edge vortices simultaneously convecting on the upper surfaces of T90-R plates in each shedding cycle

Mode	1		2						3						
c/t	4.0	4.5	5.0	5.5	5.75	6.0	6.5	7.0	7.25	7.5	8.0	8.25	8.5	9.0	9.5
$N_{LEV\max}$	1	1	1	1	1	2	2	2	2	2	2	2	3	3	3

Figure 3.17 shows the distance (d_{LT}) between a trailing-edge vortex that just starts to form ($\pm 0.5t/U_\infty$ since the velocity and vorticity fields were sampled at intervals of ΔT = 0.5 before identifying the vortices) and the closest leading-edge vortex for the T90-R plates. In the figure, the solid circles are the average values of the data (hollow squares) gathered from the identified vortices, solid lines are a fit to the average values, and broken lines are reference lines with unity slope (parallel to the line $d_{LT}/t = c/t$). It can be observed that the distance d_{LT} increases with c/t until a jump occurs. This jump coincides with the jump at the same elongation ratio in the St_c map. For c/t on a linear leg in the St_c map, d_{LT}/t increases almost as fast as c/t, and the increasing rate starts to level off at an elongation ratio corresponding to the transition to a horizontal leg. After the jump the process repeats itself. It is interesting to note that, the drastic decrease of d_{LT} at the jump (c/t = 7.25) in Figure 3.17 is not caused by an increase of the number of leading-edge vortices. Rather, it is due to the change of timings of the formation of leading- and trailing-edge vortices, which will be explored next.

With the identified vortices, further analyses are carried out for the plates with c/t = 6.5 (on the horizontal leg of mode 2, see Figure 3.5), 7.0 (before jump to mode 3), 7.25 (after jump to mode 3), 8.0 (on the linear leg of mode 3) and 9.5 (on the horizontal leg of mode 3). Figure 3.18 shows the strengths of the identified leading-edge vortices (Γ_{LEV}) along the surface of the plates, in which x is measured from the tip of the leading-edge

nosing, and the smooth curves are polynomial fits to the data. It can be observed that, the identified leading-edge vortices make their first appearance at almost the same distance from the leading edge (3.3-3.5t) for all plates under investigation, and their initial strengths are comparable (1.2-1.4$U_\infty t$), except for the plate with c/t = 7.25 (immediately after the jump) the leading-edge vortices are much weaker. For plates of the same mode (e.g., c/t = 6.5 and 7.0) in the St_c map (see Figure 3.5), leading-edge vortices are stronger on longer plates, and the evolution of Γ_{LEV} along the surface shows some similarity (the evolution curves are almost parallel to each other). At an St_c jump to a higher mode, Γ_{LEV} also jumps to a lower value, and the vortices tend to diffuse more slowly along the plate. For plates on horizontal legs in the St_c map, leading-edge vortices may convect beyond the trailing edge before coalescing with the trailing edge vortices, while the beginning of the merger usually occurs before the trailing edge for plates on a linear leg.

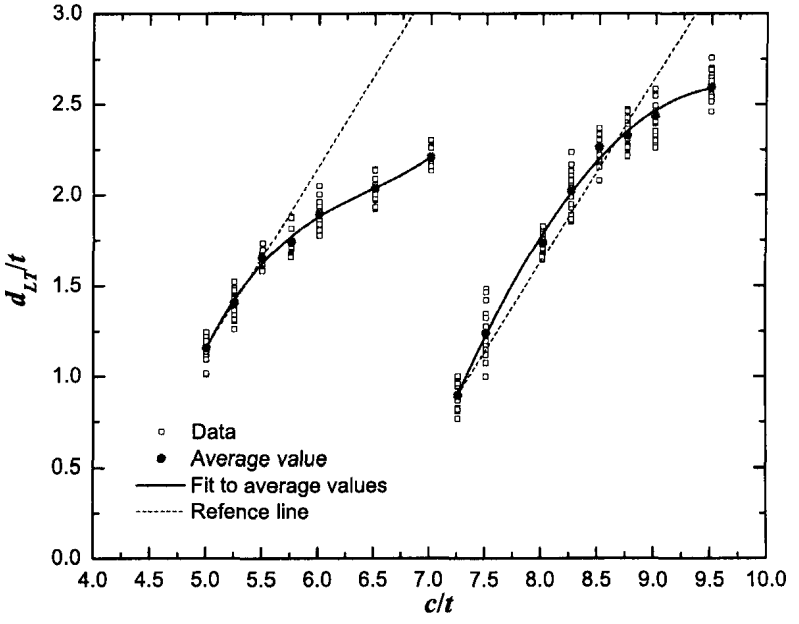

Figure 3.17. Distance between a forming trailing-edge vortex and the closest leading-edge one for a T90-R plate

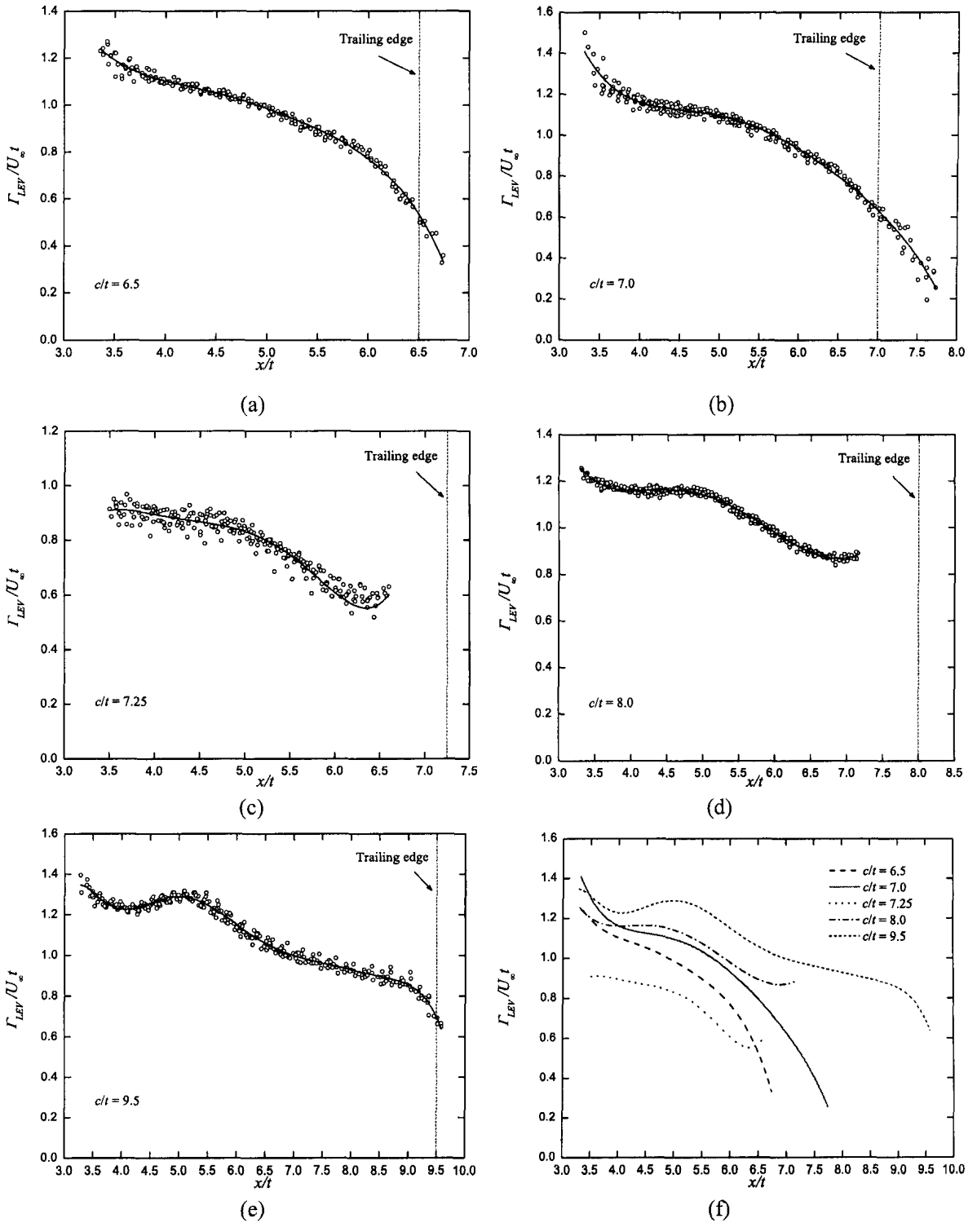

Figure 3.18. Strengths of identified leading-edge vortices along the surface of T90-R plates. Smooth curves are polynomial fit to the data; (a) $c/t = 6.5$; (b) $c/t = 7.0$; (c) $c/t = 7.25$; (d) $c/t = 8.0$; (e) $c/t = 9.5$; (f) fitted curves. x is measured from the leading edge.

The convection speed of leading-edge vortices (U_c) along the surfaces of the plates are presented in Figure 3.19. Again the smooth curves are polynomial fits to the data. Figure 3.19 shows that, the leading-edge vortex usually begins with a convection speed of a little less than half of the freestream velocity, then decelerates quickly until its distance from the leading edge is about 4-4.5t, where the speed reaches its minimum ($U_{c\min}$ = 0.35-0.4U_∞) and the vortex starts to accelerate towards the trailing edge. These observations are consistent with those reported in Tan *et al.* (2004).

The solid circles in Figures 3.19 (a-e) mark the data points occur at the same moment ($\pm 0.5t/U_\infty$ due to the sampling interval of $\Delta T = 0.5$) when a leading-edge vortex merges with a trailing-edge one. It can be observed that, for c/t = 6.5, 7.0, 7.25 and 8.0, a coalescing event at the trailing edge usually occurs just after the leading-edge vortex reaches $U_{c\min}$ and starts to accelerate towards the trailing edge; while for c/t = 9.5, coalescing events occur just before $U_{c\min}$ is reached. Flow visualizations (not shown here) have revealed that a leading-edge vortex usually reaches its minimum convection speed just before it is cutoff (shed) from the leading-edge shear layer (which is also suggested by Tan *et al.* 2004). This means that, for c/t = 6.5, 7.0, 7.25 and 8.0, the merger of a leading-edge vortex and a trailing-edge one at the trailing edge usually leads to the shedding of another leading-edge vortex. For c/t = 9.5, however, the merger occurs before another leading-edge vortex is shed. An additional analysis shows that this also happens when c/t = 9.0. A possible explanation is that, for c/t = 9.0 and 9.5, there are always 3 leading edge vortices on the surface of the body, of which the one in the middle may interfere with the transmission of the feedback signals produced by the coalescing event back to the leading edge.

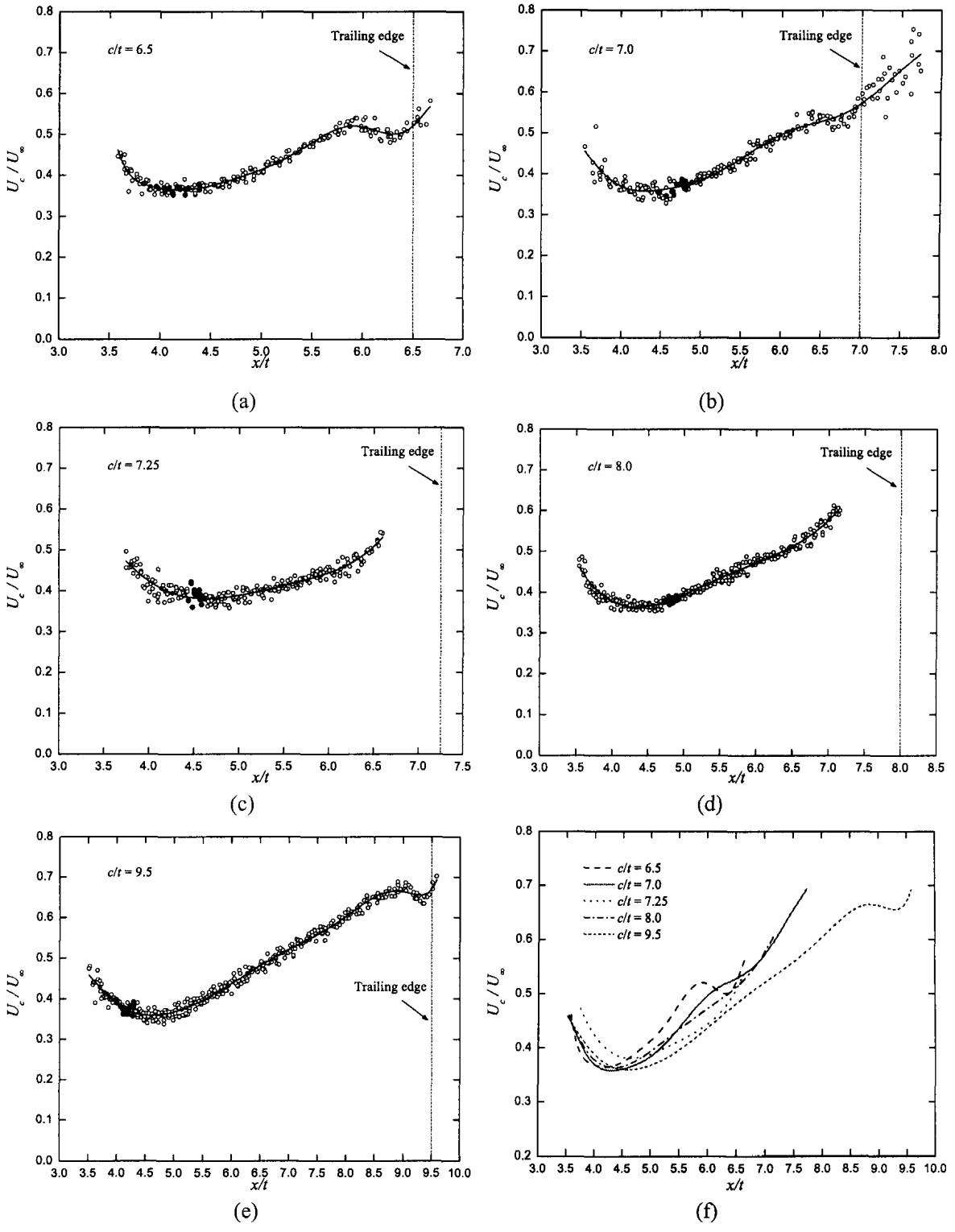

Figure 3.19. Convection speed of identified leading-edge vortices along the surface of T90-R plates. Smooth curves are polynomial fit to the data; (a) $c/t = 6.5$; (b) $c/t = 7.0$; (c) $c/t = 7.25$; (d) $c/t = 8.0$; (e) $c/t = 9.5$; (f) fitted curves. x is measured from the leading edge.

The strengths of identified trailing-edge vortices (Γ_{TEV}) are present in Figure 3.20, in which x is measured from the trailing-edge separation point, and the smooth curves are again polynomial fits to the data. It can be observed from Figure 3.20 that, for plates on horizontal legs in the St_c map, trailing-edge vortices have a better opportunity to develop more fully prior to merging with leading-edge one. The strength of the vortex grows rapidly while slowly moving away from the body, until it saturates at its maximum value (1.4-1.84$U_\infty t$ in Figure 3.20) and becomes almost constant before the merger occurs. For plates on linear St_c legs, the merger usually happens prematurely. In such cases, however, the disappearance of trailing-edge vortices in Figure 3.20 does not necessarily mean that coalesced vortex has been shed into the wake. Since, as long as the two vortices starts to connect, the whole region occupied by both vortices will be identified as a single, larger vortex in the vortex identification process. Vorticity field plots show that the merged vortex may remain attached to the trailing-edge shear layer, and its strength may continue to grow. However, it is reasonable to assume that the drastic change of timing for the merger of leading- and trailing-edge vortices for plates with c/t = 7.0 and 7.25 is the reason for the St_c jump to occur at c/t = 7.25.

3.5.3. Effects of Geometry on the Shedding Process

Table 3.4 summarizes the effects of increasing c/t on vortex shedding from a T90-R plate identified so far in the present investigation. At an St_c jump to a higher mode, where the shedding frequency f_v jumps to a higher value, the reattachment length x_r and the formation length in the wake L_w both reach their local maxima, and the distance between a forming trailing-edge vortex and the closest leading-edge one d_{LT} jumps from its local

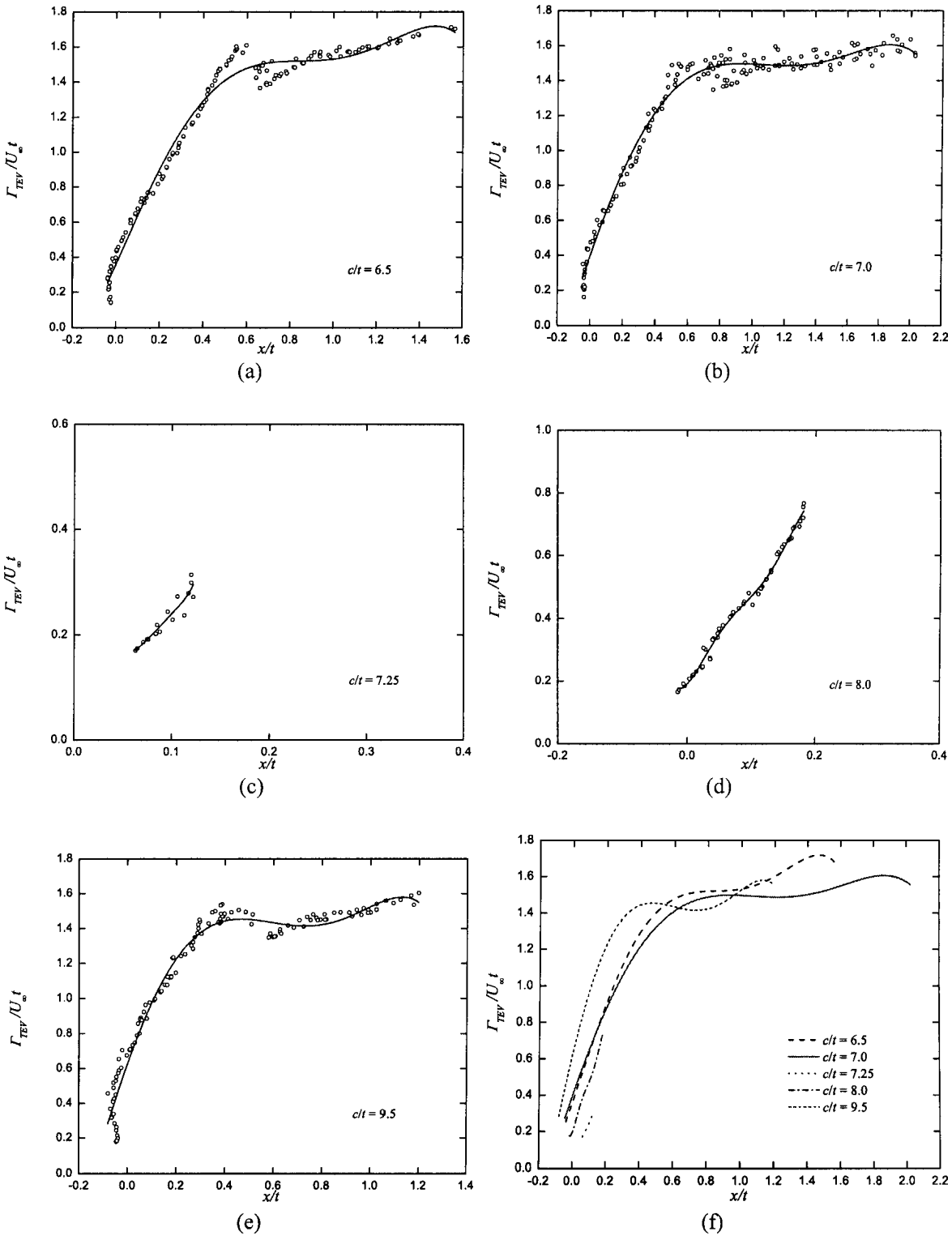

Figure 3.20. Strengths of identified trailing-edge vortices in the near wake of T90-R plates. Smooth curves are polynomial fit to the data; (a) c/t = 6.5; (b) c/t = 7.0; (c) c/t = 7.25; (d) c/t = 8.0; (e) c/t = 9.5; (f) fitted curves. x is measured from the trailing-edge separation point.

maximum to its local minimum. The strengths of leading-edge vortices Γ_{LEV} also jump to a lower value. After the jump, the variation of St_c follows the linear leg of the higher mode, where f_v remains almost constant, L_w decreases with c/t, while d_{LT} and Γ_{LEV} keep increasing with c/t. On the linear leg, the maximum number of leading-edge vortices simultaneously convecting on the surface $N_{LEV\max}$ is less than the mode number by one, and they start to merge with the trailing-edge ones before they reach the trailing edge. Further increase of c/t eventually leads to a transition from the linear leg to the horizontal leg, where $N_{LEV\max}$ increases by one and is now equal to the mode number, and L_w reaches its local minimum. On the horizontal leg, leading-edge vortices tend to convect past the trailing edge before they start to merge with the trailing-edge one; f_v starts to decrease, while x_r, L_w, and d_{LT} all increases with c/t, until the next St_c jump is encountered.

Table 3.4. Effects of increasing c/t on vortex shedding from a T90-R plate

	At an St_c jump	On a linear leg	On a horizontal leg
f_v	Jumps to higher value	Almost constant	Decreases
x_r	Local maximum	Decreases or increases	Increases
L_w	Local maximum	Decreases	Increases
d_{LT}	Jumps from local maximum to local minimum	Increases as fast as c	Increases slower than c
Γ_{LEV}	Jumps to lower value	Increases	Increases
$N_{LEV\max}$	No change	< mode number	+1 at transition from linear leg = mode number
Comments	Mode number + 1	Leading- and Trailing-edge vortices start to merge before trailing edge	Leading- and Trailing- edge vortices start to merge after trailing edge

Based on the observed effects of geometry on the flow characteristics, the changes in the underlying shedding process may be described as follows. Start with a horizontal leg on the St_c map, where x_r, L_w, and d_{LT} all increase with c/t. An increasing c/t

means a longer distance for the leading-edge vortices to travel, and because the trailing-edge shedding only occurs in-between the passage of leading-edge vortices, a larger d_{LT} and a lower shedding frequency are observed. A larger d_{LT} leads to a longer and thicker shear layer to roll up into a stronger trailing-edge vortex, and, when it is sufficiently long (near the end of a horizontal leg), the trailing-edge shedding mimics that from an O-R plate. Evidence can be found in Figure 3.8 that formation lengths of a T90-R plate near St_c jumps (c/t = 5 and 7) are very close to those of an O-R plate. Hence, it is reasonable to assume that, when c/t has increased past the end of the horizontal leg, the trailing-edge shedding is strong enough to take control of the shedding process, and the trailing-edge shedding frequency jumps to a higher value close to that of an O-R plate. Since the shedding frequency is now much higher, while c/t is increased and, from Figure 3.19 there is no significant increase in the convection speed of leading-edge vortices after a jump, the adjustment of the timing of the leading-edge vortices arriving at the trailing edge is achieved by a noticeable increase in x_r. Although d_{LT} is at its local minimum immediately after the jump, the jump of Γ_{LEV} to a much lower value (which may be due to the fact that there is less time for the leading-edge vortex to grow before it is shed at a higher frequency) ensures that the trailing-edge shedding is still in control of the shedding process, and hence, St_c follows a linear leg (or f_v is almost constant) with increasing c/t. The premature coalescence of the leading- and trailing-edge vortices before the former reaches the trailing edge (see Section 3.5.2) may also help the trailing-edge shedding dominate the shedding process, but the underlying mechanics are not entirely clear yet. A further increase in c/t leads to stronger Γ_{LEV} and larger d_{LT}. Figure 3.17 shows that, d_{LT} increases almost as fast as c/t on a linear leg, leaving a stronger

leading-edge vortex close to the end of the leading-edge shear layer. While not fully verified with the present data, it seems reasonable to assume that the leading-edge shear layer may re-establish its undisturbed shedding process due to close proximity of a strong vortex. When the elongation ratio is increased past the transition point from the linear to horizontal leg, an additional leading-edge vortex is shed during each shedding cycle due to the re-establishment of the "natural" shedding process of the leading-edge separation bubble (see Section 1.2.2), and the leading-edge shedding starts to predominate in the overall shedding process (which is described in Chapter 1 for rectangular plates, see also Section 3.5.1 for visualizations of the shedding) until the next St_c jump is encountered. It can be inferred from the description that, it is the alternate predominance of the leading- and trailing-edge shedding in the overall shedding process that leads to the linear and horizontal variations, and abrupt jumps of St_c.

For plates with larger separation angles (larger θ), the jumps occur at larger c/t ratios because longer shear layers (larger d_{LT}) and stronger trailing-edge shedding are necessary to overcome the stronger leading-edge shedding. The linear leg may become shorter because the strong leading-edge shedding tends to take back control of the overall shedding process quickly after the jump.

CHAPTER 4

CONCLUDING REMARKS

4.1. SUMMARY AND CONCLUSIONS

In the present study, a 2-D, high-resolution, vortex particle method was implemented, and its validity and capabilities were demonstrated through comparisons with experimental and numerical data available in the literature for flows around bluff bodies. The capability of the code to run long time simulations of bluff-body flows was demonstrated by replicating the *St-Re* relationships for circular and square cylinders. For circular cylinders, the predicted Strouhal numbers are in good agreement with experimental data in the laminar flow region, but the present 2-D simulations are unable to capture the discontinuities in the transitional region and tend to overpredict Strouhal numbers at higher Reynolds numbers. On the other hand, the Strouhal numbers from the present simulations for square cylinders are in reasonable agreement with experimental data from low to moderate Reynolds numbers. The ability of the method to handle complex flow phenomena is further illustrated by long time simulations of flows around elongated bodies. The successful replication of the stepwise variation of the chord-based Strouhal numbers for rectangular cylinders, and the favorable comparisons of flow patterns from the present simulations with experimental observations, again suggest that the present code is capable of capturing the physics of interest with reasonable accuracy. The fact that the flow patterns from the present 2-D simulations at a moderate Reynolds number agree well with experimental observations at much higher Reynolds numbers

indicates that, although small differences in the flow fields are expected due to the large difference in Reynolds numbers and the absence of 3-D effects in these simulations, the energy-carrying, large-scale structures in the flows are correctly captured to a significant extent. Hence, with the convenience of running simulations on ordinary personal computers at low cost, the present 2-D vortex particle code can be a useful engineering tool for studies of various flow phenomena related to these large vortical structures, such as vortex shedding from bluff bodies.

With the 2-D vortex particle code, many simulations of the flow around flat plates with various nosings and elongation ratios were performed to investigate the effects of geometry on vortex shedding from elongated bluff bodies. The resultant St_c map (variation of chord-based Strouhal number with elongation ratio and nosing angle) reveals that there are two limits for St_c variations: horizontal lines (lower limit) where St_c is almost constant with increasing elongation ratio (c/t) until a sudden jump occurs, and a straight line (upper limit) where St_c varies almost linearly with c/t. By reducing the separation angle at the leading edge, the transition from the lower to upper limit appears to be continuous: St_c jumps occur earlier, and the sizes of which tend to be smaller, until finally they disappear and St_c variation follows a straight line. It was also discovered in the present study that, for plates with a smaller separation angle at the leading edge, St_c does not always jump directly onto a horizontal leg of a higher mode. Instead it settles at a somewhat lower value, and then follows a linear leg which eventually makes transition to the horizontal leg. Furthermore, an St_c jump is not necessarily accompanied by an increase of leading-edge vortices convecting on the body surface. The additional leading-

edge vortex appears on the surface only when St_c makes transition from the linear to the horizontal leg.

From the analyses of mean flow characteristics (reattachment lengths and formation lengths, mean velocity and r.m.s. velocity profiles), visualizations of the vorticity field, and quantitative analyses of identified vortices (number of vortices convecting on the surface, distance between leading- and trailing-edge vortices, evolution of the vortex strengths, and convection speed of the vortices), the effects of geometry on a number of properties of the flow around an elongated bluff body, which are linked to the jump, linear and horizontal legs of variation, and transition from linear to horizontal leg in the St_c map, were identified, and a summary of which for a T90-R plate is given in Table 3.4. Based on the observed effects of geometry on the flow characteristics, a detailed description of the mechanics leading to various behaviors of St_c was given. It is the alternate predominance of the leading- and trailing-edge shedding in the overall shedding process that leads to the linear and horizontal variations, and abrupt jumps of St_c. When the trailing-edge shedding is in control, the shedding process mimics that from a plate with a streamlined leading edge, and the shedding frequency jumps to a higher value and St_c tends to follow a linear leg in the map. When the leading-edge shedding predominates, St_c tends to follow a horizontal leg.

4.2. RECOMMENDATIONS

To the knowledge of the author, the present study is the first one dedicated to systematical investigation of the effects of geometry on vortex shedding from elongated

bluff bodies with various nosings. In light of the progress made in the present study, a few recommendations can be made for future studies.

As mentioned in Chapter 1, the present study is a first step toward a better understanding of geometry effects on vortex-induced vibrations of long-span bridges. The upper and lower surfaces of a bridge deck are usually asymmetric, while in the present study all the bluff bodies are symmetric about its horizontal center line. With a better understanding of the effects of leading-edge separation angles and elongation ratios, the effects of asymmetry of upper and lower surfaces is the next obstacle to a better understanding of vortex shedding from a bridge deck.

It has been shown in the literature that the motion of a bluff body, or external forcing, changes flow patterns significantly. A systematical study of the effects of geometry on vortex shedding from elongated bluff bodies under free or forced vibrations, or external forcing, will be another venue of improving the present understanding of vortex-induced vibration of bridges.

Furthermore, experimental studies on vortex shedding from flat plates with triangular nosings are rare in the literature. Although the numerical method implemented in the present work has been validated against experimental data for rectangular plates, many of the new findings made in the present study about geometric effects are completely based on numerical simulations at a relatively low Reynolds number. Hence, a detailed experimental study with a few carefully selected models (which is now possible due to an improved understanding of geometric effects from the present study) at higher Reynolds numbers will be an important contribution. As this will not only validate the findings in the present study, but it will also fill the gap in the literature.

REFERENCES

Abernathy, F.H. & Kronauer, R.E. (1962). The formation of vortex streets. *J. Fluid Mech., 13*, 1-20

Al-Jamal, H. & Dalton, C. (2004). Vortex induced vibrations using Large Eddy Simulation at a moderate Reynolds number. *J. Fluids Structs., 19*, 73-92

Alessandrini, G., Douglis, A. & Fabes, E. (1983). An approximate layering method for the Navier-Stokes equations in bounded cylinders. *Annali di matematica pura ed applicata, 135*, 329-347

Anderson, C. & Greengard, C. (1985). On vortex methods. *SIAM J. Numer. Anal., 22*, 413-440

Anderson, C.R. & Reider, M.B. (1996). A high order explicit method for the computation of flow about a circular cylinder. *J. Comput. Phys., 125*, 207-224

Bandyopadhyay, P.R. (1991). Instabilities and large structures in reattaching boundary layers. *AIAA J., 29*, 1149-1155

Bar-Lev, M. & Yang, H.T. (1975). Initial flow field over an impulsively started cylinder. *J. Fluid Mech., 72*, 625-647

Barba, L.A. (2004). *Vortex Method for computing high-Reynolds number flows: Increased accuracy with a fully mesh-less formulation.* PhD Thesis, Graduate Aeronautical Laboratories, California Institute of Technology.

Barnes, J.E. & Hut, P. (1986). A hierarchical O(NlogN) force-calculation algorithm. *Nature, 324*, 446-449

Beale, J.T. & Majda, A. (1981). Rates of convergence for viscous splitting of the Navier-Stokes Equations. *Math. Comput., 37*, 243-259

Beale, J.T. & Majda, A. (1982a). Vortex methods. I: Convergence in three dimensions. *Math. Comput., 39*, 1-27

Beale, J.T. & Majda, A. (1982b). Vortex methods. II: Higher order accuracy in two and three dimensions. *Math. Comput., 39*, 29-52

Beale, J.T. & Majda, A. (1985). High order accurate vortex methods with explicit velocity kernels. *J. Comput. Phys., 58*, 188-208

Bearman, P.W. (1965). Investigation of the flow behind a two-dimensional model with a blunt trailing edge and fitted with splitter plates. *J. Fluid Mech., 21*, 241-255

Bearman, P.W. (1967). On vortex street wakes. *J. Fluid Mech., 28*, 625-641

Bearman, P.W. (1984). Vortex shedding from oscillating bluff bodies. *Annu. Rev. Fluid Mech., 16*, 195-222

Bearman, P.W. & Owen, J.C. (1998). Reduction of bluff-body drag and suppression of vortex shedding by the introduction of wavy separation lines. *J. Fluids Structs., 12*, 123-130

Bearman, P.W. & Trueman, D.M. (1972). An investigation of the flow around rectangular cylinders. *Aeronaut. Q., 23*, 229-237

Benhaddouch, R. (1998). *Treatment of a Neumann boundary condition by a particle strength exchange method.* In: Proceedings of the Third International Workshop on Vortex Flows and Related Numerical Methods, August 24-27, 1998, Toulouse. pp.36-45

Berger, E. & Wille, R. (1972). Periodic flow phenomena. *Annu. Rev. Fluid Mech., 4*, 313-340

Billah, K.Y.R. (1989). *A study of vortex-induced vibration.* PhD Thesis, Department of Civil Engineering and Operations Research, Princeton University.

Bishop, R.E.D. & Hassan, A.Y. (1964). The lift and drag forces on a circular cylinder oscillating in a flowing fluid. *Proc. Roy. Soc. Lond. Ser. A, 227*, 51-75

Blazewicz, A.M., Bull, M.K. & Kelso, R.M. (2007). *Characteristics of flow regimes for single plates of rectangular cross-section.* In: Proceedings of 16th Australasian Fluid Mechanics Conference, December 3-7, 2007, Queensland, Australia. pp.935-938

Blevins, R.D. (1986). *Flow-induced vibration.* Malabar, Florida: Krieger Publishing Company.

Bloor, M.S. (1964). The transition to turbulence in the wake of a circular cylinder. *J. Fluid Mech., 19*, 290-304

Bouard, R. & Coutanceau, M. (1980). The early stage of development of the wake behind an impulsively started cylinder for $40 \leq \mathrm{Re} \leq 10^4$. *J. Fluid Mech., 101*, 583-607

Bradshaw, P. & Wong, F.Y.F. (1972). The reattachment and relaxation of a turbulent shear layer. *J. Fluid Mech., 52*, 113-135

Bull, M.K., Li, Y. & Pickles, J.M. (1995). *Effects of boundary layer transition on vortex shedding from thick plates with faired leading edge and square trailing edge.* In: Proceedings of 12th Australasain Fluid Mechanics Conference, December 15-20, 1995, Sydney, Australia. pp.231-234

Burgmann, S., Dannemann, J. & Schröder, W. (2008). Time-resolved and volumetric PIV measurements of a transitional separation bubble on an SD7003 airfoil. *Exp. Fluids, 44*, 609-622

Cao, C. & Hancock, P.E. (2004). Boundary layer development after a region of three-dimensional separated flow. *Eur. J. Mech. B Fluids, 23*, 519-533

Carrier, J., Greengard, L. & Rokhlin, V. (1988). A fast adaptive multipole algorithm for particle simulations. *SIAM J. Sci. Comput., 9*, 669-686

Castro, I.P. (2005). The stability of laminar symmetric separated wakes. *J. Fluid Mech., 532*, 389-411

Castro, I.P. & Epik, E. (1998). Boundary layer development after a separated region. *J. Fluid Mech., 374*, 91-116

Castro, I.P. & Haque, A. (1987). The structure of a turbulent shear layer bounding a separation region. *J. Fluid Mech., 179*, 439-468

Castro, I.P. & Haque, A. (1988). The structure of a turbulent shear layer bounding a separation region. Part. 2. effects of free-stream turbulence. *J. Fluid Mech., 192*, 577-595

Caughey, D.A. (2001). Implicit multigrid computation of unsteady flows past cylinders of square cross-section. *Comput. Fluids, 30*, 939-960

Cerretelli, C. & Williamson, C.H.K. (2003). The physical mechanism for vortex merging. *J. Fluid Mech., 475*, 41-77

Chatelain, P. & Leonard, A. (2008). Isotropic compact interpolation schemes for particle methods. *J. Comput. Phys., 227*, 3244–3259

Cherry, N.J., Hillier, R. & Latour, M.E.M.P. (1983). The unsteady structure of two-dimensional separated-and- reattaching flows. *J. Wind Eng. Ind. Aerod., 11*, 95-105

Cherry, N.J., Hillier, R. & Latour, M.E.M.P. (1984). Unsteady measurements in a separated and reattaching flow. *J. Fluid Mech., 144*, 13-46

Chomaz, J.M., Huerre, P. & Redekopp, L.G. (1988). Bifurcation to local and global modes in spatially developing flows. *Phys. Rev. Lett., 60*(1), 25-28

Chorin, A.J. (1973). Numerical study of slightly viscous flow. *J. Fluid Mech., 57*, 785-796

Christiansen, J.P. (1973). Numerical simulation of hydrodynamics by the method of point vortices. *J. Comput. Phys., 13*, 363-379

Collins, W.M. & Dennis, S.C.R. (1973a). Flow past an impulsively started circular cylinder. *J. Fluid Mech., 60*, 105-127

Collins, W.M. & Dennis, S.C.R. (1973b). The initial flow past an impulsively started circular cylinder. *Q. J. Mech. Appl. Math., 26*, 53-75

Cottet, G.-H. (1987). Convergence of a vortex-in-cell method for the two-dimensional Euler equations. *Math. Comput., 49*, 407-425

Cottet, G.-H. (1996). Artificial viscosity models for vortex and particle methods. *J. Comput. Phys., 127*, 299-308

Cottet, G.-H. & Koumoutsakos, P. (2000). *Vortex methods: theory and practice*. Cambridge: Cambridge University Press.

Cottet, G.-H., Michaux, B., Ossia, S. & Vanderlinden, G. (2002). A comparison of spectral and vortex methods in three-dimensional incompressible flows. *J. Comput. Phys., 175*, 702-712

Couet, B., Buneman, O. & Leonard, A. (1981). Simulation of three-dimensional incompressible flows with a vortex-in-cell method. *J. Comput. Phys., 39*, 305-328

Davenport, A.G. (1961). The application of statistical concepts to the wind loading of structures. *Proc. Inst. Civ. Eng., 19*, 449-472

Davenport, A.G. (1962). The response of slender line-like structures to a gusty wind. *Proc. Inst. Civ. Eng., 23*, 389-408

Davies, M.E. (1976). A comparison of the wake structure of a stationary and oscillating bluff body, using a conditional averaging technique. *J. Fluid Mech., 75*, 209-231

Davis, R.W. & Moore, E.F. (1982). A numerical study of vortex shedding from rectangles. *J. Fluid Mech., 116*, 475-506

Degond, P. & Mas-Gallic, S. (1989). The weighted particle method for convection-diffusion equations. Part 1. The case of an isotropic viscosity. *Math. Comput., 53*, 485-507

Djilali, N. & Gartshore, I.S. (1992). Effect of leading-edge geometry on a turbulent separation bubble. *AIAA J., 30*(2), 559-561

Doligalski, T.L., Smith, C.R. & Walker, J.D.A. (1994). Vortex interactions with walls. *Annu. Rev. Fluid Mech., 26*, 573-616

Driver, D.M., Seegmiller, H.L. & Marvin, J. (1987). Time-dependent behavior of a reattaching shear layer. *AIAA J., 25*, 914-919

Dutta, S., Panigrahi, P.K. & Muralidhar, K. (2008). Experimental investigation of flow past a square cylinder at an angle of incidence. *J. Eng. Mech., 134*(9), 788-803

Eaton, J.K. & Johnston, J.P. (1981). A review of research on subsonic turbulent flow reattachment. *AIAA J., 19*, 1093-1100

Ekaterinaris, J.A. (2005). High-order accurate, low numerical diffusion methods for aerodynamics. *Progr. Aero. Sci., 41*, 192-300

Eldredge, J.D. (2007). Numerical simulation of the fluid dynamics of 2D rigid body motion with the vortex particle method. *J. Comput. Phys., 221*, 626-648

Eldredge, J.D. (2008). Dynamically coupled fluid–body interactions in vorticity-based numerical simulations. *J. Comput. Phys., 227*, 9170-9194

Fage, A. & Johansen, F.C. (1928). The structure of vortex sheets. *Phil. Mag. Ser. 7, 5*(28), 417-441

Ferziger, J. (1993). Simulation of complex turbulent flows: recent advances and prospects in wind engineering. *J. Wind Eng. Ind. Aerod., 46 &47*, 195-212

Fey, U., König, M. & Eckelmann, H. (1998). A new Strouhal–Reynolds-number relationship for the circular cylinder in the range $47 < Re < 2\times10^5$. *Phys. Fluids, 10*, 779–794

Fischer, P.F. (1997). An overlapping Schwarz method for spectral element solution of the incompressible Navier–Stokes equations. *J. Comput. Phys., 133*, 84-101

Fitzgerald, M.J., Sheard, G.J. & Ryan, K. (2007). *Cylinders with square cross-section: Paths to turbulence with various angles of incidence.* In: Proceedings of the 16th Australasian Fluid Mechanics Conference, December 3-7, 2007, Queensland, Australia. pp.1055-1062

Franke, R., Rodi, W. & Schönung, B. (1990). Numerical calculation of laminar vortex-shedding flow past cylinders. *J. Wind Eng. Ind. Aerod., 35*, 237-257

Friedmann, A. (1964). *Partial differential equations of parabolic type.* Englewood Cliffs, NJ: Printice-Hall.

Fujii, K. (2005). Progress and future prospects of CFD in aerospace - Wind tunnel and beyond. *Progr. Aero. Sci., 41*, 455-470

Fureby, C. (2008). Towards the use of large eddy simulation in engineering. *Progr. Aero. Sci., 44*, 381-396

Gabbai, R.D. & Benaroya, H. (2005). An overview of modeling and experiments of vortex-induced vibration of circular cylinders. *J. Sound Vib., 282*, 575-616

Gal, P.L. & Croquette, V. (2000). Visualization of the space-time impulse response of the subcritical wake of a cylinder. *Phys. Rev. E, 62*(3), 4424-4426

Gerrard, J.H. (1966). The mechanics of the formation region of vortices behind bluff bodies. *J. Fluid Mech., 25*, 401-413

Gerrard, J.H. (1978). The wakes of cylindrical bluff bodies at low Reynolds number. *Phil. Trans. Roy. Soc. Lond. Ser A, 288*, 351-382

Goldburg, A. & Florsheim, B.H. (1966). Transition and Strouhal number for the incompressible wake of various bodies. *Phys. Fluids, 9*(1), 45-50

Graham, J.M.R. (1980). The forces on sharp-edged cylinders in oscillatory flow at low Keulegan-Carpenter numbers. *J. Fluid Mech., 97*, 331-346

Greengard, L. & Rokhlin, V. (1987). A fast algorithm for particle simulations. *J. Comput. Phys., 73*, 325-348

Greengard, L. & Strain, J. (1990). A fast algorithm for the evaluation of heat potentials. *Comm. Pure Appl. Math., 43*, 949-963

Griffin, O.M. (1978). A universal Strouhal number for the 'locking-on' of vortex shedding to the vibrations of bluff cylinders. *J. Fluid Mech., 85*, 591-606

Griffin, O.M. (1981). Universal similarity in the wakes of stationary and vibrating bluff structures. *J. Fluids Eng. Trans. ASME, 103*, 52-58

Griffin, O.M. & Hall, M.S. (1991). Review – vortex shedding lock-on and flow control in bluff body wakes. *J. Fluids Eng. Trans. ASME, 113*, 526-537

Griffin, O.M. & Ramberg, S.E. (1974). The vortex-street wakes of vibration cylinders. *J. Fluid Mech., 66*, 553–576

Hald, O.H. (1979). Convergence of vortex methods for Euler's equations. II. *SIAM J. Numer. Anal., 16*, 726-755

Hald, O.H. (1987). Convergence of vortex methods for Euler's equations. III. *SIAM J. Numer. Anal., 24*, 538-582

Hammache, M. & Gharib, M. (1991). An experimental study of the parallel and oblique vortex shedding from circular cylinders. *J. Fluid Mech., 232*, 567-590

Hancock, P.E. (2000). Low Reynolds number two-dimensional separated and reattaching turbulent shear flow. *J. Fluid Mech., 410*, 101-122

Henderson, R.D. (1997). Nonlinear dynamics and pattern formation in turbulent wake transition. *J. Fluid Mech., 352*, 65-112

Hockney, R.W., Goel, S.P. & Eastwood, J.W. (1973). A 10000 particle molecular dynamics model with long range forces. *Chem. Phys. Lett., 21*, 589-591

Hourigan, K., Thompson, M.C. & Tan, B.T. (2001). Self-sustained oscillations in flows around long blunt plates. *J. Fluids Structs., 15*, 387-398

Hu, J.C., Zhou, Y. & Dalton, C. (2006). Effects of the corner radius on the near wake of a square prism. *Exp. Fluids, 40*, 106-118

Huang, M.-J., Su, H.-X. & Chen, L.-C. (2009). A fast resurrected core-spreading vortex method with no-slip boundary conditions. *J. Comput. Phys., 228*, 1916-1931

Huberson, S., Rivoalen, E. & Voutsinas, S. (2008). Vortex particle methods in aeroacoustic calculations. *J. Comput. Phys., 227*, 9216–9240

Hudy, L.M., Haguib, A.M. & Humpheys, W.M. (2003). Wall-pressure-array measurements beneath a separating/reattaching flow region. *Phys. Fluids, 15*, 706-717

Huerre, P. & Monkewitz, P.A. (1990). Local and global instabilities in spatially developing flows. *Annu. Rev. Fluid Mech., 22*, 473-537

Jeong, J. & Hussain, F. (1995). On the identification of a vortex. *J. Fluid Mech., 285*, 69–94

Katz, J. & Plotkin, A. (2001). *Low-speed aerodynamics* (2nd ed.). New York: Cambridge University Press.

Khalak, A. & Williamson, C.H.K. (1999). Motions, forces and mode transitions in vortex-induced vibrations at low mass-damping. *J. Fluids Structs., 13*, 813-851

King, J.P.C. (2003). The foundation and the future of wind engineering of long span bridges – the contributions of Alan Davenport. *J. Wind Eng. Ind. Aerod., 91*, 1529–1546

Kiya, M. & Sasaki, K. (1983). Structure of a turbulent separation bubble. *J. Fluid Mech., 137*, 83-113

Kiya, M., Shimizu, M. & Mochizuki, O. (1997). Sinusoidal forcing of a turbulent separation bubble. *J. Fluid Mech., 342*, 119-139

Koch, W. (1985). Local instability characteristics and frequency determination of self-excited wake flows. *J. Sound Vib., 99*, 53-83

Koumoutsakos, P.D. (1993). *Direct numerical simulations of unsteady separated flows using vortex methods.* PhD Thesis, Graduate Aeronautical Laboratories, California Institute of Technology.

Koumoutsakos, P.D. (2005). Multiscale flow simulations using particles. *Annu. Rev. Fluid Mech., 37*, 457–487

Koumoutsakos, P.D. & Leonard, A. (1995). High-resolution simulations of the flow around an impulsively started cylinder using vortex methods. *J. Fluid Mech., 296*, 1-38

Koumoutsakos, P.D., Leonard, A. & Pépin, F. (1994). Boundary conditions for viscous vortex methods. *J. Comput. Phys., 113*, 52-61

Kuethe, A.M. & Chow, C.-Y. (1986). *Foundations of Aerodynamics: Bases of Aerodynamic Design* (4th ed.). New York: John Wiley & Sons Inc.

Lakkis, I. & Ghoniem, A. (2009). A high resolution spatially adaptive vortex method for separating flows. Part I: Two-dimensional domains. *J. Comput. Phys., 228*, 491-515

Lane, J.C. & Loehrke, R.I. (1980). Leading edge separation from a blunt plate at low Reynolds number. *J. Fluids Eng. Trans. ASME, 102*, 494-496

Laneville, L., Gartshore, I.S. & Parkinson, G.V. (1977). *An explanation of some effects of turbulence on bluff bodies.* In: Proceedings of the 4th International Conference on Wind Effects on Buildings and structures, 1977. Cambridge: Cambridge University Press. pp.333-341

Larsen, A., Eshahl, S., Andersen, J.E. & Vejrum, T. (2000). Storebælt suspension bridge–vortex shedding excitation and mitigation by guide vanes. *J. Wind Eng. Ind. Aerod., 88*, 283-296

Leonard, A. (1980). Vortex methods for flow simulation. *J. Comput. Phys., 37*, 289-335

Leonard, A., Shiels, D., Salmon, J.K., Winckelmans, G.S. & Ploumhans, P. (1997). *Recent advances in high resolution vortex methods for incompressible flows.* In: 13th Computational Fluid Dynamics Conference, AIAA Paper 97-2108, June 29-July 2, 1997, Snowmass Village, Colorado.

Lienhard, J.H. (1966). *Synopsis of lift, drag and vortex frequency data for rigid circular cylinders.* Research Division Bulletin 300, College of Engineering, Washington State University.

Lighthill, M.J. (1963). Introduction. Boundary layer theory. In L. Rosenhead (Ed.), *Laminar Boundary Layers.* Oxford: Oxford University Press.

Lotfy, A. & Rockwell, D. (1993). The near-wake of an oscillating trailing edge: mechanisms of periodic and aperiodic response. *J. Fluid Mech., 251*, 173-201

Luo, S.C., Chew, Y.T. & Ng, Y.T. (2003). Characteristics of square cylinder wake transition flows. *Phys. Fluids, 15*, 2549-2559

Luo, S.C., Tong, X.H. & Khoo, B.C. (2007). Transition phenomena in the wake of a square cylinder. *J. Fluids Structs., 23*, 227-248

Mabey, D. (1972). Analysis and correlation of data on pressure fluctuations in separated flow. *J. Aircraft, 9*, 642-645

Macdonald, J.H.G., Irwin, P.A. & Fletcher, M.S. (2002). Vortex-induced vibrations of the Second Severn Crossing cable-stayed bridge -- full-scale and wind tunnel measurements. *Proc. ICE Structs. Bldgs., 152*(2), 123-134

Mas-Gallic, S. (1995). Particle approximation of a linear convection-diffusion problem with neumann boundary conditions. *SIAM J. Numer. Anal., 32*(4), 1098-1125

Matsumoto, M., Shiraishi, N., Shirato, H., Stoyanoff, S. & Yagi, T. (1993). Mechanism of, and turbulence effect on vortex-induced oscillations for bridge box girders. *J. Wind Eng. Ind. Aerod., 49*, 467-476

Miller, G.D. & Williamson, C.H.K. (1994). Control of three-dimensional phase dynamics in a cylinder wake. *Exp. Fluids, 18*, 26-35

Mills, R., Sheridan, J. & Hourigan, K. (2002). Response of base suction and vortex shedding from rectangular prisms to transverse forcing. *J. Fluid Mech., 461*, 25-49

Mills, R., Sheridan, J. & Hourigan, K. (2003). Particle image velocimetry and visualization of natural and forced flow around rectangular cylinders. *J. Fluid Mech., 478*, 299-323

Mills, R., Sheridan, J. & Hourigan, K. (2005). Wake of forced flow around elliptical leading edge plates. *J. Fluids Structs., 20*, 157-176

Mittal, R. & Balachandar, S. (1995). Effect of three-dimensionality on the lift and drag of nominally two-dimensional cylinders. *Phys. Fluids, 7*, 1841-1865

Monaghan, J.J. (1985). Extrapolating B-splines for interpolation. *J. Comput. Phys., 60*, 253-262

Monkewitz, P.A. (1988). The absolute and convective nature of instability in two-dimensional wakes at low Reynolds numbers. *Phys. Fluids, 31*(5), 999-1006

Monkewitz, P.A. & Nguyen, L.N. (1987). Absolute instability in the near-wake of two-dimensional bluff bodies. *J. Fluids Structs., 1*, 165-184

Morgenthal, G. (2002). *Aerodynamic analysis of structures using high-resolution vortex particle methods.* PhD Thesis, Department of Engineering, University of Cambridge.

Morkovin, M.V. (1964). *Flow around circular cylinder - a kaleidoscope of challenging fluid phenomena.* In: ASME Symposium on Fully Separated Flows, 1964, Philadelphia. pp.102-118

Najjar, F.M. & Vanka, S.P. (1993). Numerical study of separated-reattaching flow. *Theor. Comput. Fluid Dynam., 5*, 291-308

Nakaguchi, H., Hashimoto, K. & Muto, S. (1968). An experimental study on aerodynamic drag of rectangular cylinders. *J. Jpn. Soc. Aeronaut. Space Sci., 16*, 1-5

Nakamura, Y. (1996). Vortex shedding from bluff bodies with splitter plates. *J. Fluids Structs., 10*, 147-158

Nakamura, Y. & Nakashima, M. (1986). Vortex excitation of prisms with elongated rectangular, H and T cross-sections. *J. Fluid Mech., 163*, 149-169

Nakamura, Y., Ohya, Y., Ozono, S. & Nakayama, R. (1996). Experimental and numerical analysis of vortex shedding from elongated rectangular cylinders at low Reynolds numbers 200-10^3. *J. Wind Eng. Ind. Aerod., 65*, 301-308

Nakamura, Y., Ohya, Y. & Tsuruta, H. (1991). Experiments on vortex shedding from flat plates with square leading and trailing edges. *J. Fluid Mech., 222*, 437-447

Naudascher, E. & Rockwell, D. (1994). *Flow-induced vibration: an engineering guide.* Rotterdam: A.A. Balkema.

Naudascher, E. & Wang, Y. (1993). Flow-induced vibrations of prismatic bodies and grids of prisms. *J. Fluids Structs., 7*, 341-373

Norberg, C. (1993). Flow around rectangular cylinders: pressure forces and wake frequencies. *J. Wind Eng. Ind. Aerod., 49*, 187–196

Norberg, C. (1994). An experimental investigation of the flow around a circular cylinder: influence of aspect ratio. *J. Fluid Mech., 258*, 287-316

Norberg, C. (2003). Fluctuating lift on a circular cylinder: review and new measurements. *J. Fluids Structs., 17*, 57–96

Novak, M. & Tanaka, H. (1975). *Pressure correlations on a vibrating cylinder.* In: Proceedings of the 4th International Conference on Wind Effects on Buildings and Structures, September 1975, 1975, London. Cambridge: Cambridge University Press. pp.227-232

Oertel, H. (1990). Wakes behind blunt bodies. *Annu. Rev. Fluid Mech., 22*, 539-564

Ohya, Y., Nakamura, Y., Ozono, S., Tsuruta, H. & Nakayama, R. (1992). A numerical study of vortex shedding from flat plates with square leading and trailing edges. *J. Fluid Mech., 236*, 445-460

Okajima, A. (1982). Strouhal numbers of rectangular cylinders. *J. Fluid Mech., 123*, 379-398

Orlandi, P. (2007). Two-dimensional and three-dimensional direct numerical simulation of co-rotating vortices. *Phys. Fluids, 19*, 013101

Ould-Salihi, M.L., Cottet, G.-H. & El Hamraoui, M. (2000). Blending finite-difference and vortex methods for incompressible flow computations. *SIAM J. Sci. Comput., 22*, 1655-1674

Owen, J.S., Vann, A.M., Davies, J.P. & Blakeborough, A. (1996). The prototype testing of Kessock Bridge: response to vortex shedding. *J. Wind Eng. Ind. Aerod., 60*, 91-108

Pantazopoulos, M.S. (1994). *Vortex-Induced Vibration Parameters: Critical Review.* In: Proceedings of the 13th International Conference on Offshore Mechanics and Arctic Engineering (Vol. 1), 1994, Houston. pp.199–255

Parker, R. & Welsh, M.C. (1983). Effects of sound on flow separation from blunt flat plates. *Int. J. Heat Fluid Flow, 4*(2), 113-127

Parkinson, G.V. (1971). Wind-induced instability of structures. *Phil. Trans. Roy. Soc. Lond. Ser A, 269*, 395-409

Perlman, M. (1985). On the accuracy of vortex methods. *J. Comput. Phys., 59*, 200-223

Peskin, C.S. (1972). Flow patterns around heart valves: A numerical study. *J. Comput. Phys., 10*, 252-271

Ploumhans, P. & Winckelmans, G.S. (2000). Vortex methods for high-resolution simulations of viscous flow past bluff bodies of general geometry. *J. Comput. Phys., 165*, 354-406

Ploumhans, P., Winckelmans, G.S., Salmon, J.K., Leonard, A. & Warren, M.S. (2002). Vortex methods for direct numerical simulation of three-dimensional bluff body flows: application to the sphere at Re = 300, 500, 1000. *J. Comput. Phys., 178*, 427-463

Prasad, A. & Williamson, C.H.K. (1997). The instability of the shear layer separating from a bluff body. *J. Fluid Mech., 333*, 375-402

Provansal, M., Mathis, C. & Boyer, L. (1987). Bénard-von Kármán instability: transient and forced regimes. *J. Fluid Mech., 182*, 1-22

Robichaux, J., Balachandar, S. & Vanka, S.P. (1999). Three-dimensional Floquet instability of the wake of square cylinder. *Phys. Fluids, 11*(3), 560-578

Rockwell, D. & Naudascher, E. (1978). Self-sustaining oscillations of flow past cavities. *J. Fluids Eng. Trans. ASME, 100*, 152-165

Rockwell, D. & Naudascher, E. (1979). Self-sustained oscillations of impinging free shear layers. *Annu. Rev. Fluid Mech., 11*, 67-94

Roshko, A. (1954a). *On the development of turbulent wakes from vortex streets*. NACA Tech. Report 1191.

Roshko, A. (1954b). *On the drag and shedding frequency of two-dimensional bluff bodies.* NACA Tech. Note 3169.

Roshko, A. (1955). On the wake and drag of bluff bodies. *J. Aeronaut. Sci., 22*(1), 124-132

Roshko, A. (1993). Perspectives on bluff body aerodynamics. *J. Wind Eng. Ind. Aerod., 49*, 79-100

Roshko, A. & Lau, J.C. (1965). *Some observations on transition and reattachment of a free shear layer in incompressible flow.* In: Proceedings of the Heat Transfer and Fluid Mechanics Institute, 1965. Stanford: Stanford University Press. pp.157-167

Rossi, L.F. (1996). Resurrecting core spreading vortex methods: a new scheme that is both deterministic and convergent. *SIAM J. Sci. Comput., 17*, 370-397

Roushan, P. & Wu, X.L. (2005). Universal wake structures of Kármán vortex streets in two-dimensional flows. *Phys. Fluids, 17*(7), 073601

Saha, A.K., Biswas, G. & Muralidhar, K. (2003). Three-dimensional study of flow past a square cylinder at low Reynolds numbers. *Int. J. Heat Fluid Flow, 24*, 54–66

Saha, A.K., Muralidhar, K. & Biswas, G. (2000). Experimental study of flow past a square cylinder at high Reynolds numbers. *Exp. Fluids, 29*, 553-563

Sarpkaya, T. (1979). Vortex-induced oscillations–a selective review. *J. Appl. Mech., 46*, 241-258

Sarpkaya, T. (1989). Computational methods with vortices – the 1988 Freeman Scholar Lecture. *J. Fluids Eng. Trans. ASME, 111*, 5-52

Sarpkaya, T. (2004). A critical review of the intrinsic nature of vortex-induced vibrations. *J. Fluids Structs., 19*, 389-447

Sasaki, K. & Kiya, M. (1991). Three-dimensional vortex structure in a leading-edge separation bubble at moderate Reynolds numbers. *J. Fluids Eng. Trans. ASME, 113*, 405-410

Scanlan, R.H. (1978). The action of flexible bridges under wind. I: Flutter Theory. *J. Sound Vib., 60*(2), 187-199

Shang, J.S. (2004). Three decades of accomplishments in computational fluid dynamics. *Progr. Aero. Sci., 40*(3), 173-197

Shankar, S. (1996). *A new mesh-free vortex method.* PhD Thesis, Department of Mechanical Engineering, Florida State University.

Shankar, S. & Van Dommelen, L. (1996). A new diffusion procedure for vortex methods. *J. Comput. Phys., 127*, 88-109

Shiels, D. (1998). *Simulation of controlled bluff body flow with a viscous vortex method.* PhD Thesis, Graduate Aeronautical Laboratories, California Institute of Technology.

Shimizu, M. & Tanida, Y. (1978). On the fluid forces acting on rectangular sectional cylinders. *Trans. JSME B, 44*(384), 2699-2706. (in Japanese)

Shiraishi, N. & Matsumoto, M. (1983). On classification of vortex-induced oscillation and its application for bridge structures. *J. Wind Eng. Ind. Aerod., 14*, 419-430

Sigurdson, L.W. (1995). The structure and control of a turbulent reattaching flow. *J. Fluid Mech., 298*, 139-165

Sigurdson, L.W. & Roshko, A. (1988). The structure and control of a turbulent reattaching flow. In H.W. Liepmann & R. Narasimha (Eds.), Turbulence Management and Relaminarisation. New York: Springer-Verlag. pp.497-514

Simiu, E. & Scanlan, R.H. (1996). *Wind effects on structures: Fundamentals and applications to design* (3rd ed.). New York: John Wiley & Sons Inc.

Simmons, J.E.L. (1977). Similarities between two-dimensional and axisymmetric vortex wakes. *Aeronaut. Q., 26*, 15-20

Simpson, R.L. (1985). Two-dimensional turbulent separated flow. *AGARDograph, 287.*

Simpson, R.L. (1989). Turbulent boundary-layer separation. *Annu. Rev. Fluid Mech., 21*, 205-234

Sohankar, A., Davidson, L. & Norberg, C. (1995). *Numerical simulation of unsteady flow around a square two-dimensional cylinder.* In: Proceedings of the 12th Australian Fluid Mechanics Conference, December 10-15, 1995, Sydney, Australia. pp.517–520

Sohankar, A., Norberg, C. & Davidson, L. (1999). Simulation of three-dimensional flow around a square cylinder at morderate Reynolds numbers. *Phys. Fluids, 11*(2), 288-306

Song, S., Degraaff, D.B. & Eaton, J.K. (2000). Experimental study of a separating, reattaching, and redeveloping flow over a smoothly contoured ramp. *Int. J. Heat Fluid Flow, 21*, 512-519

Song, S. & Eaton, J.K. (2004). Reynolds number effects on a turbulent boundary layer with separation, reattachment, and recovery. *Exp. Fluids, 36*, 246-258

Soria, J., Sheridan, M. & Wu, J. (1993). Spatial evolution of the separated shear layer from a square leading edge flat plate. *J. Wind Eng. Ind. Aerod., 49*, 237-246

Stansby, P.K. (1976). Base pressure of oscillating circular cylinder. *J. Eng. Mech. Div. Proc. ASCE, 102*, 591-600

Staubli, T. & Rockwell, D. (1989). Pressure fluctuations on an oscillating trailing edge. *J. Fluid Mech., 203*, 307-346

Stokes, A.N. & Welsh, M.C. (1986). Flow-resonant sound interaction in a duct containing a plate, II: square leading edge. *J. Sound Vib., 104*, 55-73

Ta Phuoc Loc & Bouard, R. (1985). Numerical solution of the early stage of the unsteady viscous flow around a circular cylinder: a comparison with experimental visualization and measurements. *J. Fluid Mech., 160*, 93-117

Tafti, D.K. & Vanka, S.P. (1991). A three-dimensional numerical study of flow separation and reattachment on a blunt plate. *Phys. Fluids A, 3*(12), 2887-2909

Tan, B.T., Thompson, M.C. & Hourigan, K. (1998). Flow around long rectangular plates under cross-flow perturbations. *Int. J. Fluid Dynam., 2*, Article 1. Retrieved from http://elecpress.monash.edu.au/ijfd/1998_vol2/paper1/paper1.html

Tan, B.T., Thompson, M.C. & Hourigan, K. (2004). Flow past rectangular cylinders: receptivity to transverse forcing. *J. Fluid Mech., 515*, 33-62

Taylor, Z.J., Gurka, R. & Kopp, G.A. (2009). The role of geometry on vortex shedding from elongated bluff bodies. *submitted to Journal of Fluid Mechanics*

Thompson, M.C. & Hourigan, K. (2005). The shear-layer instability of a circular cylinder wake. *Phys. Fluids, 17*(2), 021702

Triantafyllou, G.S., Kupfer, K. & Bers, A. (1987). Absolute instabilities and self-sustained oscillation in the wakes of circular cylinders. *Phys. Rev. Lett., 59*(17), 1914-1917

Tutar, M. & Holdø, A.E. (2000). Large Eddy Simulation of a smooth circular cylinder oscillating normal to a uniform flow. *J. Fluids Eng. Trans. ASME, 122*, 694-702

Unal, M.F. & Rockwell, D. (1988a). On vortex formation from a cylinder. Part 1. The initial instability. *J. Fluid Mech., 190*, 491-512

Unal, M.F. & Rockwell, D. (1988b). On vortex formation from a cylinder. Part 2.Control by splitter-plate interference. *J. Fluid Mech., 190*, 513-529

Van Dommelen, L.L. & Shen, S.F. (1980). The spontaneous generation of the singularity in a separating laminar boundary layer. *J. Comput. Phys., 38*, 125-140

Walther, J.H. (2003). An influence matrix particle-particle particle-mesh algorithm with exact particle-particle correction. *J. Comput. Phys., 184*, 670-678

Wee, D. & Ghoniem, A.F. (2008). A fast 3D particle method for the simulation of buoyant flow. *J. Comput. Phys., 227*, 9063-9090

Welsh, M.C., Stokes, A.N. & Parker, R. (1984). Flow-resonant sound interaction in a duct containing a plate, I: semi-circular leading edge. *J. Sound Vib., 95*, 305-323

Westphal, R.V. & Johnston, J.P. (1984). Effect of initial conditions on turbulent reattachment downstream of a backward-facing step. *AIAA J., 22*, 1727-1732

Williamson, C.H.K. (1988). Defining a universal and continuous Strouhal-Reynolds number relationship for the larminar vortex shedding of a circular cylinder. *Phys. Fluids, 31*(10), 2742-2744

Williamson, C.H.K. (1989). Oblique and parallel modes of vortex shedding in the wake of a circular cylinder at low Reynolds numbers. *J. Fluid Mech., 206*, 579-627

Williamson, C.H.K. (1992). The natural and forced formation of spot-like 'vortex dislocations' in the transition of a wake. *J. Fluid Mech., 243*, 393-441

Williamson, C.H.K. (1996). Vortex dynamics in the cylinder wake. *Annu. Rev. Fluid Mech., 28*, 477-539

Williamson, C.H.K. & Brown, G.L. (1998). A series in $1/\sqrt{Re}$ to represent the Strouhal-Reynolds number relationship of the cylinder wake. *J. Fluids Structs., 12*, 1073-1085

Wood, C.J. (1971). The effect of lateral vibrations on vortex shedding from blunt-based aerofoils. *J. Sound Vib., 14*, 91-102

Wu, J.C. (1981). Theory for aerodynamic force and moment in viscous flows. *AIAA J., 19*, 432-441

Yaghoubi, M. & Mahmoodi, S. (2004). Experimental study of turbulent separated and reattached flow over a finite blunt plate. *Exp. Therm. Fluid Sci., 29*, 105-112

Yarusevych, S., Sullivan, P.E. & Kawall, J.G. (2009). On vortex shedding from an airfoil in low-Reynolds-number flows. *J. Fluid Mech., 632*, 245–271

Yeung, W.W.H. & Parkinson, G.V. (2004). Analysis and modeling of pressure recovery for separated reattaching flows. *J. Fluids Eng. Trans. ASME, 126*, 335-361

Ying, L.-A. (1987). Convergence study of viscous splitting in bounded domains. *Lect. Notes Math., 1297*, 184-202

Ying, L.-A. (1990). Viscous splitting for the unbounded problem of the navier-stokes equations. *Math. Comput., 55*, 89-113

APPENDIX A

THE FORMATION OF VORTEX SHEDDING FROM CIRCULAR CYLINDERS

Although the motion of the separation points makes it more difficult to understand various aspects of the problem, circular cylinders have been the most popular bluff body in the literature. Among the vast number of research papers related to this subject published during the long course of studies, the number of papers devoted to circular cylinders far exceeds the total number of papers dealing with all other bluff bodies (Roshko 1993). That is, most of the knowledge accumulated so far in the area of bluff-body flows has been contributed by the studies related to circular cylinders. This appendix provides a brief overview of the current understanding of the formation of vortex shedding from circular cylinders.

A.1. FLOW REGIMES

The flow pattern around a circular cylinder is often described in terms of various Reynolds number regimes (Morkovin 1964, Lienhard 1966, Pantazopoulos 1994, Williamson 1996), which in fact correspond to different states (turbulent or laminar) of the boundary layers before separation (the location of the separation points in turn depends on the state of the boundary layer) and the wake. For a smooth circular cylinder in uniform flow, the major Reynolds number regimes of vortex shedding are shown in Figure A.1.

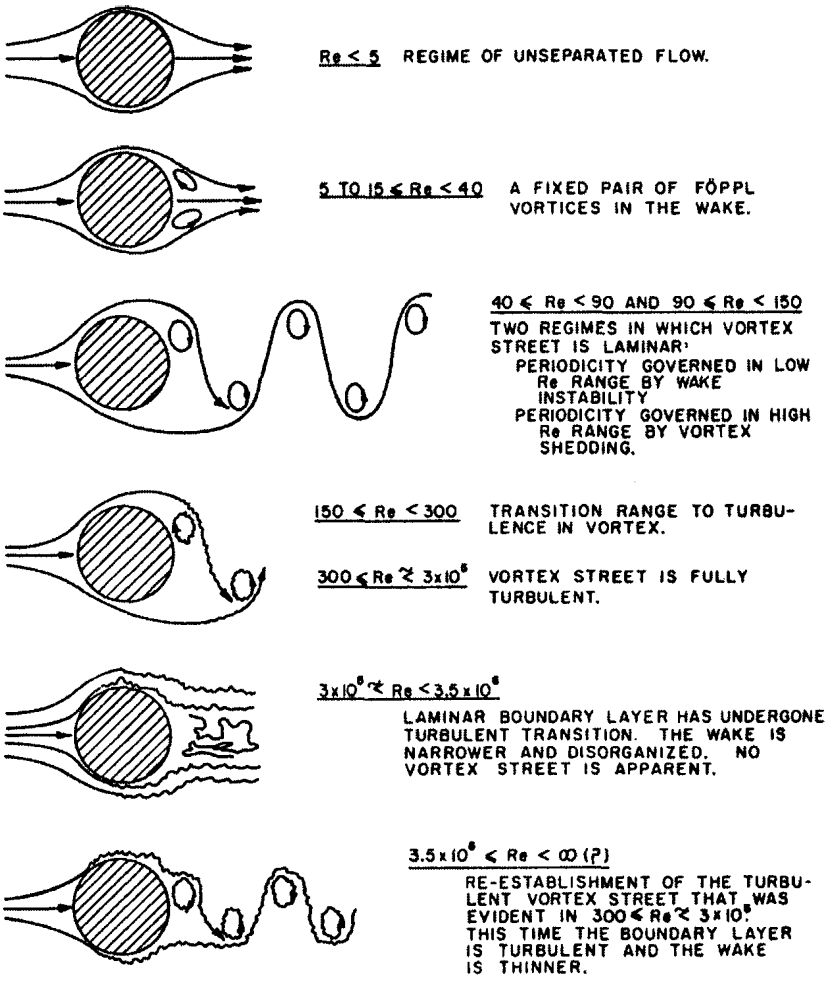

Figure A.1. Regimes of fluid flow past circular cylinders (Lienhard 1966)

According to Pantazopoulos (1994), the Reynolds number range, $300 < Re < 1.5\times10^5$, is called the subcritical regime, in which the laminar boundary layers separate at about 80° after the stagnation point and the vortex shedding is strong and periodic; the range, $1.5\times10^5 < Re < 3.5\times10^6$, is referred to as the transitional (or supercritical) regime (which is often further divided into two sub-regimes: the critical regime, $1.5\times10^5 < Re < 3.5\times10^5$, and the super critical regime, $3.5\times10^5 < Re < 3.5\times10^6$), where the separation points move to 140° after the stagnation point and the wake narrows substantially, with a consequent sharp drop in the drag coefficient of the cylinder. Vortex shedding in this

range is characterized by a broad spectrum without a dominant frequency. In the postcritical (transcritical) regime, where $Re > 3.5\times10^6$, regular vortex shedding is re-established, and the vortex shedding persists at Reynolds numbers as high as 10^{11}. The suppression and re-establishment of the periodic vortex shedding in the transitional and postcritical regimes may be explained by the observation that, regular vortex shedding can be severely disrupted when the separation line is not straight (Bearman 1984, Bearman & Owen 1998). In the transitional regime, the boundary layer is laminar, transition to turbulence occurs within a separation bubble on the surface. The separation bubble breaks down at random points across the span of the cylinder, which results in a separation line that is not straight and thus the regular vortex shedding disappears. In the postcritical regime, the transition occurs within the boundary layer and thus a straight separation line, and hence, a regular vortex shedding is re-established.

A.2. THE FORMATION OF VORTEX SHEDDING

Due to the viscous effects in the boundary layers before separation, the inner part of the free shear layer moves slower than the outer part, and, hence, the shear layer tends to roll up into discrete vortices (Blevins 1986). There is no complete solution to the problem of vortex shedding, and it is difficult to describe exactly how shedding occurs (Pantazopoulos 1994), but previous studies have led to reasonable insight into the mechanism. The numerical simulation reported by Abernathy & Kronauer (1962) demonstrates that, the interaction between two parallel free shear layers, represented by oppositely signed vortex sheets, results in clouds of vortices that resemble the regular Kármán vortex street. The simulation also predicts a reduction in the net strength of the

concentrated clouds to about 60% of the original circulation generated during one vortex formation cycle, due to the cancellation of some oppositely signed point vortices mixing within the clouds. This is in good agreement with observations in experiments (see e.g., Sarpkaya 2004, and Roushan & Wu 2005). In addition, it is estimated by Roushan & Wu (2005) that, only about 5% of the work done by the mean flow on the cylinder is extracted by the vortices in the wake. Abernathy & Kronauer (1962) emphasize that, it is the presence of two vortex sheets that is primarily responsible for the formation of the vortex street, while the role of the bluff body is merely to generate the vortex layers. Bearman (1984) adds that the presence of the bluff body may also modify the process by allowing feedback between the wake and the shedding of circulation at the separation points.

The phenomenological description of the mechanics of the vortex formation region proposed by Gerrard (1966) is widely accepted as a descriptive model to explain many phenomena related to vortex shedding (Berger & Wille 1972, Griffin & Ramberg 1974, Bearman 1984, Williamson 1996). It is hypothesized in Gerrard (1966) that, a vortex will keep growing as long as it is fed by circulation from the shear layer until it is strong enough to draw the shear layer on the opposite side across the wake. The approaching oppositely signed vorticity from the other shear layer, with sufficient concentration, will cut off further supply of circulation to the vortex, which is then shed and convected downstream. Gerrard's formation region model is shown in Figure A.2, by filament lines in the rolling-up shear layer at the instant when the entrained irrotational flow begins to cross the wake axis. Some portion of the entrained fluid is drawn into the growing vortex *a*, the portion *b* is captured by the shear layer upstream of the vortex, and

portion *c* is trapped into the interior of the formation region, which will be cancelled half a shedding period later. Since vortex formation involves mixing of oppositely signed vortices, the strength of a shed vortex will be less than the total circulation generated from one side of a fluff body during a shedding cycle.

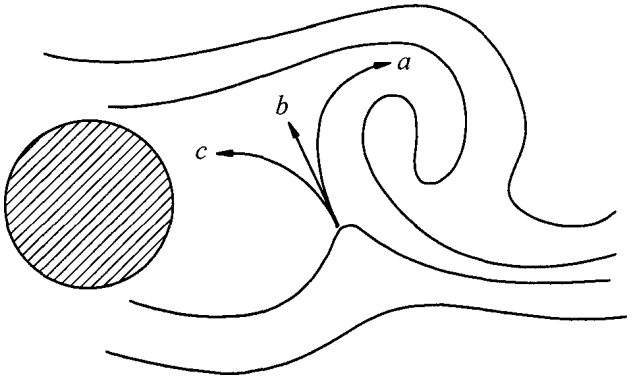

Figure A.2. Filament-line sketch of the vortex formation region (after Gerrard 1966)

Gerrard (1966) suggests that there are two characteristic length scales, the length of the formation region and the diffusion length (the thickness of the free shear layer at the end of the formation region), that govern the vortex-shedding frequency. Gerrard defines the end of the formation region as the point where fluid from outside the wake first crosses the axis of the wake. He argues that, if the diffusion length is larger (hence the vortices in the shear layer are more diffused), it will take longer for a sufficient concentration of vorticity to be entrained across the wake and to initiate shedding, hence, the shedding frequency will be lower and the formation length will be longer. On the other hand, the greater diffusion of the vorticity in the shear layer on the other side also leads to less entrainment of oppositely signed vortices into the growing vortex, and thus, stronger vortices are observed. He suggests that the relatively constant Strouhal number over the whole subcritical Reynolds number range is a consequence of the fact that the

two major controlling length scales tend to change the frequency in an opposite manner. The same reasoning is also applied to explain the effects of turbulence. When the free-stream turbulence level is higher, the formation region shrinks, but the diffusion length is assumed to increase in such a way that the opposite effects on the frequency are cancelled by each other.

A.3. INSTABILITY THEORIES

In the 1980s and 1990s, the theories of absolute and convective instabilities received much attention (see, e.g., Koch 1985, Provansal *et al.* 1987, Monkewitz & Nguyen 1987, Triantafyllou *et al.* 1987, Chomaz *et al.* 1988, Monkewitz 1988, Huerre & Monkewitz 1990, and Oertel 1990). These theories have led to a promising analytical approach to understanding the physics of vortex formation. If a small disturbance in a flow grows exponentially at the location of its generation and the instability wave travels both upstream and downstream, the flow is termed absolutely unstable. Oertel (1990) has proved the existence of absolutely unstable regions in bluff-body wakes based on experimental evidence and numerical simulations. An absolutely unstable flow is not sensitive to external disturbances, and, hence, the flow is likely to develop an "intrinsic response". Any transition point in the flow with a real branch-point frequency may serve as a "selective reflector" for instability waves of the same frequency, while the solid boundary may act as a "broadband reflector" for all instability waves. Hence, a self-sustained feedback loop may exist in the flow and lead to resonance phenomena (Monkewitz & Nguyen 1987). On the other hand, the flow is considered to be convectively unstable if the growing disturbance is convected away from the source and

both ends of the instability wave propagate downstream. A convectively unstable flow is sensitive to external forcing, which is faithfully reflected by the instability wave. The term "global instability" was introduced by Chomaz *et al.* (1988) to emphasize that the region of absolute instability must be large enough for a global mode oscillation (e.g., a Kármán vortex street) to be self-excited. Although the physical mechanism of the vortex formation in bluff body wakes is still not fully understood, stability theories have demonstrated the ability of explaining many relevant phenomena, such as the self-sustained fluid oscillation, frequency and mode selection in the wake, and receptivity to external forcing. It is now well established that Kármán vortex street behind a circular cylinder is a result of a Hopf bifurcation to a global instability mode in the flow at a Reynolds number above 49 (see Provansal *et al.* 1987, Griffin & Hall 1991, Williamson 1996, Prasad & Williamson 1997, and Gal & Croquette 2000), which has been demonstrated in Provansal *et al.* (1987) that it is well described by the Stuart-Landau equation. The near wake region (the formation region) is speculated to be globally unstable, and is assumed to be responsible for sustaining the continuous formation of the vortex street. The shear layers and the flow further downstream in the wake are considered to be convectively unstable (Monkewitz & Nguyen 1987, Huerre & Monkewitz 1990, Griffin & Hall 1991).

In addition to the primary wake instability that results in the Kármán vortex street, the shear layers separating from a cylinder become unstable $Re > 1{,}200$, usually known as the "Bloor-Gerrard instability", or the "Kelvin-Helmholtz instability" (Bloor 1964, Gerrard 1978, Roshko 1993, Williamson 1996, Prasad & Williamson 1997, Thompson & Hourigan 2005). The shear-layer instability is commonly considered to be driven by a

Kelvin-Helmholtz mechanism, and it scales with the thickness of the shear layer. Compared to the primary global instability, which scales with the dimension of the bluff body, the time and length scales of the shear-layer instability are much smaller. It is speculated that this small-scale instability does not have a significant influence on the large-scale vortex formation in the wake, and no evidence of successive coalescence of the small vortices into large-scale structures has been observed, but it may contribute to the thickening of the mean shear layer (Unal & Rockwell 1988a,b). In her pioneering work, Bloor (1964) suggests that this instability is governed by the boundary-layer state at separation, and that its frequency normalized by that of large scale vortex shedding in the wake scales with $Re^{1/2}$. This frequency scaling law has led to an ongoing debate in the literature (see Roshko 1993, Prasad & Williamson 1997, Thompson & Hourigan 2005, and references cited therein). By fitting the available data in the literature over a wide range of Reynolds number, and through theoretical reasoning, Prasad & Williamson suggest that the exponent is 0.67 instead of 1/2. Thompson & Hourigan find that the data may be grouped into two distinct regions of Reynolds numbers, $1{,}500 < Re < 5{,}000$ and $Re > 10{,}000$ (which may be associated with the drastic changes in the near wake between these two Re ranges). Over these two Re ranges the exponent has two different values, 0.57 and 0.52 respectively, considerably lower than 0.67 suggested by Prasad & Williamson. Thompson & Hourigan further suggest that the slightly higher values than 1/2 is due to the effect of the mobility of separation point on a circular cylinder, and Bloor's relationship may be approximately applied to the two Re regions, but not in-between. They also suggest that, for fixed-point separation there should be no such deviations.